THE EFFECT OF THE DIRECTION OF THE ROLLING WAY ON BIO-CORROSION PROPERTIES OF AZ31 ALLOY

**2024
MASTER THESIS
METALLURGICAL AND MATERIALS ENGINEERING**

Ali Abdulhaleem Raoof AL SHAIBANI

**Thesis Advisor
Assist. Prof. Dr. İsmail Hakkı KARA**

THE EFFECT OF THE DIRECTION OF THE ROLLING WAY ON BIO-CORROSION PROPERTIES OF AZ31 ALLOY

Ali Abdulhaleem Raoof AL SHAIBANI

T.C.
Karabuk University
Institute of Graduate Programs
Department of Metallurgical and Materials Engineering
Prepared as
Master Thesis

Thesis Advisor
Assist. Prof. Dr. İsmail Hakkı KARA

KARABÜK
January 2024

I certify that in my opinion the thesis submitted by Ali Abdulhaleem Raoof AL SHAIBANI titled "THE EFFECT OF THE DIRECTION OF THE ROLLING WAY ON BIO-CORROSION PROPERTIES OF AZ31 ALLOY" is fully adequate in scope and in quality as a thesis for the degree of Master of Science

Assist. Prof. Dr. İsmail Hakkı KARA   ....
Thesis Advisor, Department of Metallurgical and Materials Engineering

This thesis is accepted by the examining committee with a unanimous vote in the Department of Metallurgical and Materials Engineering as a Master of Science thesis. January 19, 2024

<u>Examining Committee Members</u> (Institutions)   Signature

Chairman:Prof. Dr. Mustafa ACARER (SU)   ....

Member : Prof. Dr. Hayrettin AHLATCI (KBU)   ....

Member : Assist. Prof. Dr. İsmail Hakkı KARA (KBU)   ....

The degree of Master of Science by the thesis submitted is approved by the Administrative Board of the Institute of Graduate Programs, Karabuk University.

Doç. Dr. Zeynep ÖZCAN.   ....
Lisansüstü Eğitim Enstitüsü Müdürü

"I declare that all the information within this thesis has been gathered and presented in accordance with academic regulations and ethical principles and I have according to the requirements of these regulations and principles cited all those which do not originate in this work as well."

Ali Abdulhaleem Raoof AL SHAIBANI

ABSTRACT

Master Thesis

THE EFFECT OF THE DIRECTION OF THE ROLLING WAY ON BIO-CORROSION PROPERTIES OF AZ31 ALLOY

Ali Abdulhaleem Raoof AL SHAIBANI

Karabük University
Institute of Graduate Programs
Metallurgical and Materials Engineering

Thesis Advisor:
Assist. Prof. Dr. İsmail Hakkı KARA
January 2024, 102 pages

Producing lightweight and efficient materials is a challenge for manufacturers nowadays. containing alloys in certain applications, due to of their poor resistance to corrosion, magnesium alloys are not as widely used in industrial and medical application. Consequently, it is imperative that we deepen our comprehension of the factors and processes influencing magnesium corrosion and devise more potent plans to strengthen magnesium corrosion resistance. Investigation the effect of rolling direction and addition of alloying elements (calcium and cerium) on the microstructural and corrosion behavior of AZ31-Mg alloys. In this study, gravity casting is used to fabricate AZ31 and a modified AZ31 containing Ca-Ce alloys. After casting, homogenization took place for 24 hours at 350 °C. The prepared samples were rolled at 400 °C in three different directions. The corrosion investigation included potentiodynamic corrosion tests, electrochemical impedance spectroscopy, and immersion experiments in red (HBSS) and white (HBSS+)

solutions. X-ray diffraction was used to analyze the phases and intermediate components. Optical (OM)and scan electron microscope (SEM) were used to examine the microstructures and energy -dispersive x-ray spectroscopy (EDX) was used to determine the elements composition. To evaluate the performance of the alloys in different media, wet wear tests were also carried out. The XRD analysis showed that α-Mg and β-$Mg_{17}Al_{12}$ phases were frequently detected in the studied AZ31 alloys. Addition of Ce resulted in the formation of $Al_{11}Ce_3$, while the weight ratio of Mn/Al was closely to the ratio of Al_8Mn_5 detected on the AZ31. The microstructure images also showed that the average grain size varied depending on the rolling speed and direction, with the grains becoming thinner along the rolling direction after rolling with the addition of Ce. SEM analysis revealed a high pitting corrosion rate in samples A1 to A3, whereas the addition of Ca and Ce in samples B1 to B3 resulted in a significant decrease in the corrosion rate. The wet wear test revealed an increase in weight loss at higher loads due to increased friction, while the addition of Ca and Ce increased wear resistance, which was particularly evident in the 45° angle samples. The results of the immersion corrosion test demonstrated that the corrosion resistance of the Mg-based AZ31 materials was greatly enhanced by the addition of Ca and Ce. The potentiodynamic polarization tests revealed that the addition of Ca and Ce to AZ31 alloy generally improved its corrosion resistance in HBSS solution, as evidenced by higher open circuit potential (Ecorr), lower corrosion current density (Icorr), and reduced cathodic and anodic Tafel slopes (Beta C and Beta A). The electrochemical impedance (EIS) measurements showed that the addition of Ca and Ce to the AZ31-Mg alloys improved the corrosion resistance, as evidenced by reduced impedance values. The microstructure and orientation of the samples significantly influenced the EIS results, with samples rolled perpendicular direction having the highest impedance values, followed by samples rolled at a 45° angle and then parallel to the rolling direction.

ÖZET

Yüksek Lisans Tezi

AZ31 ALAŞIMININ BİYO-KOROZYON ÖZELLİKLERİNE HADDELENME YOLU YÖNÜNÜN ETKİSİ

Ali Abdulhaleem Raoof AL SHAIBANI

Karabük Üniversitesi
Lisansüstü Eğitim Enstitüsü
Metalurji ve Malzeme Mühendisliği

Tez Danışmanı:
Dr. Öğr. Üyesi İsmail Hakkı KARA
Ocak 2024, 102 sayfa

Hafif ve verimli malzemeler üretmek günümüzde üreticiler için zorlu bir iştir. Belirli uygulamalarda alaşımlar içerir. Korozyona karşı zayıf dirençleri nedeniyle magnezyum alaşımları endüstriyel ve tıbbi ortamlarda yaygın olarak kullanılmamaktadır. Sonuç olarak, magnezyum korozyonunu etkileyen faktörler ve süreçler hakkındaki anlayışımızı derinleştirmemiz ve magnezyum korozyon direncini güçlendirmek için daha güçlü planlar tasarlamamız zorunludur. AZ31-Mg alaşımlarının mikroyapı ve korozyon davranışına haddeleme yönü ve alaşım elementleri (kalsiyum ve seryum) ilavesinin etkisinin araştırılması. Bu çalışmada, AZ31 ve modifiye edilmiş AZ31 içeren Ca-Ce alaşımlarının imalatı için yerçekimi dökümü kullanılmıştır. Dökümden sonra homojenizasyon 350°C'de 24 saat süreyle gerçekleştirildi. Hazırlanan numuneler 400 °C sıcaklıkta üç farklı yönde haddelenmiştir. Korozyon araştırması potansiyodinamik korozyon testlerini, elektrokimyasal empedans spektroskopisini ve kırmızı (HBSS) ve beyaz (HBSS+)

çözeltilere daldırma deneylerini içeriyordu. Fazlar ve ara bileşenleri analiz etmek için X-ışını kırınımı kullanıldı. Mikroyapıları incelemek için optik mikroskop (OM) ve taramalı elektron mikroskobu (SEM), element kompozisyonunu belirlemek için ise enerji dağılımlı x-ışını spektroskopisi (EDX) kullanıldı. Alaşımların farklı ortamlardaki performansını değerlendirmek için ıslak aşınma testleri de yapıldı. XRD analizi, çalışılan AZ31 alaşımlarında α-Mg ve β-$Mg_{17}Al_{12}$ fazlarının sıklıkla tespit edildiğini gösterdi. Ce'nin eklenmesi $Al_{11}Ce_3$'ün oluşmasıyla sonuçlandı; Mn/Al ağırlık oranı ise AZ31'de tespit edilen Al_8Mn_5 oranına yakındı. Mikroyapı görüntüleri ayrıca ortalama tane boyutunun haddeleme hızına ve yönüne bağlı olarak değiştiğini, Ce ilavesi ile haddeleme sonrasında tanelerin haddeleme yönü boyunca inceldiğini gösterdi. SEM analizi, A1'den A3'e kadar olan numunelerde yüksek oyuklanma korozyonu oranını ortaya çıkarırken, B1'den B3'e kadar olan numunelere Ca ve Ce'nin eklenmesi, korozyon oranında önemli bir düşüşe yol açmıştır. Koroziv aşınma testi, artan sürtünme nedeniyle daha yüksek yüklerde ağırlık kaybında bir artış olduğunu ortaya koyarken, Ca ve Ce ilavesinin, özellikle 45° açılı numunelerde belirgin olan aşınma direncini arttırdığını ortaya çıkardı. Daldırma korozyon testinin sonuçları, Mg bazlı AZ31 malzemelerinin korozyon direncinin Ca ve Ce ilavesiyle büyük ölçüde arttığını gösterdi. Potansiyodinamik polarizasyon testleri, AZ31 alaşımına Ca ve Ce ilavesinin, daha yüksek açık devre potansiyeli (Ecorr), daha düşük korozyon akım yoğunluğu (Icorr) ve azaltılmış katodik ve anodik Tafel eğimleriyle kanıtlandığı gibi, HBSS çözeltisindeki korozyon direncini genel olarak iyileştirdiğini ortaya çıkardı. (Beta C ve Beta A). Elektrokimyasal empedans (EIS) ölçümleri, AZ31-Mg alaşımlarına Ca ve Ce ilavesinin, azaltılmış empedans değerlerinden de anlaşılacağı üzere korozyon direncini arttırdığını gösterdi. Numunelerin mikro yapısı ve yönelimi, EIS sonuçlarını önemli ölçüde etkilemiştir; dik yönde haddelenen numuneler en yüksek empedans değerlerine sahip olmuş, bunu 45° açıyla haddelenen ve ardından haddeleme yönüne paralel olan numuneler takip etmiştir.

Anahtar Sözcükler : AZ31 alaşımı, Döküm, Yuvarlanma yönü, Elektrokimyasal korozyon, koroziv aşınma.

Bilim Kodu   :   91501

ACKNOWLEDGMENT

CONTENTS

LIST OF FIGURES

LIST OF TABLES

SYMBOLS AND ABBREVIATIONS INDEX

SYMBOLS

Icorr :Corrosion current density

Ecorr :Corrosion potential

G   :Gram

Ca   :Calcium

Ce   :Cerium

℃   :Degrees Celsius

ABBREVIATIONS

SEM   :Scanning Electron Microscope

ASTM   :American Society for Testing and Materials

XRF   :X Ray Fluorescence

ISO   :International Organization For Standardization

SCE   :Saturated Calomel Electrode

PART 1

INTRODUCTION

1.1. INTRODUCTION

Magnesium and its alloys stand out in aerospace, automotive, and weapons industries for its excellent strength-to-weight ratio. Due to its ease of machining and casting quality, new studies and applications of these alloys are being carried out. Another common application was using of magnesium alloys as implants in human body [1-3]. Due to its rapid corrosion process, magnesium has not been used in humid or salty environments, which is one of the primary barriers to its use in structural applications. [4]. Fine-grained magnesium alloys pose a problem because the sophisticated processing and operating environment can improve or degrade the corrosion resistance of these materials depending on the alloy type [5, 6]. Comparing magnesium alloys with conventional metallic materials, polymers and ceramics shows a number of advantages. Their elastic modulus is between 41 and 45 GPA, making them ideal for load-bearing applications due to their low density. The biodegradability of magnesium has been demonstrated in living organisms and it is an essential mineral for human metabolism and biological processes. Magnesium alloys have been used in biodegradable implants like stents, screws, and intramedullary nails. However, due to their high reactivity, they corrode quickly. The main disadvantage of using magnesium alloys in biomedical applications is their rapid decomposition in chlorine-containing solutions such as blood plasma or human body fluids. Magnesium alloys are also susceptible to galvanic corrosion, which can quickly damage the material. Despite these drawbacks, magnesium alloys have numerous advantages, making them a preferred choice for load-bearing applications [7].

Magnesium alloys' low formability is their primary drawback, but their light weight gives them great potential as a substitute for other technological materials. The AZ31 alloy discussed in this article contains zinc and aluminum as the main alloying element, which improve mechanical strength and corrosion resistance [3]. For alloys with hexagonal structure, plastic deformation is highly dependent on temperature, degree of deformation, speed, and initial crystallographic texture because they have few slip systems, which means that the predominant deformation system at low temperatures is twins. [4,5,6].

According to studies, as the grain size increases, the rate at which AZ31 alloy corrodes in a sodium chloride solution also increases. One explanation for this could be grain boundaries that serve as a barrier against corrosion. However, results showing that grain boundaries cannot stop the propagation of corrosion and are more chemically active than the grain center contradict this statement. Greater stability of the oxide film on the surface of finer-grained magnesium alloys explains the observed improvement in corrosion resistance. However, further research is needed to confirm this claim [8, 9]. Applying these magnesium alloys in biodegradable implants is being extensively studied, with characterizations involving immersion in a solution similar to the physiological environment or body fluids, favoring the formation of protective oxide films [10, 11] . Mg breaks down spontaneously in the body with water, reducing the need for a second surgery to remove the implant. Mg degradation products can activate or catalyze more than 300 types of enzymes and are necessary for various metabolic processes in the human body [12]. Magnesium as a biomaterial has a disadvantage due to hydrogen emission during its corrosion process. This emission, which results from an electrochemical reaction with water or bodily fluids, decreases magnesium's resistance to corrosion and can cause stress corrosion cracking, which jeopardizes the mechanical strength and longevity of magnesium implants. Additionally, hydrogen emission can trigger inflammation, damage tissues, form gas bubbles, and alter pH levels, hindering healing and causing complications in the host body. Various methods such as alloying, coating, surface modification, and biocompatible design. are needed to control these issues [13, 14]. Finally, based on the above, this work is justified by the fact that the influence of alloying elements and rolling in different directions on the corrosion resistance of

magnesium alloys is a topic that is not yet fully understood in the literature and needs to be taken into account the need to understand the mechanism and kinetics of the to understand corrosion of these alloys with the aim of using them in various applications, from aircraft to surgical implants. Studies on the corrosion resistance of the AZ31 alloy underwent by different heat treatments revealed that the corrosion resistance in a 3 percent NaCl solution was significantly improved due to the dissolution of the $Mg_{17}Al_{12}$ beta phase, the disappearance of twinning, and the increase in grain size. [15]. As heat treatment increases corrosion resistance, this thesis examined the corrosion resistance of a heat-treated AZ31 alloy in a solution hanks solution and after rolling in various directions. As esophagitis is an issue with this alloy, fluoride in the physiological environment might affect corrosion rates. [16].

In this case, the presence of fluoride can come from toothpastes, water supply systems, and foods themselves. Understanding the corrosion mechanisms can provide information on how to control the material's corrosion rate in an environment that simulates the physiological environment, since Mg alloys are biodegradable biomaterials. Depending on the corrosion rates and corrosion products provided by this material, further surgical procedures for removal may not be required after implantation, resulting in a reduction in cost and likely a faster recovery for the transplanted patient. Among magnesium alloys (Mg), Mg alloys of the Mg-Al-Zn ternary system (AZ series) are the group with the widest industrial applications. AZ31-Mg alloys are the most affordable of the AZ series in terms of strength, ductility, and price. In addition, another important feature is that it is the most suitable composition for use in deformation processes [17]. The rollability of magnesium alloys at room temperature is adversely affected by their hexagonal close-packed structure. Consequently, it's critical to improve the formability of magnesium alloy plates [18]. H.V. Sun et al. They prepared a Mg-3Al-1La-Mg alloy and observed α-Mg and Al_4La phases in the microstructure. They also mentioned that the La element forms a needle-like phase [17]. S.B. Kang et al. observed that the AZ61 after hot rolling with Ce and La and reported that more re-nucleated grains were formed as the cross-sectional narrowing increased. However, magnesium's low

resistance to wear, creep, and corrosion combined with its high chemical reactivity make it less useful in many applications [18].

Magnesium alloys have very good casting properties. The processes used in casting magnesium alloys are high-pressure casting, semi-solid casting processes (thixocasting, thixomolding, and rheocasting), centrifugal casting, continuous casting, and sand casting [19]. The die-casting process offers advantages such as high production speed, the ability to produce thin-walled and complex-shaped parts with greater dimensional accuracy, longer mold life, and good casting surfaces, so most magnesium alloy parts used in automotive applications can be manufactured using this casting method [19]. However, wrought alloys are known to have better mechanical properties compared to cast alloys [20]. Magnesium-wrought alloy products are rolled products (plates, sheets, and foils), extrusion products (bars, tubes, and profiles), and forged products. For many automotive applications, the mechanical properties of wrought alloys are appropriate due to their superior strength and ductility compared to cast alloys. Extensive research on alloy kneading is being conducted to develop new alloy compositions and demonstrate the potential of various forming processes. The most important advance in this area is direct sheet metal casting plants using the double-roll continuous casting process [21].

Many industrial institutions, universities, and research institutes around the world have carried out laboratory and industrial experiments on magnesium alloy continuous casting technology. In many countries, especially Korea, Germany, Australia, China, Japan, Norway, Canada, and the USA, magnesium alloy sheets have been produced using the double-roll continuous casting technique [22].

1.2. OBJECTIVE OF THE WORK

The study aim to investigate the effect of hot rolling direction on biodegradation rate of magnesium alloys which are modified with Ca and Ce AZ31 in Hank's solutions after hot rolling process. An investigation will be conducted to analyze the impact of alterations in hot rolling orientations on the mean grain size, proportion of twinning, propensity for recrystallization, and rate of biodegradation. In order to assess the biodegradation behavior, we will conduct various tests including immersion,

electrochemical impedance spectroscopy andpotentiodynamic polarization. Immersion tests and electrochemical corrosion tests will be performed in compliance with ASTM B117 standard to investigate the corrosion behavior of AZ31 alloy samples prepared by casting process. Characterization studies of the samples will be carried out before and after the applied corrosion tests and the corrosion morphologies of the samples prepared using three methods will be examined.

PART 2

THEORETICAL BACKGROUND

2.1. MAGNESIUM AND ITS ALLOYS

2.1.1. Historical and General Aspects

The word "magnesium" originates from the city of Magnesia, which is located in Greece. Approximately 2.7% of the entire crust is composed of this element, making it the 8 most prevalent element in the Earth's crust. The concentration of Mg in ocean waters is 0.14%, which is equivalent to around 1.1 $kg.m^{-3}$ of the total. It is the sixth most prevalent element that is dissolved in ocean waters [23] . Even though the element magnesium wasn't officially recognized as an element until 1755, when Scottish scientist Joseph Black started to consider Mg as an element, it was already known in compounds like carbonates, hydroxides, and sulfates.

In 1795, scientist J.C. Delanethrie gave the name "magnesite" to some known salts of Mg, such as carbonate, nitrate, chloride, and sulfate. French scientist Alexandre Brongniart used the same term for a group of minerals, including carbonates and silicates. It was in 1808 that this term was first attributed solely to the mineral magnesium carbonate by the mineralogist Dietrich L. G. Karsten, which was then gradually accepted and applied [24]. In 1808, British scientist Sir Humphry Davy isolated a trace of magnesium from a combination of MgO and HgO.

By electrolyzing magnesium chloride ($MgCl_2$) in 1833, Michael Faraday produced the first metallic sample of magnesium. The German chemist Robert Bunsen is credited with introducing industrial production of metallic magnesium in a small laboratory in 1852.

In 1886, commercial production of magnesium began in Germany. From 1896 to 1916, the production and marketing process was exclusively carried out by the Griesheim- Elektron chemical products factory [23]. In the first half of the 20th century, initial applications began with light alloys, including Mg. However, there were still difficulties with their manufacture and the mechanical and corrosive properties had not yet been improved. For these reasons, Mg alloys were replaced in several applications by aluminum alloys and, from 1960 onwards, by plastics [23].

The low density of Mg alloys caught the attention of military forces, and during the Second World War, there was a peak in their production. There was a maximum consumption in 1944 of 228,000 tons. In 1998, world consumption was 360,000 tons, a value that grew by 7% per year [25]. The first car to use more than 18 kg of Mg until the 1960s was the Volkswagen Beetle, where it was applied to the transmission and air conditioning system.

A model weighing about 39.5 kg of magnesium was introduced by Ford in 1998. Fiat introduced its first single-mold magnesium rim in 1967. Porsche began producing light alloy wheels and interior trim parts made of magnesium in 2005. In the mid-19th century, Paris began commercial magnesium manufacturing using the Deville-Caron method, which employs potassium to decrease magnesium in a heated container. The final form was available as powder or threads for many years and was commonly used in photography. From 1900 onwards, world production reached a mark of 10 tons of magnesium per year, in 1915 annual production reached 350 tons. From then on, many other countries, such as the United States, began production and annual volumes increased to 3,000 tons by the last year of World War I. In 1939 production reached 32,000 tons per year. In the 1990s, Western production reached about 250,000 tons per year [26].In the health area from the 20th century onwards, the superiority of bioabsorbable implants composed of magnesium and its alloys in relation to those composed of polymers was recognized due to mechanical properties and toxicity [27].

Currently, the automotive industry is the primary user of magnesium alloys, primarily for the purpose of lowering fuel consumption and, in turn, greenhouse gas emissions and non-renewable resource preservation.

2.1.2 Magnesium and Its Alloy

As the lightest structural metal, magnesium serves as the basis for several commercial alloys used in a variety of industries. It comprises around 2.7% of the Earth's crust and isconsidered an abundant element. In nature, it cannot be obtained directly in metallic form and is found in the form of oxides such as magnesite ($MgCO_3$) and dolomite ($MgCO_3$. $CaCO_3$). Its largest source is found in ocean water, constituting about 0.13% of all oceans [26] . Alkaline earth magnesium has a compact hexagonal structure. Compared to aluminum and steel, this metal has a lighter structure and lower density [28]. Table 1 presents the density of magnesium compared to that of aluminum and steel.

Table 2.1. Magnesium density in relation to steel and aluminum [29].

Material	Density (g/cm^3)
Magnesium	1.7
Aluminum	2.7
Steel	7.8

Its low mechanical strength and poor resistance to oxidation and corrosion make it uncommon for structural applications to use it in its pure form [30].

In engineering, magnesium has little application unless it is alloyed with another metal. Magnesium is combined with certain metals, such as aluminum, zinc, zirconia, silver, and thorium, to provide it mechanical strength and light weight for structural uses [26].

Magnesium and its alloys exhibit mechanical and physical properties more similar to those of human bone than other biomaterials. This eliminates any elastic incompatibility between an implant and bone, and magnesium is also present in the bone's natural structure and is one of the metals required for metabolism. The body readily dissolves magnesium and its alloys. Its recent application as a biomaterial is due to the fact that it is one of the primary metals naturally occurring in the body, has sufficient mechanical properties, is biodegradable and compatible with bone.

Biodegradable magnesium-based alloys typically consist of four groups. All of these consist of pure magnesium, alloys with aluminum (AZ31, AZ91, LAE422, AM60), alloys with rare earth elements (AE21, WE 43) and alloys without aluminum (WE43, MgCa0.8, MgZn6)). To give these alloys the mechanical and physical properties required for use in the orthopedic field, the coating process, grain size optimization, increased corrosion resistance and reinforced intermetallic formations are carried out. [31].

Table 2.2. Mechanical properties of some biomaterials [10].

Alloy	Symbol	ρ (g/cm^3)	σ_y (MPa)	σ_t (MPa)	E (GPa)
Natural Bone		1,8 –2,1	104–121	110–130	15 - 25
Magnesium and its alloy	Pure Mg AZ31 AZ91 WE43	1,74–2 1,78 1,81 1,84	65–100 185 160 170	90–190 263 150 220	41 – 45 45 45 44,2
Iron and Manganese alloy	$Fe_{20}Mn$ $Fe_{35}Mn$	7,73 -	420 230	700 430	207 -
Zinc-based alloys	Zn-Al-Cu	5,79	171	210	90
Stainless steel	SS316L	7,9	190	490	200
Titanium and its alloys	Ti_6Al_4V Ti_6Al_7Nb	4,43 4,52	880 800	950 900	113,8 105
Cobalt-chromium alloy	$CoCr_{20}Ni_{15}Mo_7$	7,8	240 - 250	450 - 960	195 - 230
Bioceramic material	Al_2O_3	4	-	400 – 580	260 – 410
Polymers	PLGA PCL	1,30 – 1,34 1,145	3,8 – 26,6 8,37 – 14,66	13,9 – 16,7 68,45– 102,7	1,69 281 - 686

The commercial magnesium alloys produced for the automotive industry as implant materials are currently the most researched magnesium alloys [32]. Magnesium alloys are generally designated using the American Society for Testing and Materials (ASTM) nomenclature [33] which employs a standard letter-figure combination. Al-containing alloys, alloys without Al, and pure magnesium (Mg) with traces of other elements are the three main categories of magnesium alloys [34]. The following are typical magnesium alloys containing aluminum: AE21, AZ91, AZ31, LAE442, and AZ alloys modified by calcium (Ca). For many years, AZ31 and AZ91 have been employed in technical applications. WE, MZ, WZ, and magnesium calcium alloys are among the most prevalent Al-free magnesium alloy systems. In order to enhance stability and resistance to creep at elevated temperatures, the magnesium alloy WE43 was formulated. You may find yttrium (Y), zirconium (Zr), or RE in this alloy. The properties of manganese-zinc alloys (MZ) are similar to those of the ZM alloy system, which is widely recognized in the transportation industry for its use in forging applications. However, biodegradable implant materials have not yet been completely developed from the aforementioned alloys. The attribution of the observed in vivo degradation to a chemical element, an intermetallic compound, or a microstructural effect resulting from the processing route remains ambiguous, owing to the intricate composition of the alloy. [2].

2.2. CLASSIFICATION OF MG ALLOYS

Mg alloys can be classified into two groups, the first of which contains alloy that have an aluminum content that varies between 1% and 9 % and other elements in a lower percentage such as manganese and zinc [35]. It has a wide variety and low price and has good mechanical properties at temperatures up to 120°C. The other group includes alloys containing elements such as rare earths, thorium, zinc, or silver containing a small percentage of zirconia. These alloys have better mechanical behavior, but their manufacturing process has higher prices [36].

The identification of magnesium alloys is carried out according to the chemical composition, in addition to thermal and mechanical treatments, according to the ASTM standard, adopting alphanumeric characters. The two main elements present

in the alloys are represented by the first two letters, while the numbers are related to the nominal contents of each element. The letter after the numbers represents other elements added in smaller proportions. The thermomechanical treatment used is represented after the hyphen. Table 2.3 shows the alloying elements and their respective letters for representation [26]. To identify the different alloys, a specific nomenclature is used (Table 2.3) [37]. The AZ31 alloy, for example, contains approximately 3.0% Al and 1.0% Zn, the remainder being mostly Mg and some elements in amounts less than 0.1% by mass.

Table 2.3. Magnesium Alloying Elements ASTM Code [37].

A: Al	**B**: Bi	**C**: cu	**D**: Cd	**E**: Rare Earth
F: Fe	**G**: Mg	**H**: Th	**K**: Zr	**L**: Li
M: Mn	**N**: Ni	**P**: Pb	**Q**: Ag	**R**: Cr
S: Si	**T**: Sn	**W**: Y	**Y**: Sb	**Z**: Zn

Thermal and thermomechanical treatments are represented by:

F = manufactured,

O = annealed,

H10 to H11 = slightly hardened,

H23, H24, H26 = hardened and partially annealed,

T4 = solubilized,

T5 = artificially aged,

 T6 = solubilized and aged artificially,

T8 = solubilized, cold worked and artificially aged.

Thus, a magnesium alloy named AZ92A-T6 has 9% aluminum and 2% zinc in its basic composition (A) and is subjected to solubilization and aging heat treatment with the aim of obtaining maximum hardness (T6) [26]

In addition, Table (2.4) for the most commonly used alloys containing a main alloying element such as aluminum (AZ, AM, AS, AE, and AT series) shows that magnesium alloys can be welded in an inert gas environment.

Table 2.4. Typical magnesium alloys and its uses [38].

Magnesium alloys	Alloying elements	Production	Properties
AZ91	9%Al 0.7%Zn 0.13%Mn	General casting alloy	Excellent molding and mechanical qualities at temperatures below 150ºC.
AM60	6%Al, 0.15%Mn	High pressure casting	Slightly less strength but slightly higher toughness and ductility than AZ91. A common use in automotive structural applications.
AM50	Mg-Al	General casting alloy	Excellent molding, energy absorption, ductility, and strength qualities.
AE44	Mg-Al with rare earth elements		Superior molding and deformation properties compared to AE42.
AE42	Mg4 atomic percentage Al2 atomic percentage rare earth		Good deformation behavior and low molding level.
AS41	4.2%Al, 1%Si		Strengther than AZ91, but better against creep resistance at high temperatures.
ZE41	4.2% Zn, 1.2% Terras Raras, 0.7% Zr	special casting alloy	Reducing the deformation resistance at high temperatures is achieved by adding rare earths. strong force.
AZ31	3% Al, 1%Zn, 0.2% Mn	forged magnesium products	Good alloy for extrusion
AM20	Mg-Al	casting alloys	Strong, low molding, high ductility.
MRI 153M	Mg-Al-Ca-Sr		For high temperature applications, up to 150°C.
MRI 230D	Mg-Al-Ca-Sr		for applications requiring high temperatures—up to 190°C.
AS 21	Mg-Al-Si		For application at temperatures above 120°C
AJ62	Mg-Al-Sr	High pressure casting	Excellent resistance to heat, mechanical stress, corrosion, and deformation, as well as casting.

Magnesium alloys are highly sought after for use in a variety of industries, including electronics, aerospace, and most notably the automotive sector, due to their great specific mechanical properties and recyclable nature. [39, 40]. The interest in the biomedical sector has also been growing in relation to magnesium due to it being a

biocompatible and bioabsorbable metal, enabling the production of temporary implants depending on the composition of the alloy [31, 41].

2.3. ALLOYING ELEMENTS

Magnesium in bulk degrades too quickly and has low strength [42]. Therefore, by using the right alloying and processing techniques, the properties of the material can be improved. Intermetallic compounds are formed when chemically active magnesium combines with alloying materials. By changing the microstructure, these intermetallic phases found in magnesium alloys affect the material properties [38]. Alloying elements directly improve the mechanical properties through precipitation hardening, grain refinement strengthening and solid solution strengthening [43]. To strengthen their matrix, magnesium is alloyed with elements whose solubility is strongly dependent on temperature. For magnesium, one of the most important factors affecting solubility is the atomic size of the element [26]. The atomic diameter of magnesium (Mg) is 0.320 nm and its hexagonal close-packed structure (HCP) allows the formation of solid solutions with a variety of elements (c/a = 1624). [28]. Intermetallic phases formed in binary Mg alloys are listed in Table 2.5

Table 2.5. Intermetallic phases formed in Mg alloys [44].

system	Phase	Melting Point (℃)	system	Phase	Melting Point (℃)
Mg_Al	$Mg_{17}Al_{12}$	402	Mg_Sm	$Mg_{62}Sm$	-
Mg_Ca	Mg_2Ca	714	Mg_Gd	Mg_6Gd	640
Mg_Sc	MgSc	-	Mg_Tb	$Mg_{24}Tb_5$	-
Mg_Mn	Mn	1245	Mg_Dy	$Mg_{24}Dy_5$	610
Mg_ Zn	MgZn	347	Mg_Ho	$Mg_{24}Ho_5$	610
Mg_Y	$Mg_{24}Y_5$	620	Mg_ Tm	$Mg_{24}Tm_5$	645
Mg_Zr	Zr	1855	Mg_Yb	Mg_2Yb	718
Mg_Ag	Mg_3Ag	492	Mg_Lu	$Mg_{24}Lu_5$	-
Mg_Sn	Mg_2Sn	770	Mg_Tl	Mg_5T_{l2}	413
Mg_Nd	$Mg_{41}Nd_5$	560	Mg_Th	$Mg_{23}Th_6$	772

2.3.1. Aluminum (Al)

Magnesium is the most favourably affected mineral. By 180 MPa, the strength of an alloy is increased by the presence of aluminum. This results in its most frequent alloying with magnesium (Mg) alloys. In order to subject an alloy to heat treatment, its aluminum content must exceed 6% by weight[26]. Al is soluble in magnesium at a rate of approximately 12 weight percent; however, this value is temperature dependent. Aluminum is less soluble in alloys abundant in Al at room temperature. An excess of 3 weight percent Al accelerates corrosion by enhancing the cathodic reaction [45]. When Al is introduced into Mg, the kinetics at the anode decrease below the solubility limit. The Mg-Al binary phase diagram is shown in Figure 2.1. Durability increases because intermetallic $Mg_{17}Al_{12}$ is developed at low temperatures (120 °C).
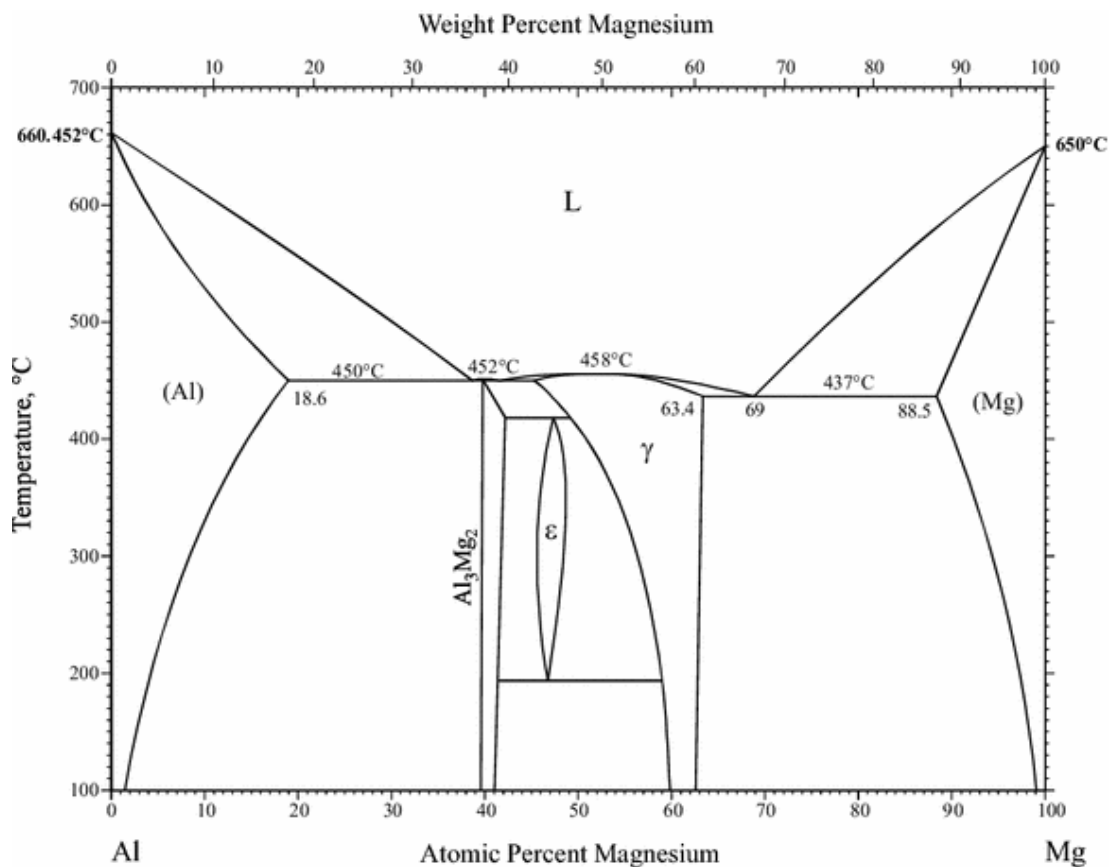
Figure 2.1. Mg-Al binary phase diagram [46].

2.3.2. Tin(Sn)

Tin forms thermally stable Mg_2Sn precipitates in the presence of trace quantities of aluminum, reducing hot shear in hot forming processes [26, 47]. Figure 2.2 of the Mg-Sn binary phase diagram shows that only Mg_2Sn precipitates in binary alloys. Tin's maximum solid solubility in magnesium is 14.85 wt% at 561 °C, the eutectic transition temperature. This value reduces rapidly to 0.45% by weight at 200 °C and approaches zero at room temperature [48]. Tin may be precipitated as Mg_2Sn, a compound with a higher melting point (770 °C) than $Mg_{17}Al_{12}$, which is thermally unstable at lower temperatures due to its reduced solubility [49].
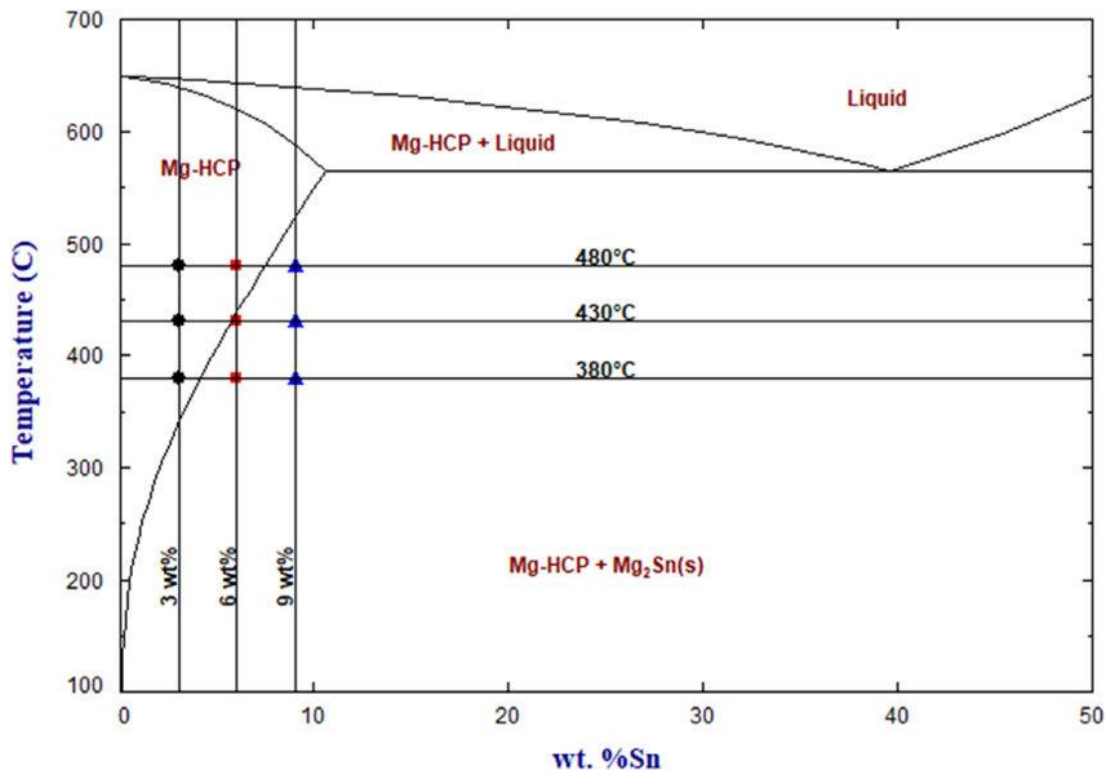
Figure 2.2. Mg-Sn secondary phase diagram [50].

2.3.3. Titanium

Due to its high mechanical strength, thermal stability, and low density, Ti is insoluble in magnesium and lowers grain size in magnesium alloys. Ti elements reduce magnesium alloy grain size. Figure 2.3 displays Mg-Ti binary phase diagram.
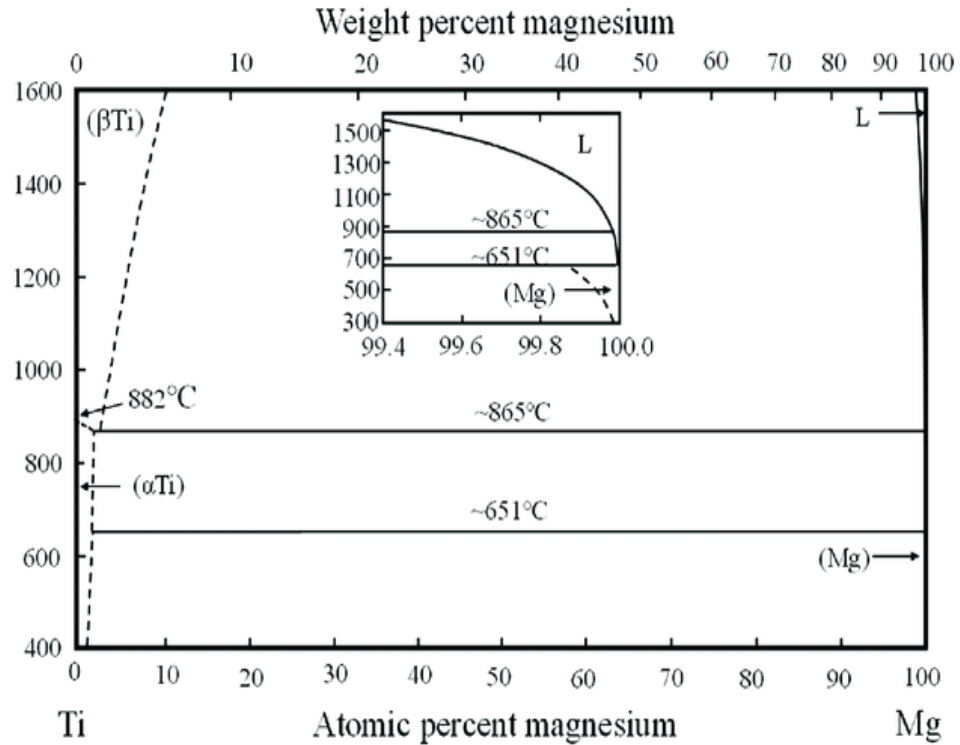
Figure 2.3. Mg-Ti binary phase diagram [51].

2.3.4. Zinc (Zn)

Zinc comes fourth behind iron, aluminum, and copper in melting and boiling points (419.5 and 907 °C). Although it is not as strong or hard as copper or aluminum, it is still stronger than tin and lead. Demanding applications cannot use pure metal because it is too fragile. Because of these factors, zinc is often alloyed or coated with steel or iron. Full-strength zinc roofs are usually made of simple wrought iron because zinc, unless extremely pure, is brittle at room temperature and becomes malleable and easily rollable at around 100°C. However, corrugated sheets become more useful for roofing when tiny amounts of titanium and copper are added to

16

increase their creep resistance. The global supply of zinc increased to 13.4 million tons[52]. compared to demand of 13.77 million tonnes. Approximately 20-40% of zinc produced worldwide is recycled [53]. Steel galvanized with half zinc is protected from corrosion. Iron and magnesium can be easily replaced with zinc, which is biodegradable [16]. Fifteen percent of the world's zinc is used to make alloys. You can choose from forged zinc alloys, drawn wire, forged ingots and applied extrusion. New zinc alloys for extrusion and forging are available. Research shows zinc's secondary phase with magnesium. Figure (2.4) shows that $MgZn_2$ dissolves at 595 °C and becomes eutectic at 368 °C with 97% Zn. It has no defined melting ranges [54].
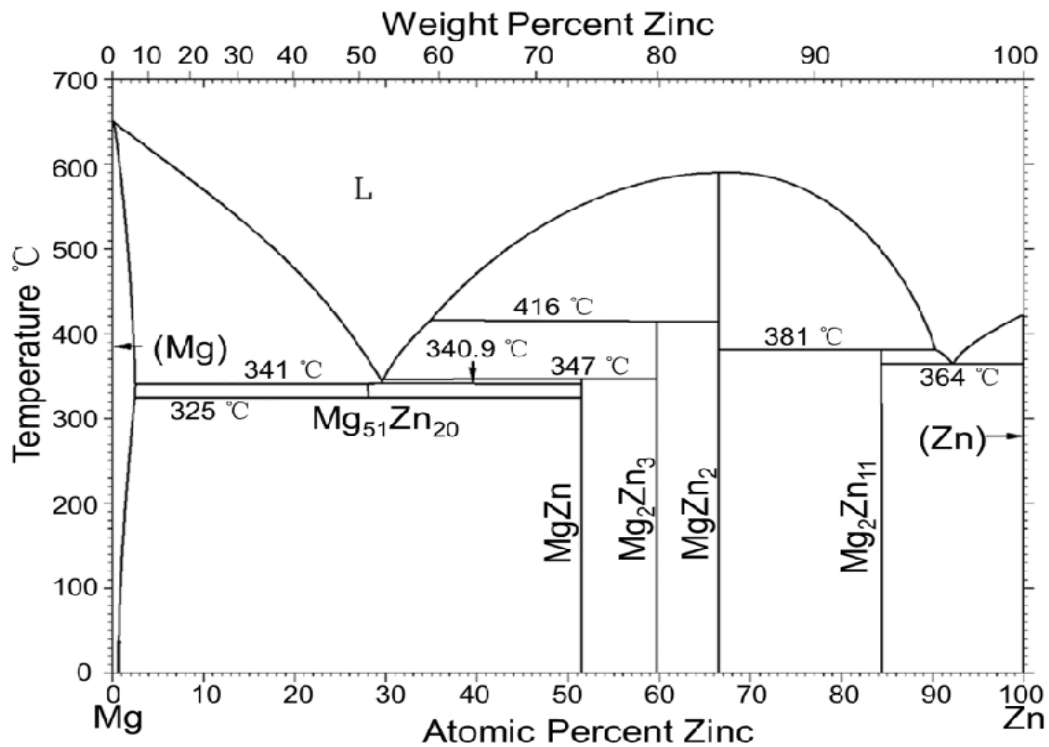
Figure 2.4. Mg-Zn secondary phase diagram [55].

2.3.5. Manganese (Mn)

Manganese (Mn), a micronutrient that is chemically active in pink, is necessary for the majority of organisms. It oxidizes easily but is brittle and hard. Pure manganese rusts like iron when it comes into contact with water and air and dissolves in weak acids. Manganese is necessary to make both steel and iron. Between 85 and 90

percent of the total demand is met by the steel industry. Many inexpensive stainless steel compositions and aluminum alloys contain manganese. In addition to discoloring glass, manganese can also produce violet glass; South Africa produces over 82% of the world's manganese; manganese steel is cheap and corrosion-resistant; and manganese has been seen in a secondary phase with magnesium in the past. Mn dissolves at a rate of 2% (atomic) at 653 °C. The Mg-Mn binary phase diagram does not show any intermediate compositions Figure (2.5) [54].
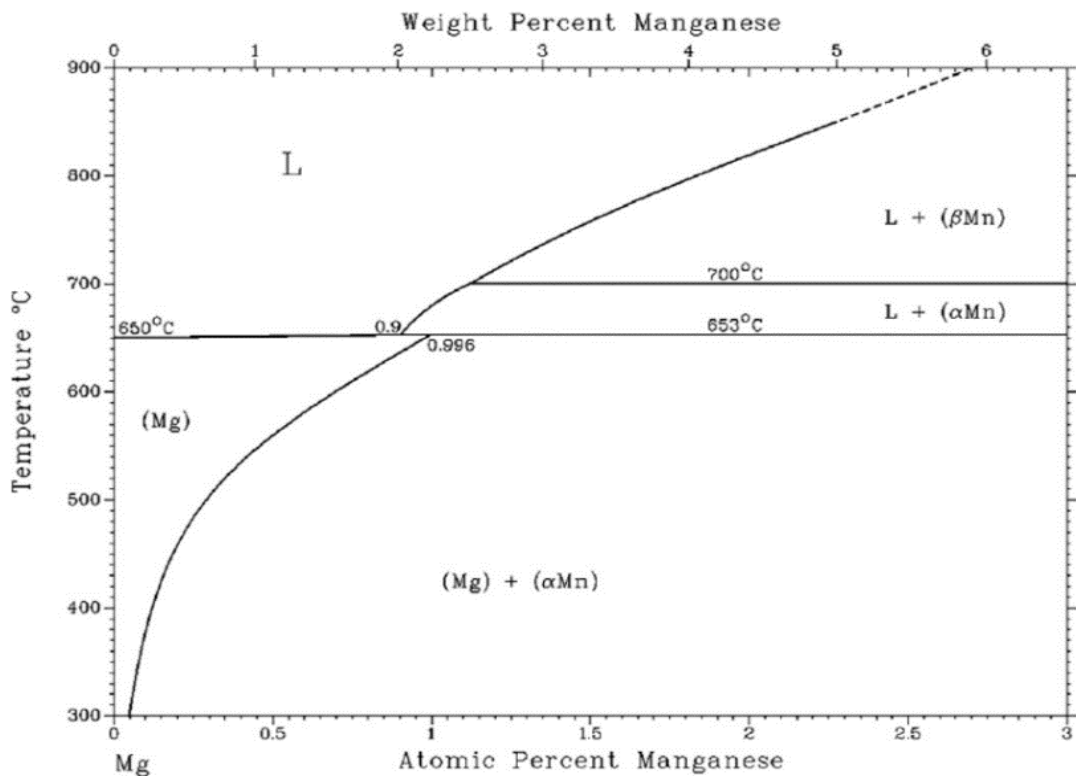
Figure 2.5. Mg-Mn secondary phase diagram [55].

2.3.6. Gadolinium (Gd)

Gadolinium forms a protective white oxide in moist air. It is very soluble in weak acids and forms water slowly when combined with colorless salts. Trivalent components are found in compounds. Gadolinium exhibits higher magnetism than nickel at 20 °C. Binary-nitrogen-sulfur-carbon-phosphorus-selenium-boron-silicon-arsenic compounds are produced by this metal at high temperatures [56]. Gadolinium is used by the majority of materials scientists to enhance several alloys. The

corrosion and creep resistance of magnesium alloys are improved by rare earth elements like Ce, La, Gd, and Nd. In the -Mg matrix, highly soluble rare earth elements form a solution that becomes the solid forming magnesium and strong alloys, while rare earth elements form the intermetallic consolidation phase that remains stable even at elevated temperatures. Gallium becomes silvery white through deoxidation. With oxygen or moisture, gadolinium gradually develops a black coating. The magnetism of the element is enhanced at this temperature. It only occurs in oxidized form in nature. When separated, it frequently has rare earth impurities due to their chemical resemblance [57]. In previous studies, a secondary phase of gadolinium with Mg was observed. The solid melt hardens because, as Figure 2.6 shows, magnesium dissolves at the eutectic temperature up to 23.49 percent (in percent Gd).[58].
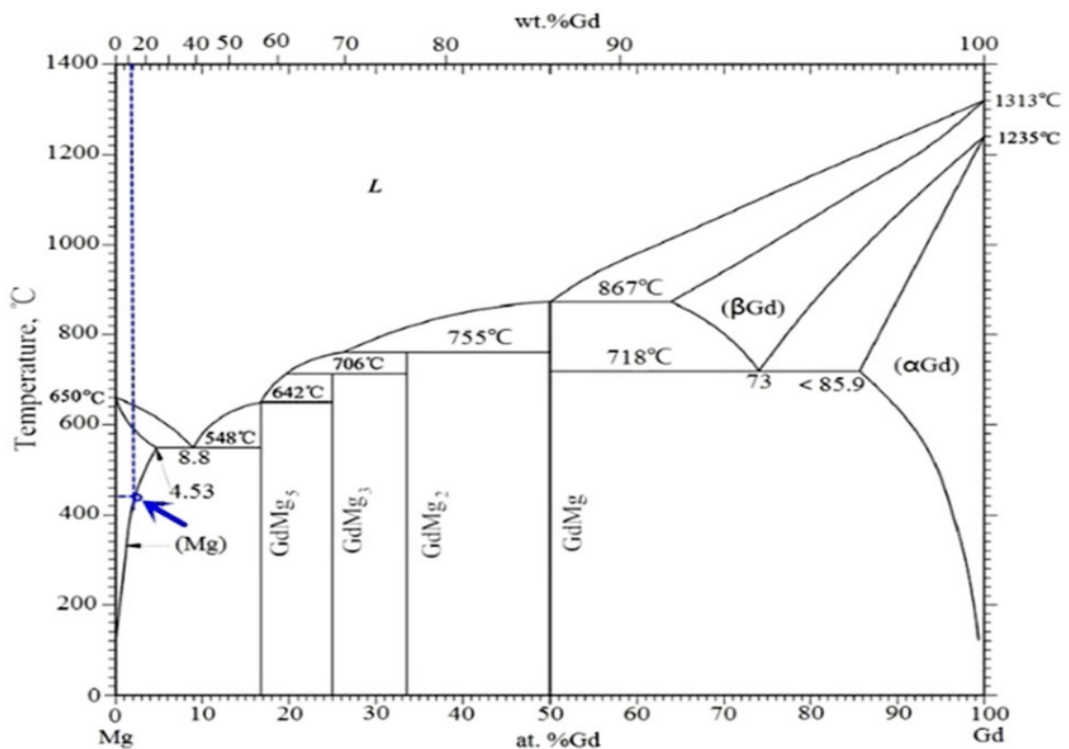
Figure 2.6. Mg-Gd secondary phase diagram [59].

2.3.7. Lanthanum (La)

Pure lanthanum is soft and malleable element. After europium, it is the second most reactive rare earth metal. In normal air, La oxidizes to lathenohydride. Despite its

19

slow water interaction, its thin fluoride (LaF3) layer enables it to dissolve quickly in dilute acids (except HF acid). From 6 K (267 C) to its melting point at 1,191 K (918 C), the metal is magnetic due to its nearly temperature independent magnetic sensitivity between 4 and 300 K (269 and 27). Seldom added rare earth elements such as lanthanum strengthen alloys made of magnesium and aluminum. These enhancements strengthen the alloy while reducing its weight, making it ideal for lightweight, durable goods [57]. Rare earth elements boost magnesium alloy yield strength. Lanthanum possesses a magnesium-containing secondary phase, according to studies. Figure 2.7 shows that La has a high eutectic temperature at 612 °C and low solubility of Mg. Its poor resolution hinders aging [58].
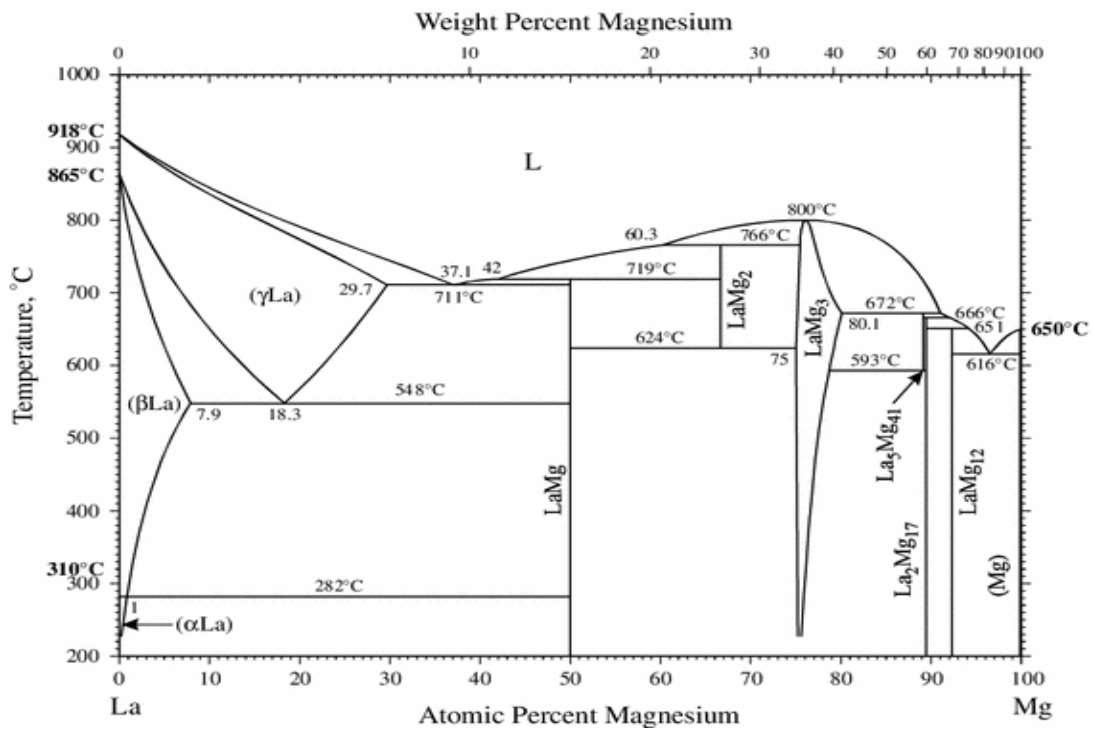
Figure 2.7. Mg-La secondary phase diagram [60].

2.3.8. Calcium (Ca)

Calcium alloying emerged with the development of high creep resistance but inexpensive alloys. Thus, the replacement of the $Mg_{17}Al_{12}$ phase with the Al_2Ca phase was achieved. The maximum solubility of calcium in magnesium is 1.34% at 565 ^{0}C. While calcium improves the rolling ability of sheets, exceeding 0.3% by

weight negatively affects the welding ability. Adding 1% Ca to Mg alloys not only improves the creep resistance of the alloy but also increases the tendency towards hot tearing [51]. Figure 2.8 shows the Mg-Ca balance diagram.
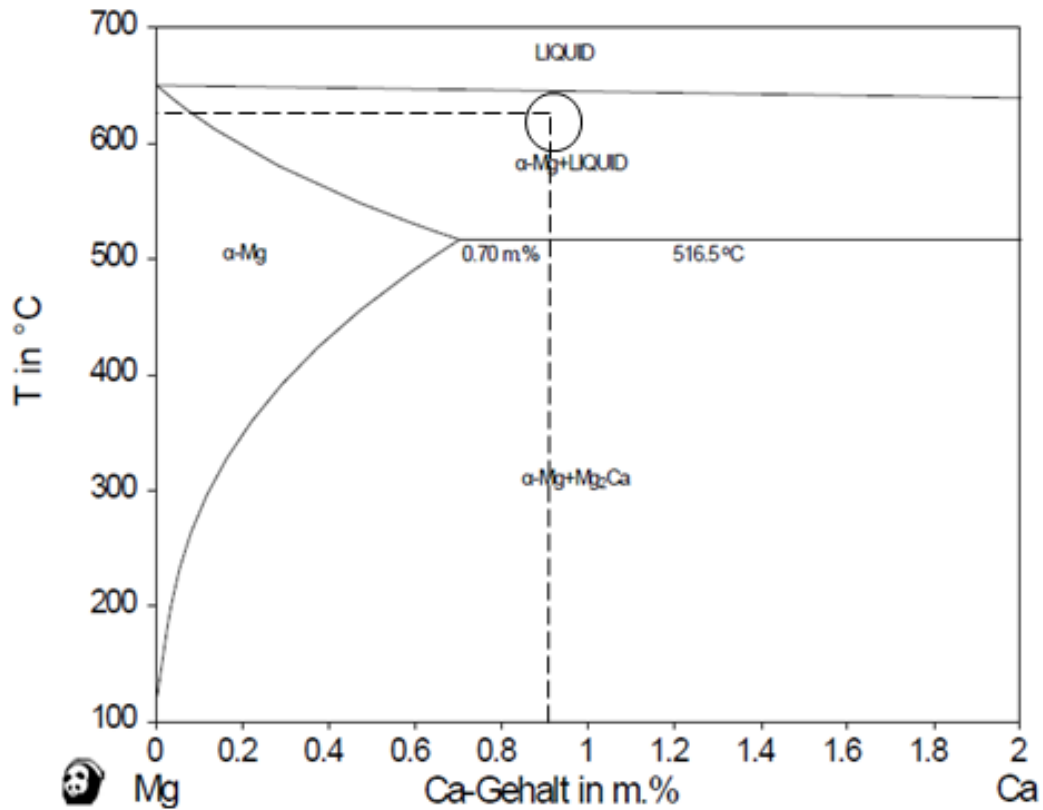
Figure 2.8. Mg-Ca secondary phase diagram [61].

2.3.9. Other alloying elements' effects.

Zinc is the most effective and often used element in magnesium alloys [62]. It is used with aluminum to improve strength. Zinc displaces Ni and iron impurities, improving the corrosion resistance of Mg (magnesium) alloys [38]. The zinc tolerance limit in milligrams is 2.5% by weight [38]. The tolerance limit for zinc in mg is 2.5% by weight [63]. However, research show that increasing the zinc content from 1 to 3 wt.% causes increased corrosion rates [64]. An increase in zinc content resulted in a proclivity for stress corrosion cracking. The most vital vitamin in the human body is

zinc. More than 85% of Zn is found in bones and muscles. Zinc is 6.2 wt% soluble in magnesium [42]. Zinc inhibits hydrogen evolution during biocorrosion [62].

Due to uneven load transmission between the implant and bone, the healing process in biomedical implants may be significantly affected by zinc alloys, despite their identical strength to magnesium alloys. This is because zinc alloys have a greater elastic modulus. Magnesium dissolves calcium at a rate of 1.34 percent under equilibrium circumstances[42]. As a result, magnesium alloys' mechanical and thermal characteristics are enhanced [65]. When magnesium alloys are heated and cast, it slows down the oxidation of calcium. Magnesium sheets can be made more rollable by adding calcium, although adding more than 0.3% causes the sheets to break when welded [26].

A biocompatibility rating of 1 wt.% for calcium added to magnesium is considered appropriate for use in biomedical applications [42]. Magnesium alloys corrode at an extraordinarily rapid rate above their solubility limit, which is at 1.34 percent by weight. One factor affecting corrosion resistance is the reduced solid solubility of copper in magnesium [26] . Magnesium and copper combine to generate Mg_2Cu. The typical restriction for copper in magnesium is 0.1 weight percent, but when aluminum and manganese are included in the alloys, the limit decreases to 0.01 weight percent [63].

Because beryllium is only slightly soluble in magnesium, it can be used in concentrations of up to about 0.001% by weight to minimize the surface oxidation tendency of molten metal during melting, casting and welding. Due to its grain-coarsening effect, it is unsuitable for sand-casting alloys, but is well suited for die-casting and wrought alloys[26]. Iron is both toxic and tolerable in terms of corrosion resistance with a magnesium level of up to 0.005%. It is a common contaminant found in magnesium alloys. Since iron is so poorly soluble in magnesium (around 0.001% by weight), it is possible to get pure iron [28].

Since Mg_3Nd is a better cathode than pure Mg and causes an increase in corrosion kinetics with increasing Nd concentration, the formation of the Mg_3Nd phase in Mg-Nd binary alloys accelerates decomposition. However, the rate of corrosion increase

is lower for Nd compared to La or Ce. In Mg-Al alloys, Nd increases corrosion resistance by reducing the galvanic coupling that occurs in AZ or AM alloys without Nd. In addition, it influences the development of a protected rare earth, magnesium and neodymium-based oxide layer on the surface.

2.4. MAGNESIUM ALUMINUM ALLOYS

Aluminum alloys are among the most commonly used metals in industry and mechanical engineering. After steel, aluminum is the most commonly used building material in industrial applications. Al is one of the most commonly used materials in Mg alloys because it contributes to mechanical and physical properties and is a cost-effective alloying element due to its occurrence in nature. The density of aluminum is 2.71 g/cm^3. In practice, Mg-Al ultralights appear to consist of solid solution δ-dendrites rich in magnesium and α-crystals with sufficient aluminum content. A solid solution is created with the composition $Mg_{17}Al_{12}$, which has a δ,α-internal structure [66]

There is a eutectic reaction at 437 °C in the binary Mg-Al equilibrium diagram. Phases $L \leftrightarrow Mg_{17}Al_{12} + \delta(Mg)$ are formed by the eutectic reaction, which yields molten magnesium and aluminum. At this particular eutectic temperature, aluminum has a maximum solubility of 12.7%. And when the temperature is room temperature, the solubility decreases to roughly 2%. According to the presented properties, the Mg-Al alloy system can produce alloys with good precipitation hardening, solid solution hardening, and castability [66].

Figure 2.9 shows that intermetallic $Mg_{17}Al_{12}$ is visible in the casting microstructure of Mg-Al alloy systems containing more than 2 percent aluminum. A phase difference causes the ductility and brittleness of the alloys to decrease or increase as the aluminum content increases above 7%. The intermetallic $Mg_{17}Al_{12}$, whose network structure is not yet fully developed, is distributed along the grain boundaries.

At ≈700 K, the solution causes the intermetallic $Mg_{17}Al_{12}$ to dissolve, resulting in solid solution hardening, which in both cases leads to an increase in tensile strength, and ductility. $Mg_{17}Al_{12}$ intermetallic compounds can precipitate between 373K and 473K, and, these precipitate particles increase tensile strength. However, Mg-Al alloys do not have the necessary properties to be used as structural materials. To improve the properties, elements such as Zn, Mn, Si, and rare earths are added to the Mg-Al alloy system [67, 68].
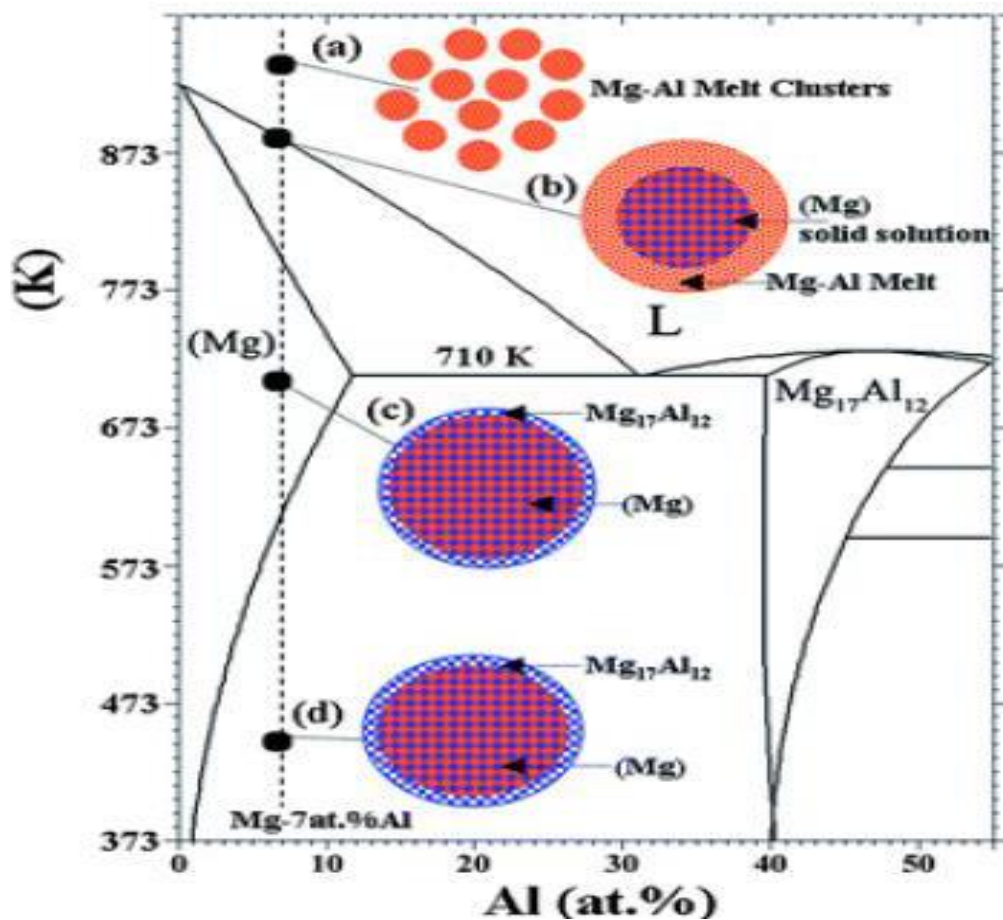
Figure 2.9. Magnesium-rich part of the Mg-Al system [69].

The magnesium-aluminum alloys AZ91, AZ31 and AM 60 are most commonly used in industrial applications. AZ series alloys have very high castability. Due to their good formability and ductility, AM60 series alloys are used in the automotive industry to make rims. since their composition contains rare earth elements., AS and

AE series magnesium alloys can withstand high temperatures for extended periods of time.

2.4.1. AZ91 Alloys

The automotive industry is particularly interested in the AZ91 alloy. The aim of current research is to improve the desired mechanical properties and plastic formability of this material. AZ91 series is the most widely used commercial Mg structural alloy due to its good casting properties and mechanical properties. AZ91 alloy has gained in recent studies attention as its use as a chill casting material in the automotive industry. The calcium content of this alloy has been studied to reduce oxidation, increase leak safety at the material boundary, and increase thermal resistance (130-150°C). However, increasing the calcium content beyond 0.2% makes the alloy brittle. [70]. AZ91 shows its best properties at room temperature. It has been studied that properties such as fatigue strength, creep strength, and dielectric strength give the best properties at room temperature without being exposed to thermal action [71].

2.4.2. AZ31 Alloys

AZ31 alloy garners significant interest due to its low cost and excellent mechanical properties at room temperature. Additionally, its castability is very high. AZ series alloys, which have low thermal resistance, may not exhibit the same mechanical properties when heated to high temperatures. [72]. Although they have low thermal stability, the main reason why they are preferred is the advantage of gaining weight due to their lightness. They are much lighter than aluminum and steel materials. The most commonly used plate is the AZ31 alloy. Because of their mechanical properties that closely resemble bone tissue and low density, aluminum-added magnesium alloys are the preferred choice for materials, particularly in orthopedic applications. In the binary system of Al and Mg, the most favored types are AZ31 and AZ91 [73]. Because Al is present in the structure, it has corrosion resistance that is significantly higher than that of pure magnesium in addition to having mechanical qualities that are similar to those of bone. The surface develops a passive oxide layer as a result of

Al$_2$O$_3$ formation during corrosion, which strengthens the material's resistance against oxidation. Biocompatibility performance is enhanced by this. They are not appropriate for long-term implantation, though, because of Al's toxic effects[74].
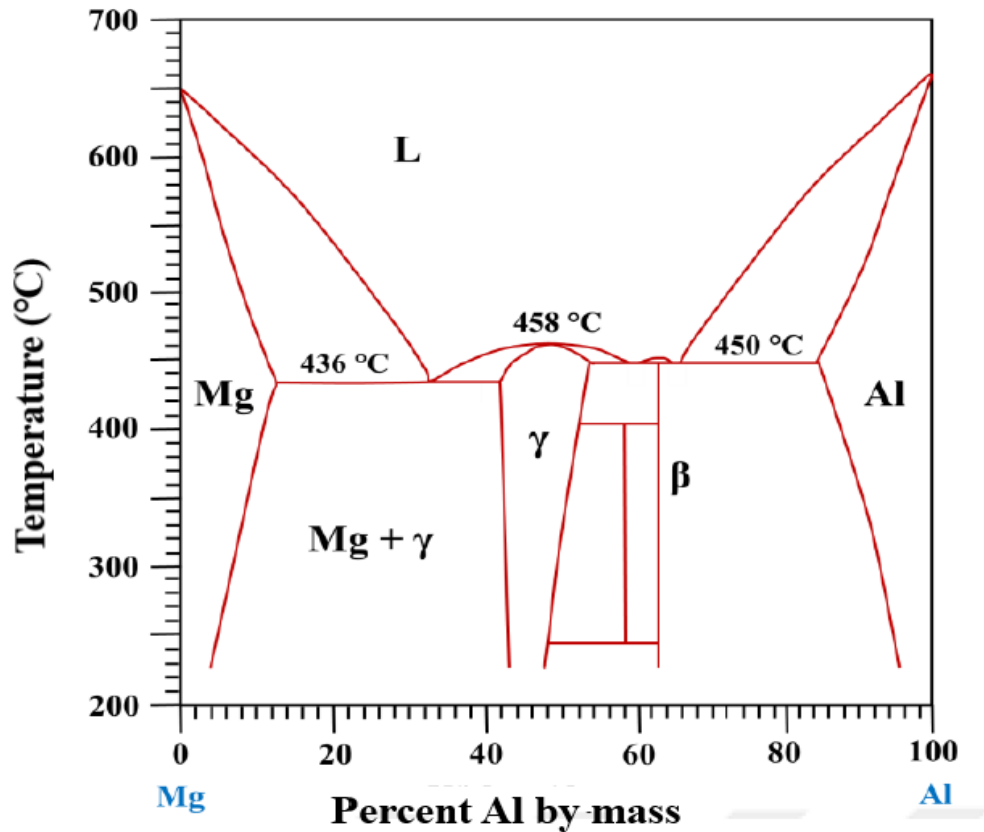
Figure 2.10. Mg-Al phase diagram[75].

2.5. IN VITRO AND IN VIVO DEGRADATION OF MG ALLOY

The rapid degradation rate of Mg alloys leads to harmful effects on organisms and the mechanical integrity of human tissues [37]. This rapid degradation stems from the excessively negative electrode potential of Mg alloys, rendering them vulnerable to decomposition in electrolytic aqueous environments. To curb the degradation rate and mitigate harmful interactions, a thorough understanding of the degradation mechanism, particularly under physiological conditions, is imperative [36]. Numerous studies have been carried out to understand the degradation mechanism [76]. Sodium chloride solution (NaCl), simulated body fluid (SBF), Hank balanced

26

salt solution (HBSS), Dulbecco modified eagle medium (DMEM), etc. For in vitro immersion testing, there are numerous options [77]. The degradation rates obtained after RE solutions can vary greatly [78]. According to Figure 2.11, ions like calcium, phosphate, sulfate, carbonate, and chloride are generally thought to have an impact on the rate of degradation of inorganic substances. The degradation potential falls with increasing concentration of chloride. In the physiological milieu, magnesium alloys are attacked and the dissolution of magnesium is accelerated by carbonate and sulfate ions. A more effective protective layer in the SBF solution is produced by higher concentrations of HCO^{3-} ions, according to some studies [79]. In SBF solution, phosphates and calcium ions are essential for the formation of hydroxyapatite (HA) and other Mg/Ca phosphate salts. [79].
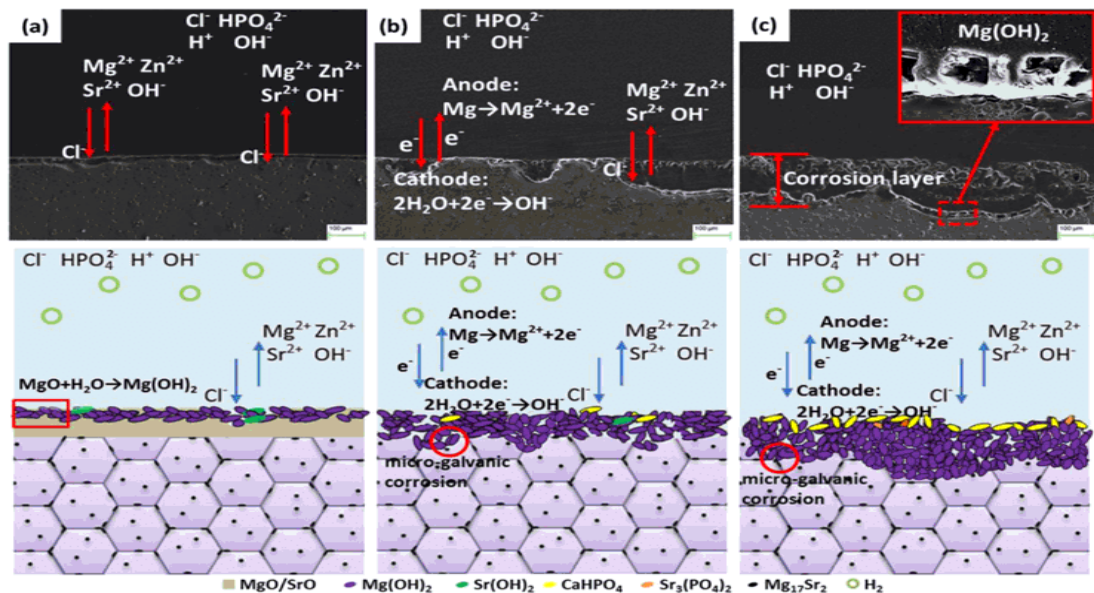
Figure 2.11. The reactions between Mg alloy and SBF are shown in the diagram: (a) galvanic reaction between the substrate and H2O, (b) dissolution of Mg(OH)2, and (c) precipitation of phosphates [80].

Other research, however, have shown that proteins accelerate the breakdown of Mg alloys. This is due to the presence of different metal cations, which, to some degree, increase the breakdown rate of proteins [37]. Electrochemical investigations revealed a synergistic impact of insoluble salt production and protein adsorption on Mg degradation [81]. Mg alloys degrade more faster in vitro than in vivo, particularly when no protein is present. Mg alloys degrade at different rates in different

anatomical locations of the human body [82]. As a result, the physiological environment has a large impact on the deterioration behavior and microstructure of Mg alloys [82]. To understand the degradation process, it is required to evaluate the degradability of Mg alloys under physiological settings. The use of suitable solutions is critical for assessing in vitro degradation [82]. The impacts of Mg alloys, inorganic chemicals, proteins, and cells are reciprocal throughout the degradation process. Extensive research, however, has explained the degradation process by investigating the interplay between degradation, proteins, and cells.

There was a quest for a therapy for peri-implant infections in the 1990s. A growing number of animal investigations and clinical outcome reports in people have been published [83]. The most common method to determine the amount of new bone and the degree of re-osseointegration (direct structural and functional connection between) to determine living bone tissue and the implant surface under load is biopsy with histological examination. Some studies[84], have limited measurements of the amount of new bone until surgical reentry. Some studies examined the height of the growing bone adjacent to the implant (not separated by a connective tissue capsule), which is better. Other studies [85]. assessed the rate of new bone formation to the most coronal (lateral vertical) bone tip (including bone separated from the implant by a connective tissue capsule). Other studies employ systemic antibiotics to treat infections, with the majority of existing studies employing postoperative (post-operative) systemic antibiotics such as metronidazole (nitroimidazole is an organic compound with the formula $O_2NC_3H_2N_2H$) or amoxicillin (against gram-positive and gram-negative microorganisms). The most widely used technique was penicillin (an efficient penicillin) plus metronidazole [86]. Systemic antibiotic scores are difficult to assess since few research have compared outcomes to not using antibiotics.

In contrast to animal research, open debridement has been a regularly employed approach for treating peri-implant infections in human investigations [86]. Osteoplasty (surgery to correct the defective bone) and apical flap (transplanting the upper tip part of a cell, structure or organ to another area) have been used, and a healing effect on soft tissue has been observed. Behnke et al. Autogenous bone grafts (in the reconstruction (rearrangement) of the jawbone that is not suitable for the desired treatment due to cysts, premature tooth loss, trauma and similar reasons, the

transfer of bone taken from another part of the patient (e.g. jaw tip , retromolar area, hip, leg) to the area to be arranged) Some treatment cases with observation intervals of up to 3 years and significantly reduced probing depths with significant radiological bone filling have been reported [87]. Orthopedic devices or implants based on Mg and its alloys have already been tested and reported in Germany, China, and Korea for the correction of fractures or bone flaps [88].

Based on clinical study, the Mg-Y-Re-Zr screw has been approved by the notified bodies designated by the relevant authorities (the applicable basis for certain products before they are placed on the EU market) to successfully obtain a CE (Conformity) mark European) approved in 2013, allowing this new device to enter the medical device market for its intended use. This is an organization commissioned by a member state to assess its conformity to technical requirements. In 2015, Mg Y Re Zr screws were used to treat Madelung deformity in Ireland. Zhao DW et al. [89] used specially designed high-purity magnesium screws to fix vascularized bone flaps during surgeries on patients with stage II/III (ARCO) osteonecrosis of the femoral head (ONFH) in 2015 (Figure 2.10). Patients treated with magnesium screw fixation experienced improvements in bone flap displacement and Harris Hip Score (HHS) using radiographic imaging during the 12-month follow-up period. These improvements were both satisfactory and significantly better than the baseline results (n = 23 in the magnesium group). n = 25 for the control group. This was China's first clinical study and it made a big difference in how quickly pure magnesium-based screws for ONFH reconstructive surgery were registered as a product. In 2015 [90] the Chinese FDA (CFDA) recognized the mg screw's innovative design as a medical device.
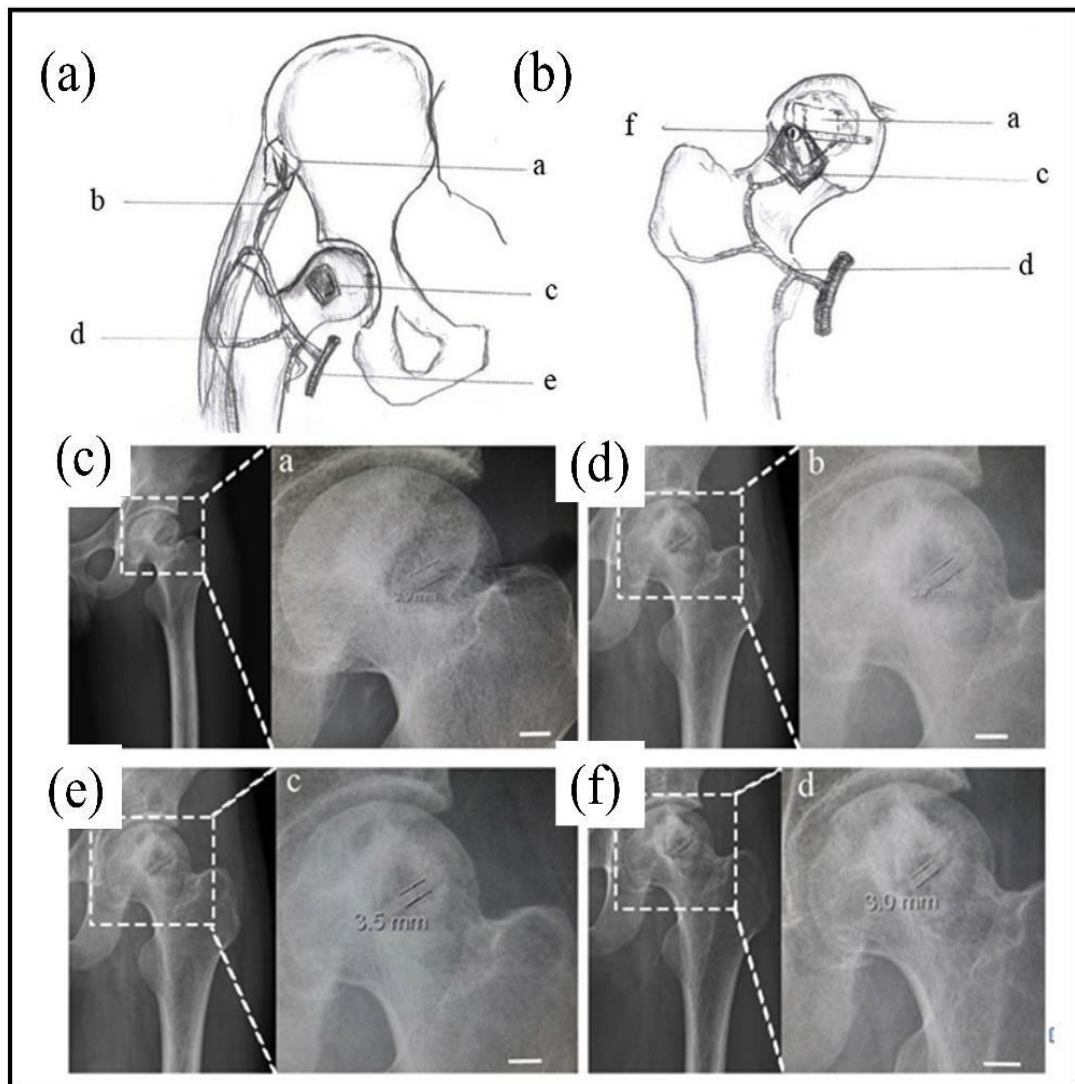
Figure 2.12. Fixation (a) and (b) Bone flap fixation with Mg screw and operation schematic (a: vascularized bone graft (left: origin of bone flap from ilia; right: implantation into the bone defect and after removal of necrotic bone); b: circumflexa femoris lat eralis artery; e: femoral artery; f: bone flap fixation with Mg screw placement). At 1, 3, 6, and 12 months following surgery, bone flap fixation using magnesium screws is described in (c)–(f) [89].

2.6. TYPES OF CORROSION OF MAGNESIUM AND ITS ALLOYS

2.6.1. Generalized Corrosion and Passivation

Magnesium has developed a protective gray oxide film that prevents further oxidation after being exposed to air. It is possible to heat magnesium to its melting

point in air without it burning. But when the powdered metal comes into contact with water or a moist environment, it heats up and reacts violently. An explosive mixture may arise from the evolution of hydrogen through its reactions. Magnesium and water in an aqueous solution separate via an electrochemical process. With an increase in oxygen concentration, it yields a crystalline film of magnesium hydroxide ($Mg(OH)_2$) and hydrogen gas at a rate that has increased noticeably. Therefore, for rapid corrosion, only basic hydrogen discharge points are needed [91]. In an aqueous solution, magnesium's primary corrosion reaction is most likely to be.

$$Mg(s) + 2H_2O(l) \longrightarrow Mg(OH)_2(s) + H_2(g).$$

Anodic and cathodic reactions can be used to explain this general reaction in the following ways:

Anodic reaction (magnesium dissolution):

- $Mg(s) \longrightarrow Mg_{2+} + 2e_-$ e/ou $Mg(s) + 2OH_- \longrightarrow Mg(OH)_2(s) + 2e_-$
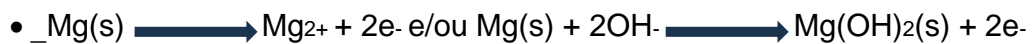
Cathodic reaction (hydrogen release reaction):

- $2H_+ + 2e_- \longrightarrow H_2(g).$

A subsequent reaction forming OH- ions may occur and/or:

- $2H_2O + 2e_- \longrightarrow H_2(g) + 2(OH_-).$

The anodic reaction's product for magnesium corrosion can include carbonates, hydroxides, sulfides, and/or sulfate compounds, depending on the medium. In an alternating layer of magnesium and hydroxide ions, the hydroxide film brucite has a hexagonal crystal structure that promotes basal cleavage.

There are visible ripples and cracks throughout the film, but it is unclear whether this is due to the release of hydrogen or the properties of the film. There is a compression film, as indicated by the $Mg(OH)_2$ pilling/Bedworth ratio of 1.77. The internal stresses of the film and the facilitated basal cleavage may be the cause of some of its cracks and ripples. Thus, the behavior of the base metal during corrosion is directly

influenced by the structure of the corrosion product. In weakly buffered and alkaline media where surface pH can rise, magnesium can form a surface film that protects the metal. Aggressive anions, including chlorides, sulfates and nitrates, destroy the passivity of magnesium. These films are influenced by corresponding elements, although the effects of these influences are not well understood [91].

Due to the production of $Mg(OH)_2$ during the corrosion reaction, magnesium may be protected at high pH values, as indicated by the Pourbaix (potential pH) diagram. Since magnesium H_2 and Mg_{2+} are formed when an electrode comes into contact with an aqueous solution, it is assumed that thermodynamic equilibrium cannot exist. Since the pH is less than 5 and the hydrogen overpotential is approximately 1 V, such an equilibrium is thus conceivable. The E versus chart takes into account the subsequent responses. In Figure 2.13, the pH value is displayed [92].

(1) $2H_+ + 2e_- \longrightarrow H_2(g)$

(2) $MgH_2 \longrightarrow Mg_{2+} + H_2 + 2e_-$

(3) $MgH_2 + 2OH_- \longrightarrow Mg(OH)_2 + H_2 + 2e_-$

(4) $Mg_{2+} + 2OH_- \longrightarrow Mg(OH)_2$

(5) $Mg_+ \longrightarrow Mg_{2+} + e_-$

(6) $Mg_+ + 2OH_- \longrightarrow Mg(OH)_2 + e_-$

$Mg_+ + 2H_2O \longrightarrow Mg(OH)_2 + 2H_2 + e_-$

(7) $MgH_2 \longrightarrow Mg_+ + H_2 + e_-$
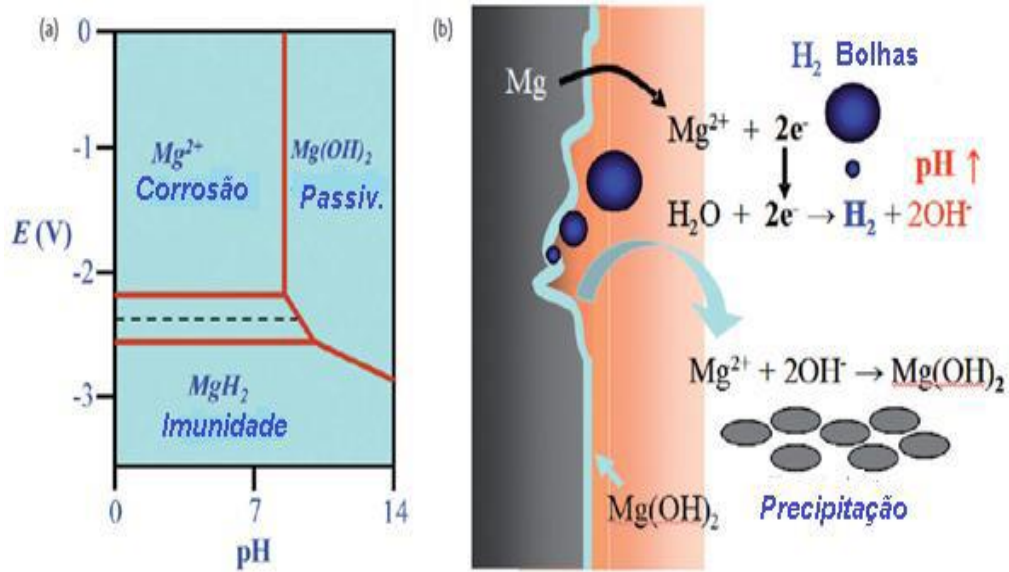
Figure 2.13. Corrosive characteristics of magnesium: (a) Equilibrium of the Mg-H2O system in the presence of H_2 at 25ºC; (b) Schematic representation of magnesium degradation, where Mg dissolves in Mg^{2+}, which reacts with water, generating hydrogen bubbles, creating hydroxyl groups and increasing the pH [92].

Since the magnesium film forms from $Mg(OH)_2$, it becomes polarized, and even though magnesium has a standard electrode potential of -2.37 V at 25 °C, in neutral or diluted chloride solutions, its potential is more negative than -1.5 V compared to the standard hydrogen electrode. In both industrial and rural settings, magnesium's oxide film offers substantial surface protection. Low-carbon steels and aluminum exhibit different rates of magnesium corrosio [92].

2.6.2. Galvanic Corrosion

Since most other metals are anodic to magnesium, galvanic microcells between magnesium and alloying elements or impurities form, which can cause galvanic corrosion, which is a serious issue. This situation was altered by adding alloys with a high level of purity[93]. ertain elements have little to no negative impact on the corrosion performance of binary magnesium alloys in saltwater. These elements include aluminum, manganese, sodium, silicon, tin, and lead. Other elements that have little to no effect on the corrosion performance of the alloy in saltwater include thorium, zirconium, beryllium, cerium, praseodymium, and yttrium. Adverse effects

on corrosion rate are observed for other elements like cadmium, zinc, calcium, and silver. On the other hand, the low solubility limits and cathodic active sites for corrosion of iron, nickel, copper, and cobalt result in extremely negative effects. As a result, it's critical to regulate the magnesium alloy's impurity level in order to stop galvanic corrosion and preserve the ability of a protective surface film to form. Still, there's no assurance that a high-purity alloy won't corrode[93].

2.6.3. Localized Corrosion

Due to a weak electrolyte and a low relative anode/cathode area ratio, local corrosion can result in pitting. Localized corrosion manifests as thread corrosion, pitting, and cracking. Pitting corrosion occurs when there is a weak spot in the oxide layer; Figure 2.14 illustrates this phenomenon.

Figure 2.14. Example of pitting on the surface of a metal [94].

Pitting corrosion is caused by a disruption of the oxide film's passivity in defects next to intermetallic particles. Next, an electrolysis cell of the type AlMnFe, $Mg_{17}Al_{12}$, or Mg_2Cu is created, with the intermetallic particles serving as the cathode and the matrix surrounding Mg as the cathode. The overall corrosion rate in the intermetallic AlMnFe appears to be determined by the Fe/Mn ratio, the predominant cathodic reaction, and hydrogen evolution. More noble intermetallic compounds are left in the

relief along the grain boundaries when the alpha matrix, which is primarily composed of magnesium, corrodes preferentially [91]. Studies on magnesium pitting and its alloys have been conducted by linking the alloys' fast cooling to the pitting behavior. Two metrics that indicate the resistance to pitting corrosion were measured in these studies: a) the passive current density, or ip, which represents the passive film's protective quality; and b) the fracture or pitting potential, or Ep, which represents the passive film's resistance to fracture against pitting. The film is more protective of the metal surface the higher the positive E value [91].

2.6.4. Grain Boundary Corrosion

In intergranular corrosion, the potential difference between the grain boundaries is greater than that within the grain due to the amorphous structure of the grain boundaries. Since the interior of the grain has a nobler structure, it is preserved while the grain boundary corrodes. Grain boundaries experience intergranular corrosion as a result of the secondary phase precipitating there. There are always regions where segregations and precipitations take place along grain boundaries. Intergranular corrosion is highly sensitive to alloys or compounds that contain intermetallic phases because of this. The existence of intergranular corrosion in magnesium alloys is disputed. Maker and others. stated that since the phases at the grain boundaries are cathodic to the grains, real intergranular corrosion cannot occur in magnesium alloys [95] intergranular corrosion, however, can happen in magnesium alloys, according to a different study [96] The vicinity of the grain boundary is typically where corrosion concentrates. Zeng in collaboration. Intergranular corrosion was found in artificially aged AZ80 Mg alloy after it was submerged in a 3 percent NaCl solution for one hour, according to [97] It was mentioned in the study carried out by. The average concentration of Al in the matrix drops with age. The aged AZ80 alloy has a less protective oxide film on its surface due to the decreased concentration of aluminum in its matrix. Consequently, the corrosion attack that happens in aged AZ80 alloy readily starts in the vicinity of the matrix's β phase. According to reports, the rate of corrosion could rise when the Al content in the α matrix falls.

2.6.5. Corrosion Fatigue

Corrosive fatigue is a type of damage that manifests itself in the form of cracks caused by corrosive environment mobility and periodically occurring loads on the material. Most parts are exposed to periodic loads in long-term active environments. Roughness, surface defects, residual compressive stresses, and environmental conditions are also among these factors. Most fatigue failures occur related to the fatigue life of materials, and the lifespan of materials varies depending on their environment.

Reductions in the fatigue strength or fatigue life of magnesium alloys have been observed in numerous experiments, even when the water used is tap or distilled [98]. In a 3 .5% NaCl solution, for instance, the fatigue corrosion resistance of AZ91E-T6 Mg alloys dropped dramatically when compared to air [99]. The fatigue life of cast magnesium alloys is much longer than that of extruded magnesium alloys in a corrosive environment [100]. Eliezer and Co. In 0.1 N $Na_2B_4O_7$ buffer solution and NaCl-based solutions,[101] examined the corrosive fatigue behavior of cast and extruded Mg-Al-Mn, Mg Al-Zn, and Mg-Zn-Zr alloys. As compared to solutions containing NaCl, the results demonstrated that all alloys had longer fatigue lives in air.

2.7. CORROSION OF MG ALLOYS (MgAlZn)

Magnesium alloys have a long history of corrosion, especially in salty conditions. This has been the case for several decades. The 1980s saw the introduction of highly pure alloys, which drastically altered the behavior of the alloys. The magnesium-aluminum-zinc system is still the most commonly used. The first commercially available magnesium alloys were those containing Al and Zn as alloying elements. Due to their good combination of formability, ductility, and corrosion resistance, AZ31 alloys—which contain 3% Al, 1% Zn, and 0.3 percent Mn—are frequently used.[4]. Fernandes [102] performed heat treatments on the AZ31 alloy, which was first solubilized at 440 °C for 24 hours and then cooled in water. After solubilization, three samples were aged 4, 6, and 12 h, respectively, and then cooled in water. The

aging time was deliberately varied to obtain different microstructures so that these changes could later be correlated with differences in electrochemical corrosion measurements. The samples exposed to longer aging times showed increased average grain size and decreased in twinning. The analysis of the corrosion indicators in 3.5% NaCl solution (m/m), such as idle potential, corrosion potential, pitting potential, current, density, and corrosion rate, showed that the larger the grain size corrosion resistance of the alloy, the shorter the aging time. According to studies, as grain size increases, so does the rate at which the AZ31 alloy corrodes in a sodium chloride solution. The larger crystallographic defects found at the grain boundaries of polycrystals, such as magnesium alloys, act as a barrier to corrosion and can inhibit corrosion propagation, which could account for the AZ31 alloy's increased corrosion resistance despite its finer grain structure. On the other hand, this explanation runs counter to the findings that corrosion cannot be stopped by grain boundaries and that grain boundaries are chemically more active than the grain center. Through the reduction of compressive stress that would otherwise lead to oxide film cracks, increasing the density of the grain boundary can make up for the incompatibility of the oxide-base metal interface. Consequently, an increase in corrosion resistance may be explained by a more stable oxide film on the surface of the fine-grained magnesium alloy. Nevertheless, there is a gap with enough data to back up this assessment. To validate this claim, more investigation is therefore required [8, 9, 103].

Liu et al.[104] demonstrated that compared to grains with other orientations, pure magnesium grains with the (0001) orientation dissolved more slowly in 0.1 N HCl. For the AZ31 alloy, this corrosion dependence on grain orientation phenomenon was also noted. But Liu et al. presented corrosion results in 2008 without providing electrochemical data to back up their claims. However, even though Song et al..[105] examined the electrochemical behavior of various orientations on the AZ31 alloy surface in a diluted sodium chloride solution; however, the findings do not reflect the electrochemical behavior per se, but rather the average performance of numerous fine grains. or the rusting of a straightforward grain that has a clear crystal orientation. Therefore, in order to gain a deeper and more fundamental understanding

of the corrosion of magnesium and its polycrystalline alloys, electrochemical studies of individual grains are required.

2.8. HEAT TREATMENT OF MG ALLOYS

Heat treatments can be applied to magnesium alloys to further improve their mechanical properties. The T5 and T6 heat treatment programs are two heat treatments that can be used on magnesium alloys whose designations are the same as those for aluminum alloys. The sample is artificially aged and cooled to a high temperature during the T5 process. The process of subjecting a material to temperatures that are moderately high in order to hasten microstructure changes over long periods of time is known as artificial aging. As a result, the microstructure can cause the precipitation of fine phases and reaches a stationary state faster. The sample is solution-treated, quenched, and artificially aged during the T6 process. A material is subjected to a higher temperature during the solution annealing process, which causes microstructure components to change into a solid solution rather than liquid phases forming. After that, the sample is quenched to capture the solid solution that results. Both procedures are frequently applied to magnesium and aluminum alloys in order to modify their properties [106].

Mg alloys produced by casting are generally aged by heating to a temperature range of approximately 380-420 °C. Magnesium is a combustible element, and when heated to a temperature above 400°C in the absence of a protective atmosphere, Mg begins to burn and creates gaps in the microstructure. The heat treatment environment is maintained in an air atmosphere with about 0.7% to 1.0% SO_2 to prevent material oxidation. T6 heat treatment that is, artificially aged cast materials after heat treatment, provides better results than the as-cast state of the material with the heat treatment applied and increases the strength of the alloys. By undergoing artificial aging heat treatment (T6) at temperatures between 175 and 200 °C, magnesium alloys are generally predicted to obtain a stronger composition. This causes the AZE911-T6 alloy's lifetime at 250 °C to drop to a value that is lower than its lifetime at room temperature. Consequently, at temperatures above a certain point, the LCF lifetime decreases and then increases to that point [107].

2.9. Mg SHEET PRODUCTION WITH TRADITIONAL MATERIAL METHOD

Hot rolling is a process that transforms AZ31 magnesium alloy into thin sheets or plates with improved mechanical properties and surface quality. The alloy is heated to a temperature above its recrystallization point, which is about 300°C for AZ31, and then passed through rollers that reduce its thickness and shape it into the desired form[108]. Because the coarse grains are broken up and a fine-grained microstructure with a uniform distribution of alloying elements is created, the hot rolling process improves the ductility, strength, and corrosion resistance of the AZ31 alloy [109]. Hot rolling also reduces the residual stresses and improves the dimensional accuracy of the alloy. The distribution of strain, temperature, and strain rate in rolled metal significantly influences metallurgical events like recrystallization and breakdown. Understanding microparameters' influence on phase transformations through hot rolling is crucial, leading to numerous studies to predict rolling process parameters and estimate interconnections between microparameters and metallurgical phase transformations [110].

The steps involved in making magnesium sheet traditionally are as follows: i) direct cooling (DC) casting process up to molds (e.g. g. 0 - 3 m - 1 m - 2 m); ii) blending the plates for multiple hours (e.g. g. iii) Hot rolling (480°C ~ 300°C) in multiple passes up to 5–6 mm in a reverse hot rolling mill; iv) Annealing the sheet before each final pass (usually at 340°C) results in multiple passes at a reduction of 5–20 percent for the final surface rolling. The last step in hot rolling takes a lot of time, reduces output, and has significant running expenses [111].

It is crucial to consider the amount of deformation in relation to the temperature every pass. The resultant microstructure is also affected by other characteristics like as strain rate and rolling rate. In the case of Gou F. et al. The AZ31 Mg alloy was rolled in a single pass at three distinct speeds: 3–12.0 m/min with strain rates of 20%, 40%, and 70%. It has been shown that minor deformations result in twinning, whereas larger deformations are mostly associated with recrystallization.

Recrystallization is known to boost ductility, while twin content has the opposite effect, reducing ductility while increasing yield strength. [112]. Also, the same author said in a different investigation that recrystallization was confined in slip bands at low rolling speeds, but broadened and uniformly distributed at high rolling speeds. Furthermore, dynamic recrystallization was reported by the same author to prevent edge cracks during rolling [113].
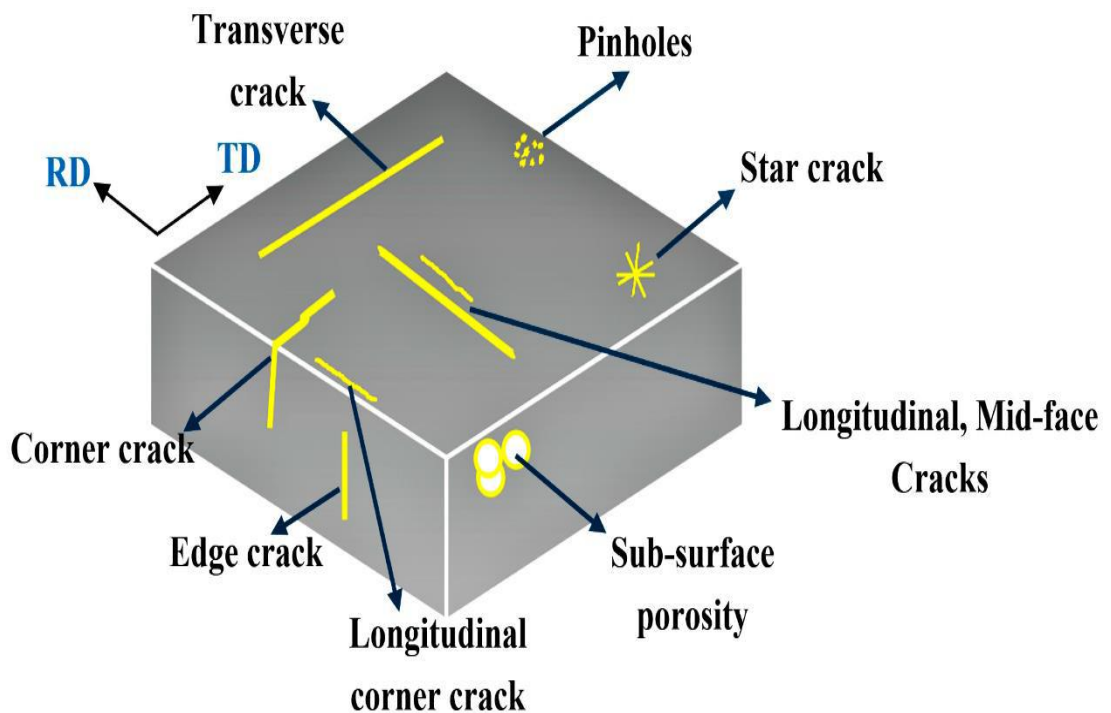
Figure 2.15. Typical surface defects in rolled products (RD: rolling direction, TD: transverse direction) [114].

Ding Y et al. [115] used rolling mill speeds ranging from 18 m/min to 102 m/min for magnesium alloy AZ31B. During deformation, twinning and ongoing dynamic recrystallization were noted. The twin density decreased as the material rolled in four passes rolled faster, but grain growth continued because the abrupt temperature change was avoided. The material was rolled twice, increasing the grain size excessively, but recrystallization decreased.

PART 3

METHODOLOGY AND EXPERIMENT

3.1. INTRODUCTION

In this section, the experimental procedures followed throughout the study are described in detail. The procedures include the collection and preparation of the samples and the hot rolling in different directions. The devices and techniques used to perform these tasks are also explained, along with their specifications and advantages. The rationale and significance of each step are also discussed to provide a clear and comprehensive understanding of the experimental methodology used in this study.

3.2. MATERIALS AND METHODOLOGY

AZ31 and a modified AZ31-Mg alloy were the main materials used in this study. Pure magnesium, pure aluminum and pure zinc were available in Turkey, but China was the main source of alloys. The manufacturing process employed low-pressure continuous casting using a specially designed die, as shown in Figure 3.1. Pure ingots of magnesium (99.9 percent), aluminum (99.9 percent) and zinc (99.9 percent) were melted at 750 °C with argon gas in the graphite pan. The melt was mixed with master alloys based on 10% Mg-Mn, 25% Mg-Ca and 25% Mg-Ce and heated to 750 °C for 15 minutes. The temperature and pressure of the molten metal were recorded at 350 °C and 2 to 3 atmospheres, respectively, after the ingot was finally discharged into a crucible filled with tin only. The molds were then heated to a very high temperature to inject the stainless steel metal into them. To prevent microsegregation, homogenization was carried out for 24 hours at 350 °C.

Figure 3.1. Mold casting furnace with low pressure[116].
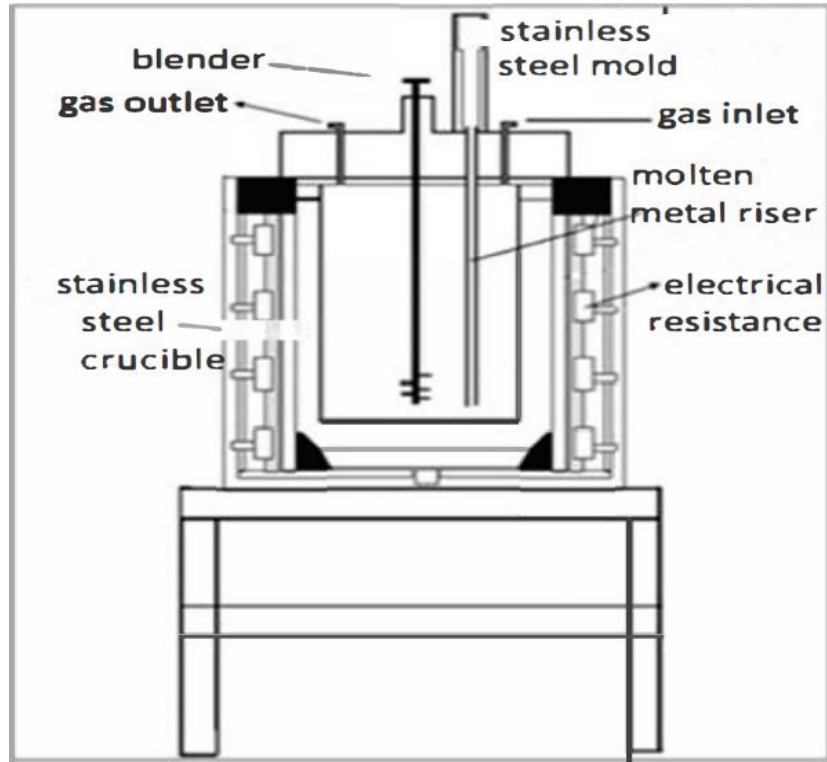
The experimental program of the current study is shown in Figure 3.2. Table 3.1 shows the allowable element percentages for the prepared alloys.

Table 3.1. Alloying elements used in the study.

Materials	Al	Mn	Zn	Ca	Ce	Mg
AZ31	2.94	0.13	0.98	-	-	Bal.
AZ31-1.0Ca-0.5Ce	2.99	0.24	0.90	0.96	0.43	Bal.

```
┌─────────────────────────────────────────────────────┐
│                    Pieces of                         │
│      Mg ,Al, Zn  with  and without Ca and Ce         │
└─────────────────────────────────────────────────────┘
                          ↓
┌─────────────────────────────────────────────────────┐
│   Ingredients are melted for 15 minutes at 750 $^{o}$C.  │
└─────────────────────────────────────────────────────┘
                          ↓
┌─────────────────────────────────────────────────────┐
│              Injected into steel mold                │
└─────────────────────────────────────────────────────┘
                          ↓
┌─────────────────────────────────────────────────────┐
│         homogenization at 350 $^{o}$C for 24 h          │
└─────────────────────────────────────────────────────┘
                          ↓
┌─────────────────────────────────────────────────────┐
│    Hot rolling at 400 $^{o}$C in different direction    │
└─────────────────────────────────────────────────────┘
                          ↓
┌─────────────────────────────────────────────────────┐
│         Characterization the prepared alloy          │
└─────────────────────────────────────────────────────┘
```

| Corrosion | Wet wear | Microstructure | XRD |

| Immersion tests |
| Potentiodynamic |
| EIS |

| Optical microscope |
| SEM & EDX |
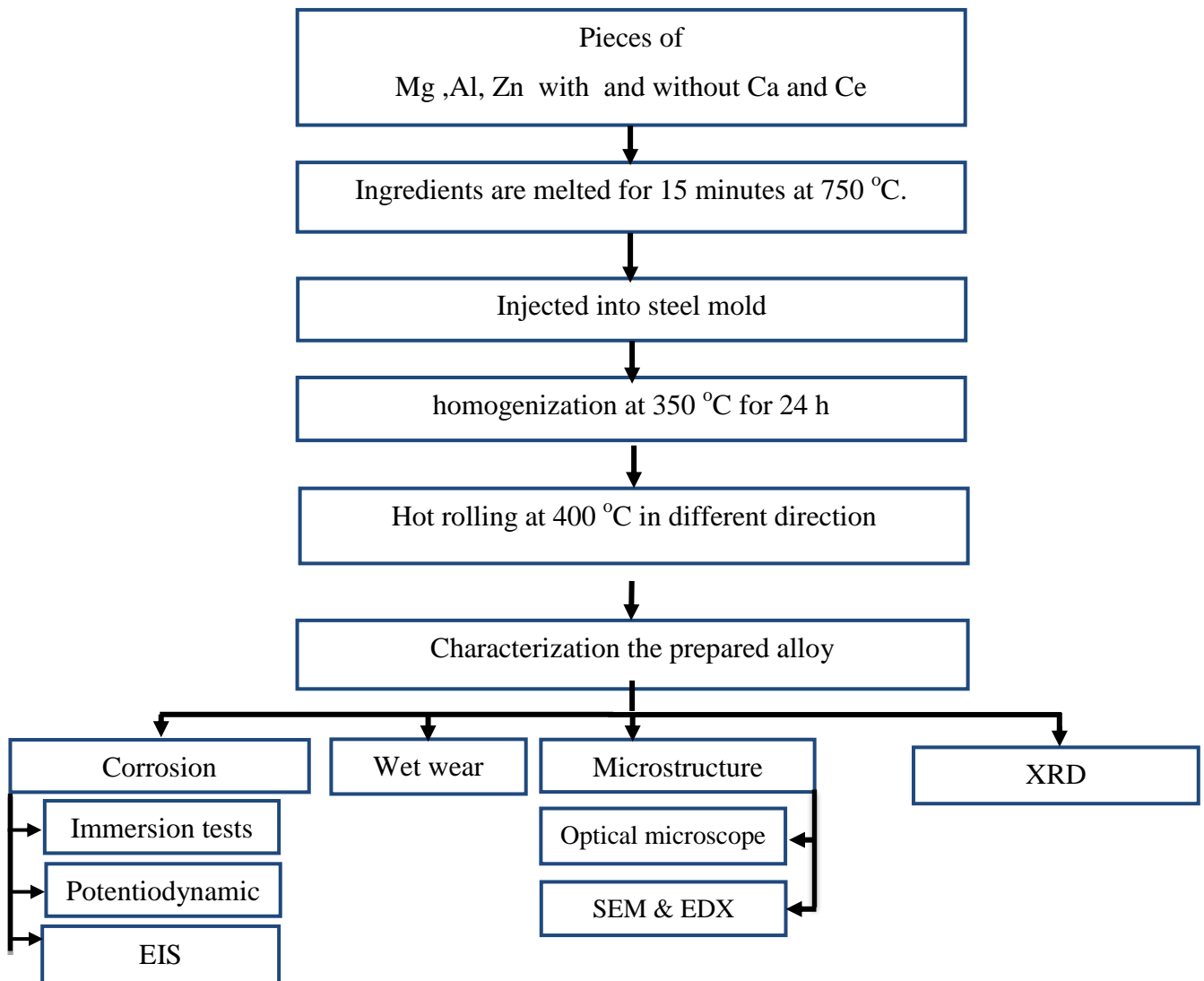
Figure 3.2. Protocol for the current study.

3.3. HOT ROLLING

During the hot rolling process (400 °C), a total of six passes were applied to 17 x 30 x 30 mm sheets, obtaining 10 mm thick sheets. Each pass has the same strain rate of 8%. After the homogenization process, the ingot is put into the hot rolling apparatus to be hot rolled according to the details listed in Table 3.2. The standards according to which hot rolling was carried out are listed there. The cross section of the ingot is

also narrowed by 8% and the total number of passes (8) for each pass. The strain rate values were determined using the equation [117]:

$$\dot\varepsilon = \frac{H-h}{H}\frac{v}{\sqrt{R(H-h)}}$$

Table 3.2. Rolling parameters.

Rolling temperature (°C)	Deformation (%)	Rolling speed (m/min)	Total number of passes	Rolling radius (mm)
400	8	9.996	6	55

Figure 3.3) and Table 3.3 show that the rolled plate materials were cut perpendicularly (90°, TD), transversely (45°) and parallel (0°, RD) to the rolling direction in order to achieve the direction-dependent high temperature mechanical properties of the alloys.
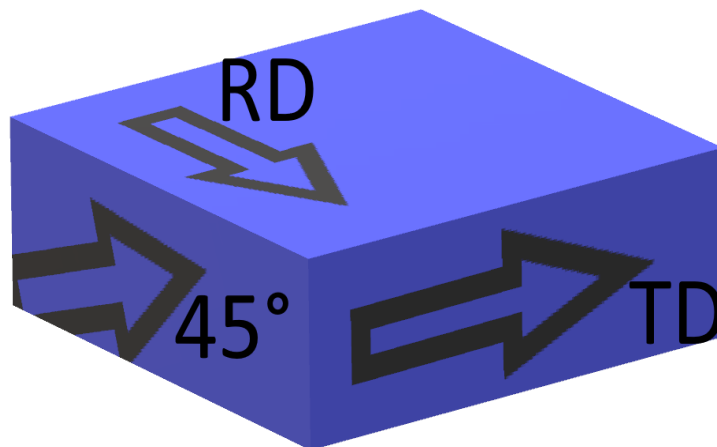

Figure 3.3. The extracted samples directions from hot rolled specimens.

Table 3.3. Rolling conditions.

Alloys	perpendicular 90° to RD	Parallel 0° to RD	45° to RD cross (45°) to the rolling direction
AZ31	A1	A2	A3
AZ31-1.0Ca-0.5Ce	B1	B2	B3

3.4. PREPARATION OF SAMPLES TO TEST

3.4.1. Material Cutting

The samples were cut using an electric saw and water to ensure that the internal phase of the samples was not changed, as shown in Figure 3.4, according to different dimensions suitable for the type of tests used. For potentiodynamic corrosion and electrochemical impedance spectroscopy tests, the samples ' sizes were cut to 1×0.9 cm, and the samples ' sizes for the immersion corrosion and wear tests were cut to 1×1 cm.

Figure 3.4. Cutting device.

3.4.2. Cold Bakelite

The samples were mounted by placing them in a gelatin mold and pouring resin on them. This is prepared using the resin with a hardener and a color of choice. After two hours, as Figure 3.5 illustrates, the resin had fully solidified. Upon drying, the samples were removed from the mold.

Figure 3.5. The cold bakelite mold for the prepared samples.

3.4.3. Grinding and Polishing

The samples were polished with a 1 μm diamond suspension and processed with silicon carbide paper (SIC) on a grinding machine, as shown in Figure 3.6.

Figure 3.6. The grinding machine.

3.5. MICROSTRUCTURE CHARACTERIZATIONS

3.5.1. Preparation of Samples

For the samples, Picral's solution consisting of 4.2 g picric acid, 10 ml acetic acid, 10 ml distilled water and 70 ml alcohol was prepared [118].
Before the etching process, the samples were sanded with 600, 800, 1000, 1200, and 2500 silicon carbide paper, then polished using 1 mμ alumina solution.

3.5.2. Optical Microscope(OM) and Scan Electron Microscope(SEM+EDX)

Images of microstructures were acquired using a Nikon Epiphot microscope at the Materials Laboratory of Karabük University's Faculty of Engineering. Microstructural pictures were collected at 200x and 500x magnifications for each alloy in experimental experiments. Figure 3.7 depicts the optical microscope used in the studies. An optical microscope was used to examine the size and form distribution of grains, grain borders, and secondary phases.

Figure 3.7. Optical microscope.

The KBÜ Iron and Steel Institute's SEM lab conducted EDX and SEM investigations of sample microstructure characterisation using the Carl Zeiss Ultra Plus Gemini Fesem equipment. Figure 3.8 depicts the experiment's scanning electron microscope.

Figure 3.8. Scanning electron microscope Carl Zeiss ultra plus gemini FESEM.

3.6. X-RAY FLUORESCENCE (XRF) AND X-RAY DIFFRACTION (XRD) ANALYZES

Rigaku ZSX Primus II and Ultima IV XRF and XRD equipment identified phased and intermediate compounds and alloying element percentages for produced alloys. XRD graphs were taken on a copper target XRD device. XRD profiles of all samples after casting were obtained at a scanning angle range of 90° and a scanning speed of 3°/minute.

3.7. CORROSION TESTS

3.7.1. Characterization of Corrosion Properties

Characterization of corrosion properties of casting and hot rolled samples at pH 7.4 and using Hank solution (HBSS and HBSS+) as shown in table 3.4. The electrochemical potentiodynamic polarization tests and continuous immersion in

Hank's liquid at 37 °C were used to conduct the experiment. The prepared samples were subjected to electrochemical impedance measurements (EIS).

In order to conduct immersion and potentiodynamic polarization corrosion testing, the samples' surfaces were sanded using sandpaper with a maximum mesh count of 600, 800, 1000, 1200, and 2500. The sample surfaces were prepared for electrochemical impedance measurements (EIS) by cleaning them of debris and sanding them with sandpaper with 600, 800, 1000, and 1200 mesh. Certain factors that could impact the rate of corrosion have been removed.

Table 3.4. Hank's solution compositions [119].

Solution	Compositions (mg.dm^{-3})							
	NaCl	KCl	KH_2PO_4	Glucose	Na_2HPO_4	$MgSo_4$	$CaCl_2$	Na_2Co_3
HBSS	8000	400	60	1000	48	-	-	350
HBSS$^+$	8000	400	60	1000	48	98	140	350

3.7.2. Immersion Corrosion Test

Immersion corrosion tests were performed in Hanks liquid HBSS and HBSS+ at 37°C as shown in Figure 3.9 and with a chemical composition as shown in Table 3.3. To carry out immersion tests, 1*1 cm samples were cut from hot-rolled and cast alloys. Before testing, the samples were subjected to a 5-minute ultrasonic bath cleaning with ethyl alcohol after being sanded with 120-1200 grit sandpaper. A sensitive balance (Precisa XB220A) was used to weigh each sample (Ms). The surface area of each sample was measured before testing and it was immersed in the corrosive environment for 8, 16, 24, 48 and 72 hours. There were five repetitions of the immersion tests. The corrosion byproducts of the samples were cleaned after each test by immersing them in an aqueous chromic acid solution in an ultrasonic cleaner for five minutes. It was then cleaned with deionized water and immersed in an ultrasonic bath containing ethyl alcohol for three minutes. After final drying in warm air, its mass (Mf) was measured. The corrosion mass loss is defined as the difference (Ms) between the initial measurement and the final measurement (Mf).

Figure 3.9. Immersion test of AZ31 alloys.

3.7.3. Potentiodynamic Polarization Test

The samples of AZ31 alloy and AZ31 modified alloy were prepared, which were hot rolled in three different directions with a surface area of 1*0.9 cm. Subsequently, Copper wires were wrapped tightly around the samples to ensure good conductivities. Then, they were mounted by placing them in a gelatin mold and pouring epoxy resin on them Subsequently, the sample surface was centered by making circular cuts in adhesive tape with a diameter of 0.16 cm2 at its midpoint. This ensured that corrosion tests were conducted in identical areas for every sample. Figure 3.10 shows Gamry model PC4/300 mA potentiostat/galvanostat with computer-controlled DC105 corrosion study tested Hank's liquid (HBSS and HBSS+) at 37 °C for potentiodynamic polarization. The sample surface was the working electrode, the graphite rod was the counter electrode, and the saturated calomel electrode (SCE) was the reference electrode in this standard three-electrode cell. Scan from 0 to 25 V (volts) + Eoc to create polarization curves. At 1 mV scan rate, Eoc. The results of three potentiodynamic polarization tests of each parameter were averaged.
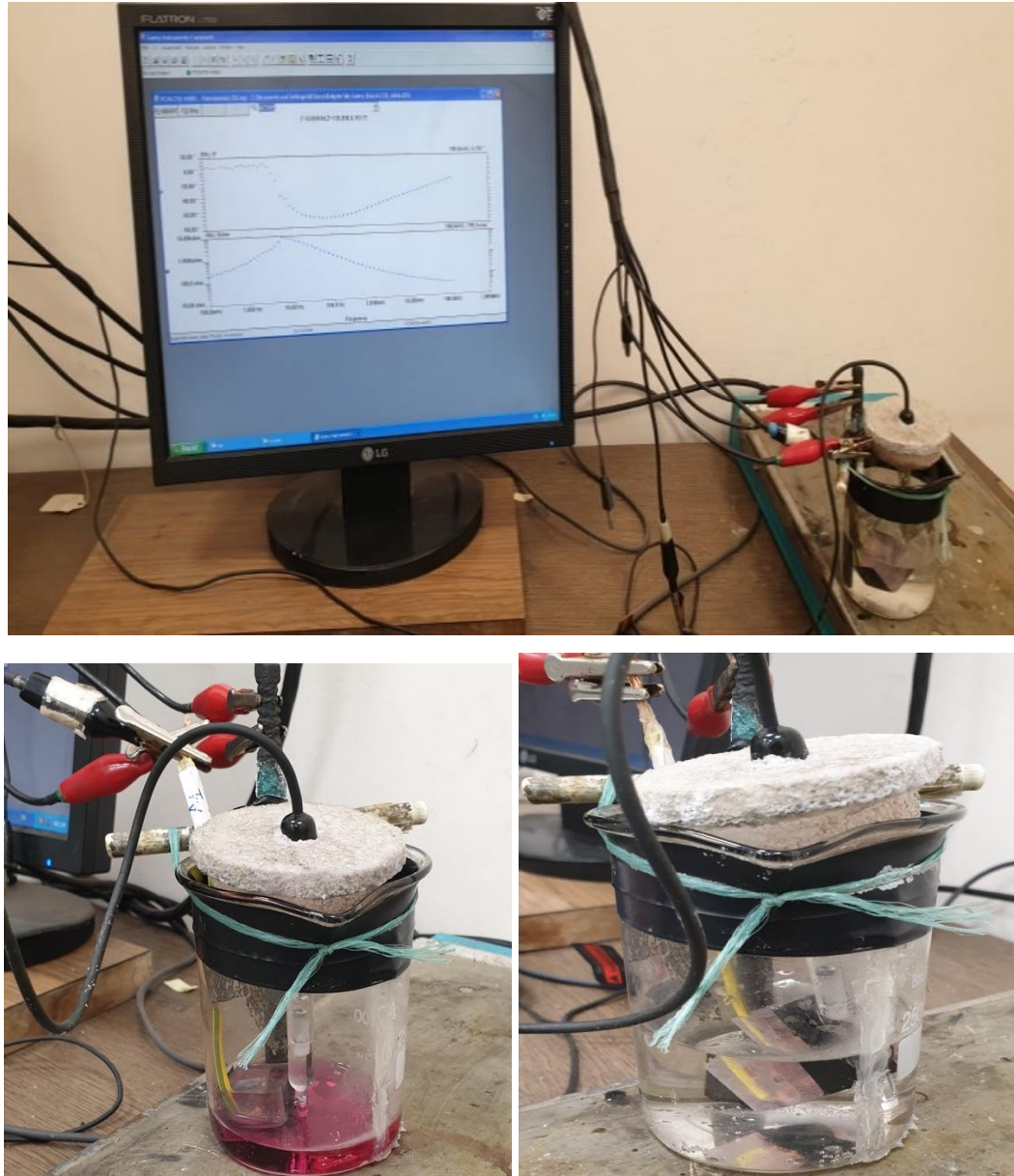
Figure 3.10. Potentiodynamic device used in the study.

3.7.4. Electrochemical Impedance Spectroscopy (EIS)

Electrochemical impedance spectroscopy tests were performed on hot-rolled specimens in three different directions. The surfaces of the specimens prepared for the electrochemical impedance spectroscopy test were cleaned with sandpaper No. 1000, 1200, and 2500 after the potentiodynamic polarization test was completed, Then, the sample surface was centered by making circular cuts in adhesive tape with a diameter of 0.16 cm2 at its midpoint. Using a Gamry model PC4/300 mA

potentiostat/galvanostat with computer-controlled DC105 corrosion analysis, electrochemical impedance spectroscopy tests were carried out in two types of Hank's solution at 37 °C for one hour. In the frequency range of 105 Hz to 10 2 Hz, EIS experiments were conducted at open-circuit potential with an AC amplitude of 10 mV. Nyquist plots were made at the conclusion of the test.

3.7.5. Corrosive Wear Test

Hot rolled sample wear tests were conducted using Hank's solution on the wear test device (back and forth) schematically depicted in Figure 3.11. The measurement was conducted under constant load, constant speed, and constant distance in Hank fluid, which is composed of the following conditions. The samples' surfaces were cleaned with pure water and alcohol and sanded to 1200 grit prior to the abrasion test. They were also cut to fit the sample bed in the apparatus. At a sliding speed of 0 points1 m/s and a total sliding distance of 400 meters, wear tests were conducted with loads of 2 and 4 N. The tribometer arm's load cell was used to measure the friction force during wear, and the results were instantly entered into the computer. The material for the penetrating tip was a high-hardness steel ball of AISI 52100 grade.
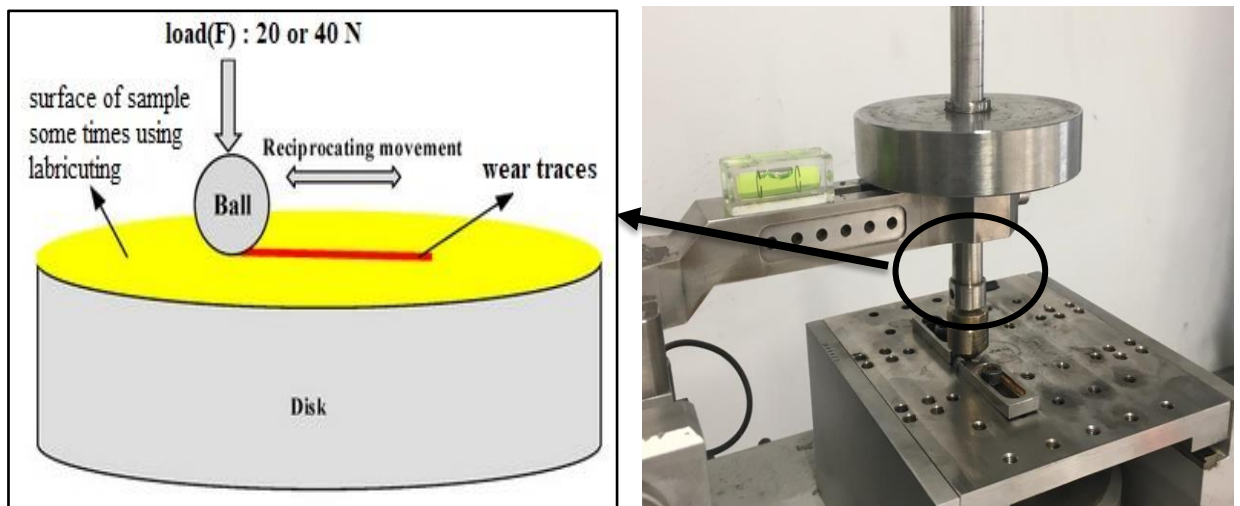

Figure 3.11. Schematic representation of the wear test.

The material is weighed on a sensitive balance (0.0001) g before testing. After sliding 0.5,1,1,5,2,2.5 mm, the test specimen is weighted and volume loss calculated using the equation. [120].

$$\text{volume loss} = \frac{\text{weight loss (g)}}{\rho \left(\frac{g}{cm^3}\right)}$$

Where:

Weight loss (g)= quantity loss

ρ (g/cm³) = theoretical density of the element formed for the specimen calculated from the following equation [120]:

$$\rho_{tB} = \sum_{i=1}^{n} Wt_1 * \rho_1 + Wt_2 * \rho_2 + \cdots\cdots + Wt_n * \rho_n$$

Wear rate calculated from the following equation [121]:

$$W_a = \frac{w_{loss}}{\rho * P * S}$$

Where:

Wa is the $wear$ $rate, mm3/N.m$

w_loss is the weight loss, g;

ρ is the $density, g/cm3;$

P is the $load, N$

S is the $sliding$ $distance, m.$

PART 4

RESULT AND DISCUSSION

4.1. INTRODUCTION

This section will characterize manufactured AZ31 alloys with and without varying Ca and Ce concentrations using XRD, optical microscopy, and SEM/EDS analysis. To prove these alloys' biological appropriateness, immersion tests, electrochemical impedance spectroscopy (EIS), potentiodynamic, and corrosive wear examined experimental samples' electrochemical behavior.
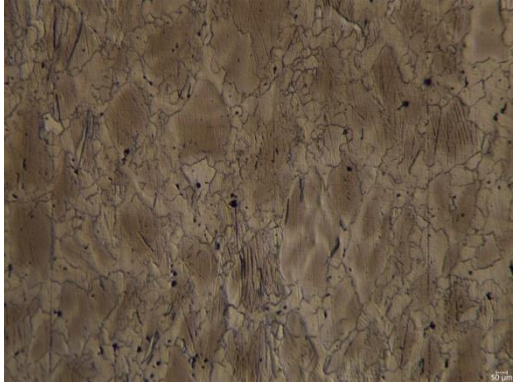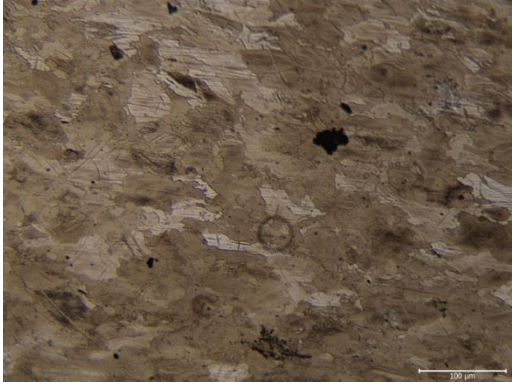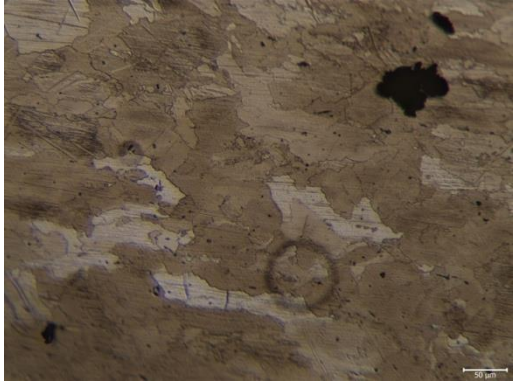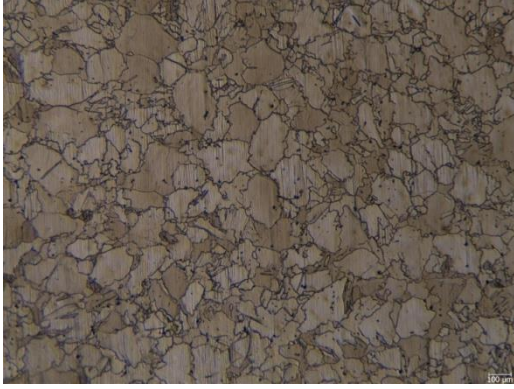
4.2. MICROSTRUCTURE CHARACTERIZATIONS

4.2.1. Analysis of Optical Microstructure

LOM images of prepared alloys shown in Figure 4.1. The bulk of grains in each sample were rolled. However, rolling direction affects average grain size [122]. The α-Mg phase is represented by the bright areas in the microstructure images of the AZ31 alloy as-cast (Figure 4.1 a), while the β-Mg_{17}-Al_{12} phase is represented by the dark-colored areas.

It can be observed that the structure consists of coarse grains. After adding Ce and Ca to the magnesium alloy AZ31, comparing the A1-A3 samples, the dispersed and dense presence of the intermetallic phase, which is presumed to be β-Mg_{17}-Al_{12}, is observed at the grain boundaries. Observing the post-homogenization microstructure of samples B1–B3, it could be seen that the phase thought to be β-Mg_{17}-Al_{12} was largely dissolved. Twinning is observed, a form of deformation that often occurs in metals such as Ce, where the number of slip systems is small, and sliding is difficult.

Figure 4.1 (B1-B3) shows that after rolling with the addition of Ce, the grains become thinner along the rolling direction.

Table 4.1. Optical microstructure of the prepared samples.

	100 μm	50 μm
A1		
A2		
A3		

B1		
B2		
B3		
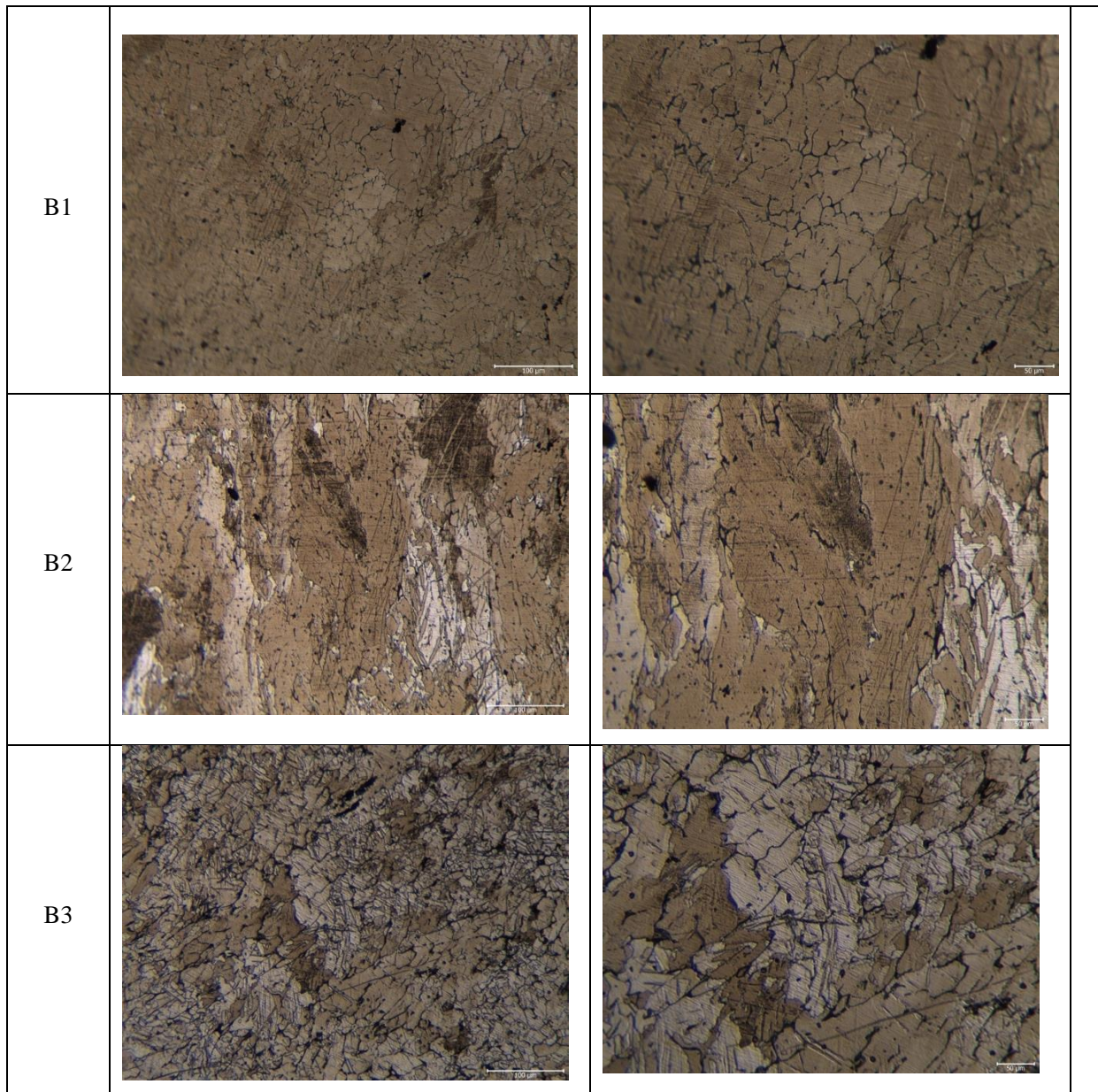
Because of the weakened base texture of alloy AZ31, the addition of Ca may result in high formability [123]. Song et al.[124] the tensile characteristics and microstructure of extruded AZ31 alloys with different weight percentages of Ca (0.5 and 1 wt. percent) were looked at. Findings indicated that the addition of Ca resulted in the formation of Al-Mn and Al_2Ca phases, a finer microstructure, and a weaker basal texture. However, the alloys' comprehensive mechanical properties improved due to grain refinement, second phase strengthening, and texture strengthening. This suggests Ca addition could enhance Mg alloy properties through dispersion strengthening. Masoudpanah et al. [125] adding 2% wt. AZ31's refined grain size and percentage Ca gave rise to increased tensile ductility. As such, it makes financial

56

sense to add Ca to AZ31 alloys in order to improve their microstructure and texture. The dynamic recrystallization and resulting inhibition of the corresponding grain growth occur when Ca is added to the magnesium alloy [116]. Consequently, the pinning effect of the finely dispersed precipitates that are formed in extruded material leads to high-density dislocations and reinforcement of the base texture. It has been demonstrated that adding Ca to wt causes the α-Mg grain size to gradually decrease. percent as a result of the Ca atoms' enrichment at the solid-liquid interface during solidification. The destruction of binary intermetallic Mg-Zn compounds at grain boundaries and the reversible concentration of the ternary Mg-Zn-Ca phase at grain corners are dependent on the increase in the Ca content of the alloy. [126]. According to Quan Li, the addition of Ce element can refine grain and purify the α-Mg matrix.[127], In contrast to AZ31 magnesium alloy, AZ31-xCe magnesium alloy exhibits a higher discharge activity because Ce is added to purify the magnesium alloy, and the Al4Ce phase helps encourage the Mg matrix to dissolve uniformly. pictures of the optical microstructure of the AZ31 alloy after it was hot-rolled in various directions and added Ca and Ce According to Table 4.1, twinning is seen in certain coarse grains of the alloys to which Ca and Ce are added, and crystal boundaries form in the majority of samples. Grain size is large because of the delayed cooling process following heat treatments. The microstructures of AZ31 alloy sheets rolled in different directions were significantly different. The sheet rolled perpendicular to RD (90°) had the finest and most equiaxed grains, the most random orientation distribution, and the weakest basal texture. The sheet rolled parallel to RD (0°) had intermediate grain size and shape, orientation distribution, and basal texture. The sheet rolled at 45° to RD (cross) had the coarsest and most elongated grains, the most aligned orientation distribution, and the strongest basal texture. These differences were attributed to the different strain paths, strain rates, basal plane rotation, and twins' formation during rolling. The sheet rolled perpendicular to RD (90°) was expected to have the highest ductility and formability, while the sheet rolled at 45° to RD (cross) was expected to have the lowest ductility and formability.

4.2.2. SEM analysis of Alloys

After an immersion test was carried out for 72 hours in HBSS modified with Mg^{2+} and Ca^{2+} ions and HBSS modified without Mg^{2+} and Ca^{2+} ions, respectively, Figures 4.1 and 4.2 shown images for the SEM of the surface of AZ31 and AZ31-1Ca-0.5Ce alloys. Figures 4.1 and 4.2 show that the pitting corrosion rate is high in samples A1 to A3, while the corrosion rate decreases with the addition of Ca and Ce in samples B1 to B3. Localized corrosion may occur in freely corroding circumstances, as a big hole progressively formed many hydrogen bubbles. Figure shows significant corrosion in samples A1-A3, which matches [128].

The mechanical qualities and corrosion resistance of magnesium alloys have been enhanced by calcium (Ca), which has recently come to light as a possible candidate. Keon et al. Ca's impact on the corrosion behavior of magnesium-5Al alloy was assessed in [128] which revealed a notable enhancement in resistance to pitting and polarization. The refined Mg_2Ca and Al_2Ca precipitate, as well as an increased precipitation density, were ascribed to the role of Ca. It is relevant to note the impact of calcium addition on the microstructure and functionality of the most well-known magnesium alloy, i.e. E. has previously been looked into, AZ31. Chaudry U.M [129] found that corrosion rates of the AZ31-0.5Ca alloy were significantly decrease compared to the base alloy AZ31, especially at pH 11. This improvement in corrosion resistance was attributed to the resulting improved distribution of the β phase from the Separation of aluminum and calcium. In a 0.01 M NaCl solution (pH = 12),Kim et al. [130] observed that Mg-5Al-1Ca had somewhat greater pitting resistance than Mg-5Al. As a result, various Ca concentrations as an alloying element were explored in order to enhance the corrosion behavior of Mg-5Al alloys. In addition, rolling during thermomechanical processing was found to be an effective way to improve the mechanical properties and regulate the corrosion behavior of magnesium-based alloys [131]. Ren et al. [132] found that heating high-purity magnesium at 500 °C for 10 hours increased the rate of corrosion because the grains got bigger and rougher. In fact, the enhanced resistance to corrosion was due to a uniform distribution, a decrease in the second phase's volume fraction, and a lowering of the internal stress [133]. It had been assumed that the crystallographic

orientations of the grains were another characteristic that significantly affects the corrosion anisotropy.

While the surface of the B1-B3 Ca specimens was not corroded, the A1-A3 specimens displayed severe corrosion. These findings align with the depression angle and potentiostatic findings. The A1-A3 samples developed some pits due to the formation of Cl-ions in this instance. In specimens containing Ca, the number of pits was decreased, while the 1.0 Ca specimen had no pits at all. This shows that as the amount of Ca added increased, the passive film's stability increased [128].

However, as reinforcement particles give the composite material its hardness and wear resistance as well as some other essential bulk properties, it is crucial to verify their presence. Therefore, using elementary mapping, the particles and their distribution in the developed composites carried out by this research are confirmed. The outcomes are displayed in Figure 4.1–4.12. The distribution of oxygen is indicated by the pale region in this mapping area, while the relevant colors for magnesium, aluminum, calcium, and cerium are red, green, purple, and yellow, respectively.

Table 4.2. SEM image of the prepared alloy following white Hank's solution corrosion.

	250X	1k
A1		

A2		
A3		
B1		
B2		

B3		
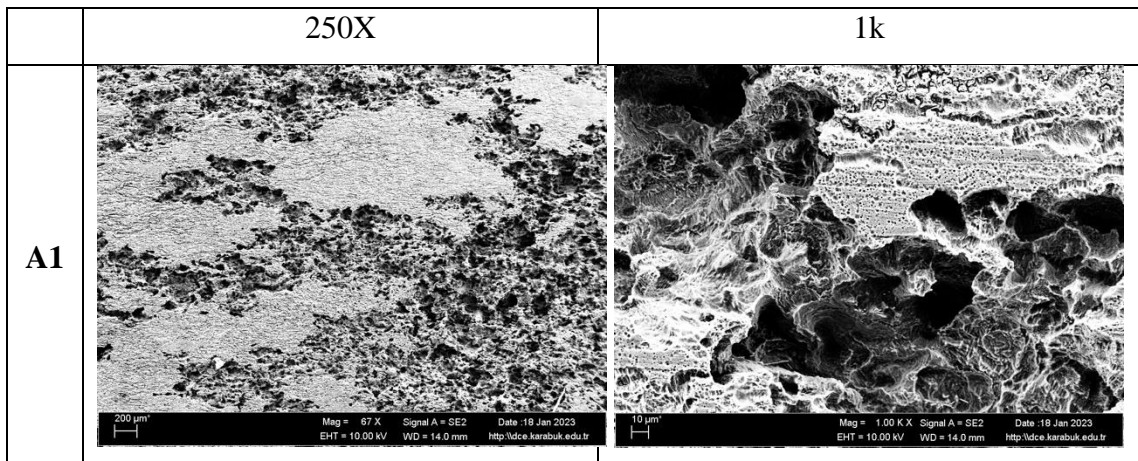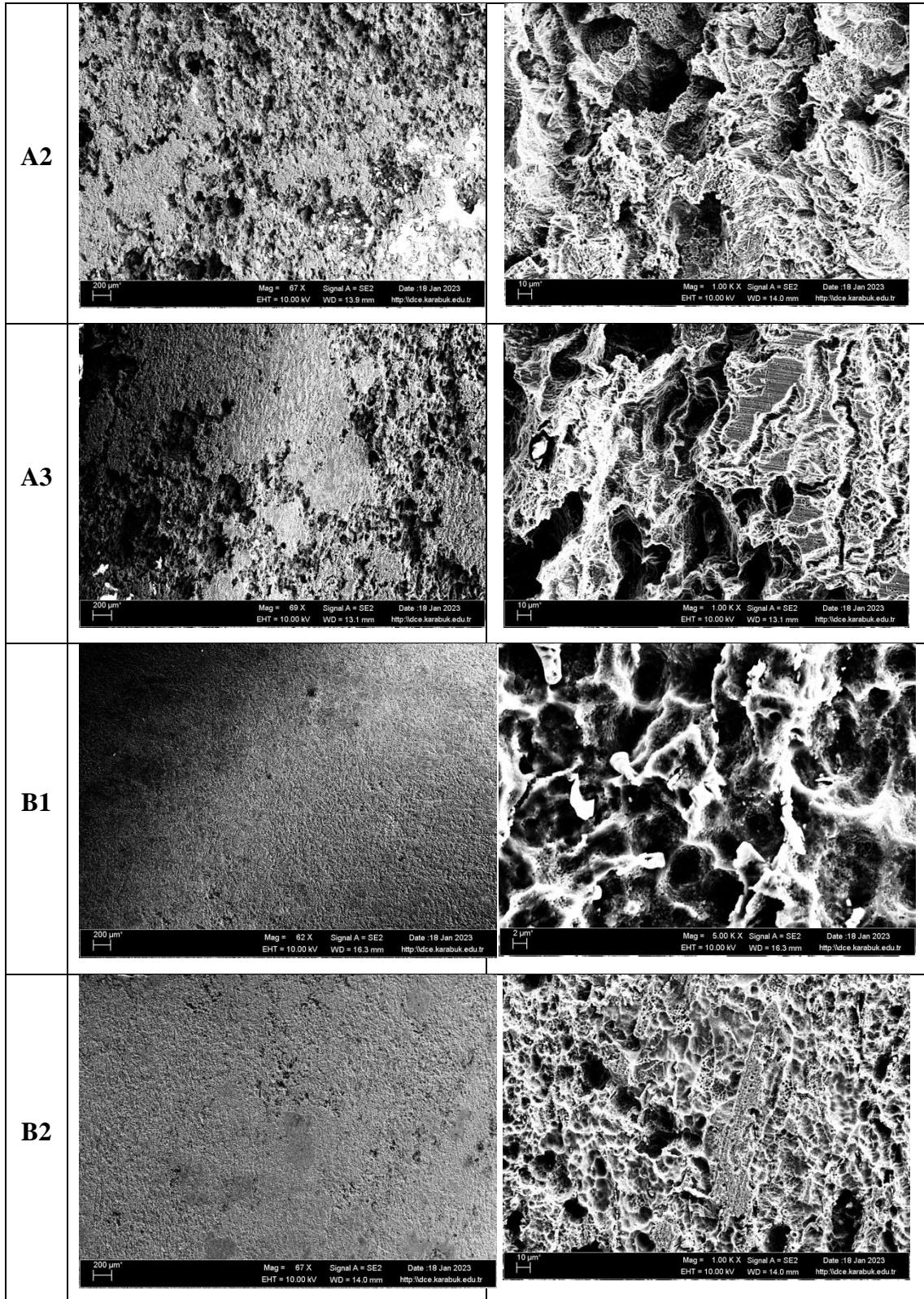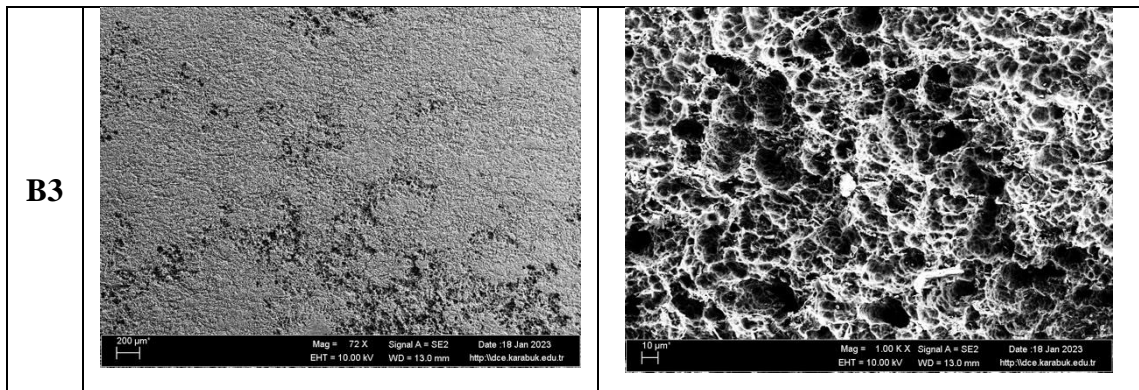
Table 4.3. SEM image of the prepared alloy following red Hank's solution corrosion.

	250X	3k
A1		
A2		
A3		
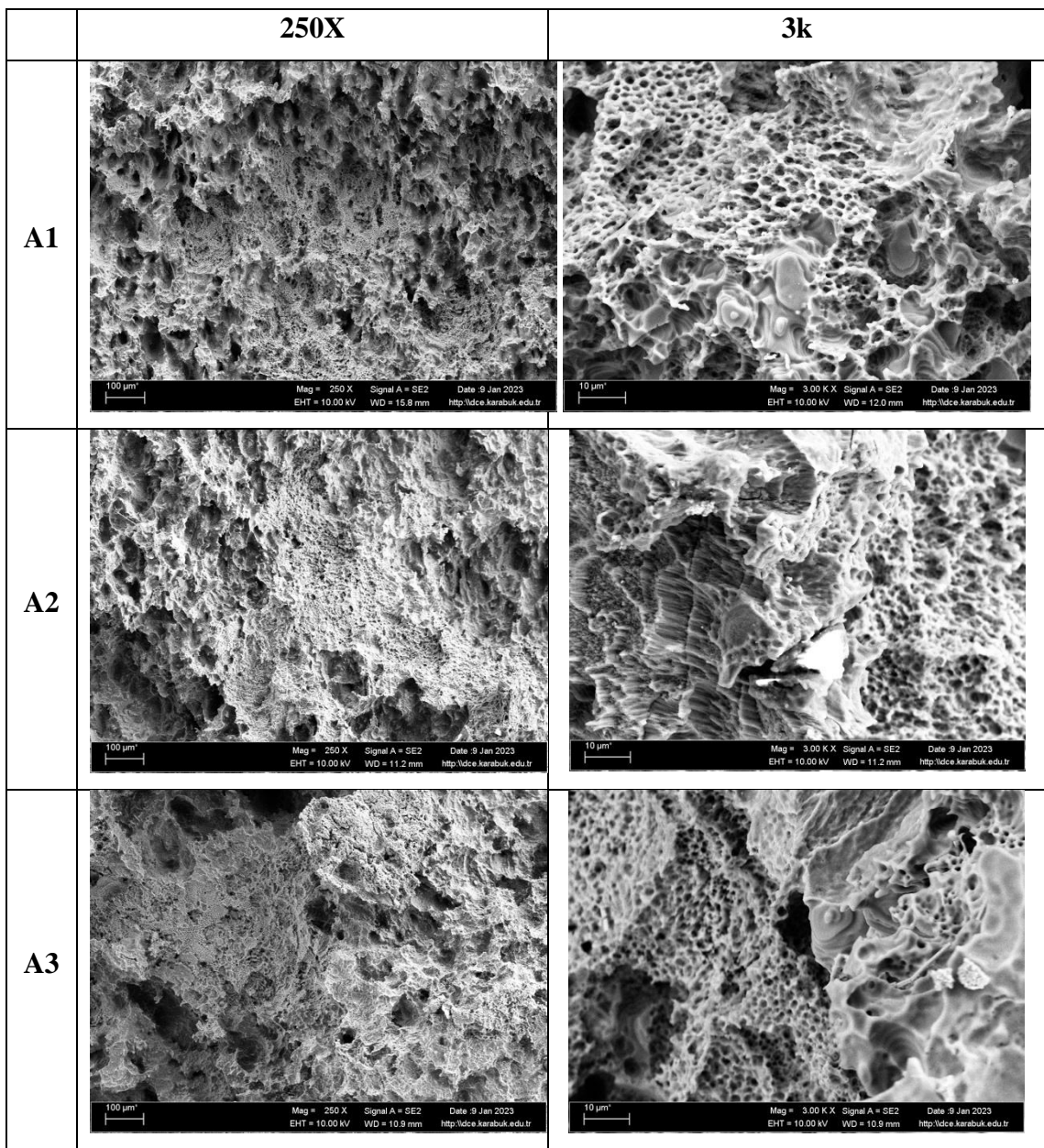
Figure 4.1. A1 sample after corrosion in white Hank's solution

Figure 4.2. A2 sample after corrosion in white Hank's solution

Figure 4.3. A3 sample after corrosion in white Hank's solution

s

Figure 4.4. B1 sample after corrosion in white Hank's solution
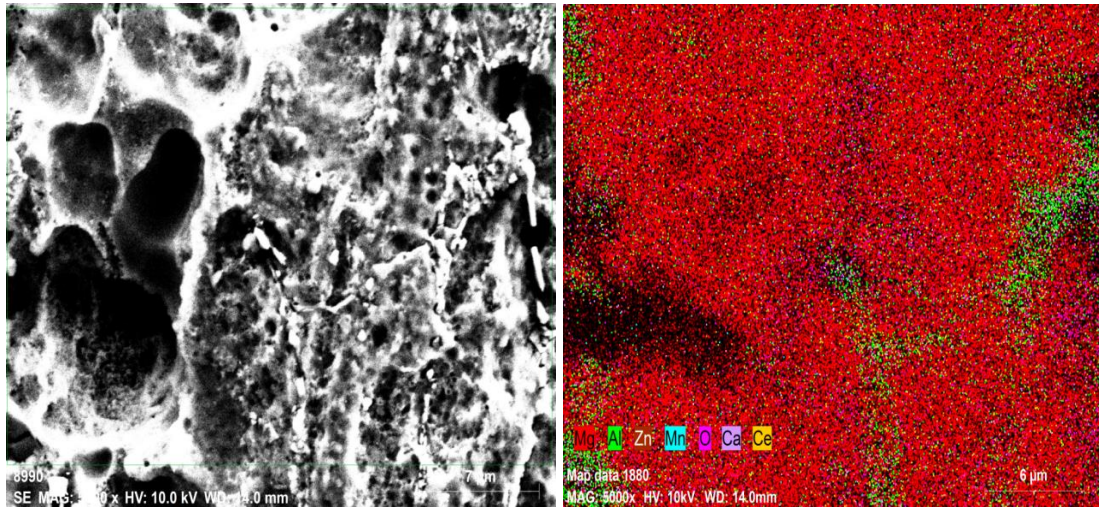
Figure 4.5. B2 sample after corrosion in white Hank's solution.
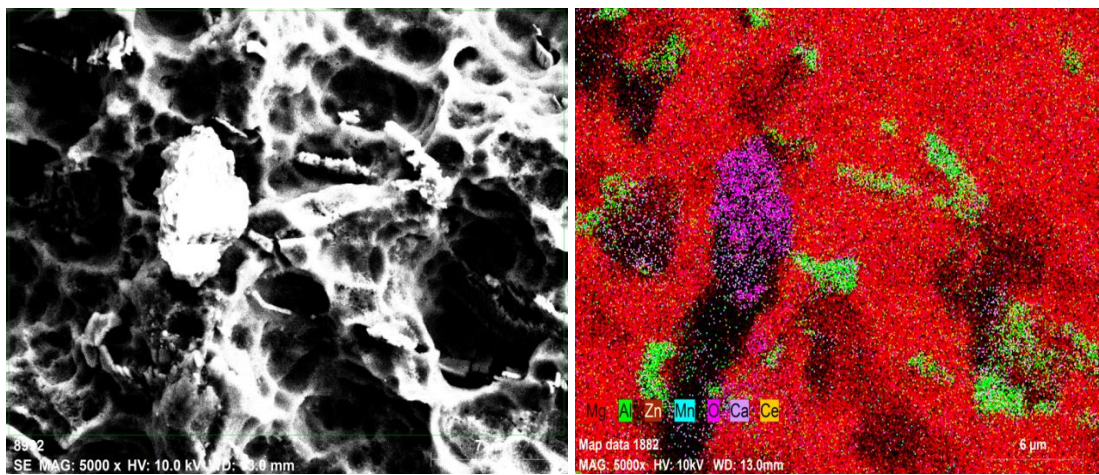
Figure 4.6. B3 sample after corrosion in white Hank's solution
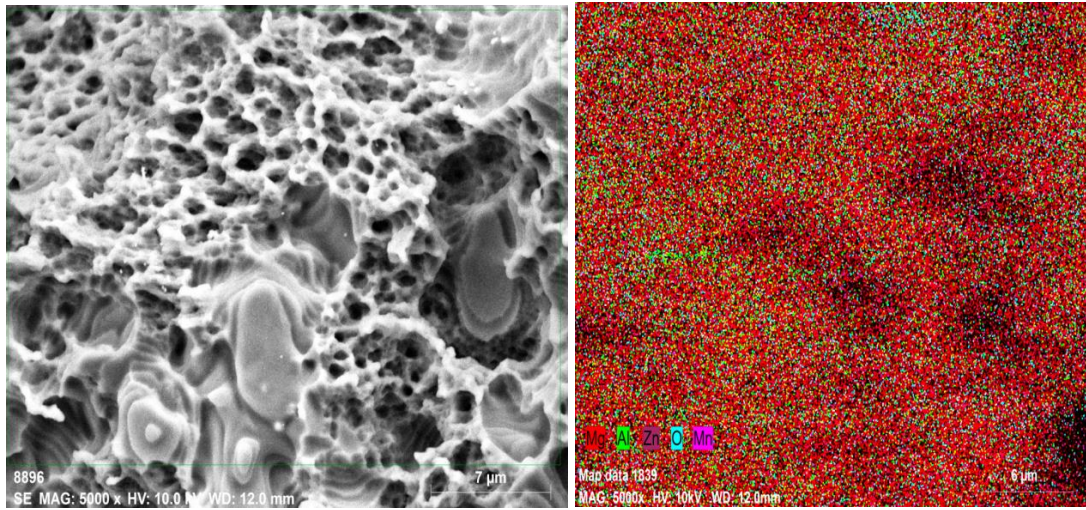
Figure 4.7. A1 sample after corrosion in red Hank's solution
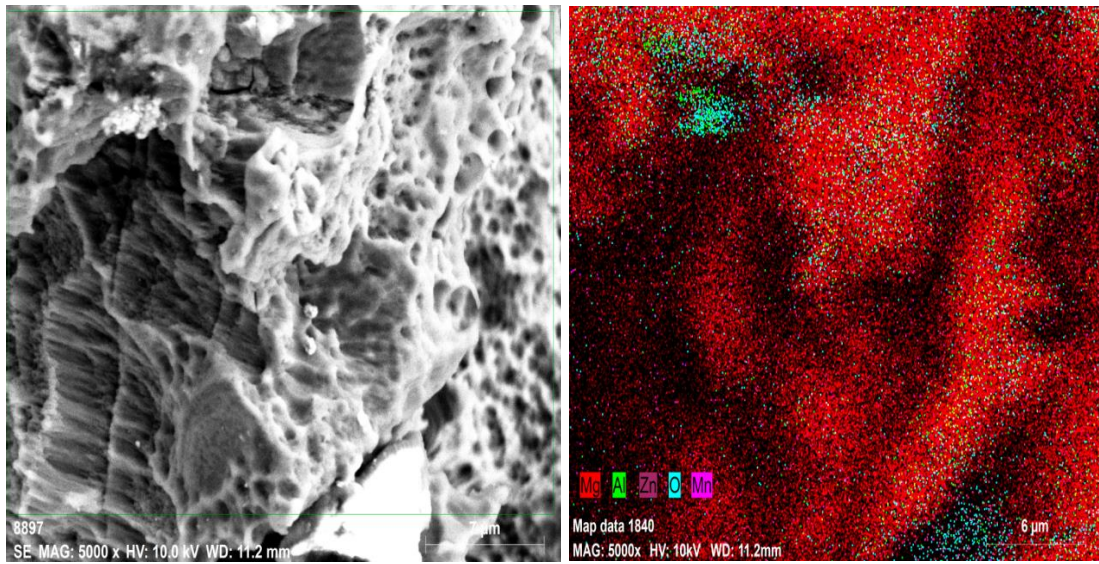
Figure 4.8. A2 sample after corrosion in red Hank's solution.
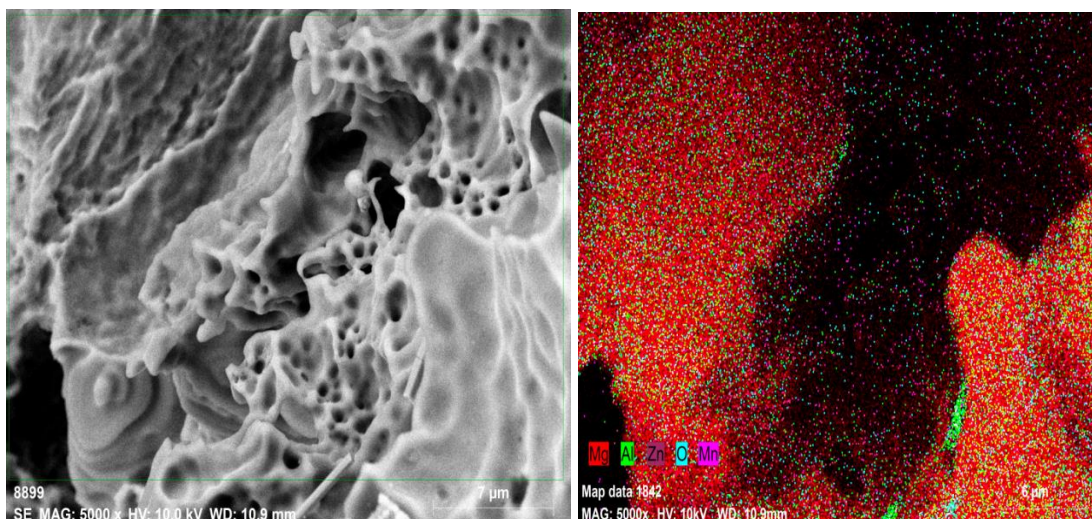
Figure 4.9. A3 sample after corrosion in red Hank's solution.
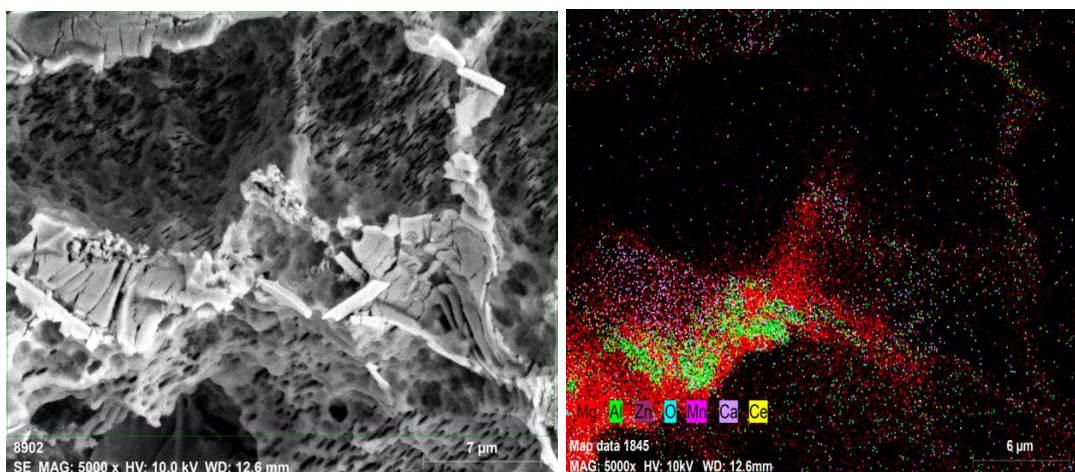
Figure 4.10. B1 sample after corrosion in red Hank's solution.
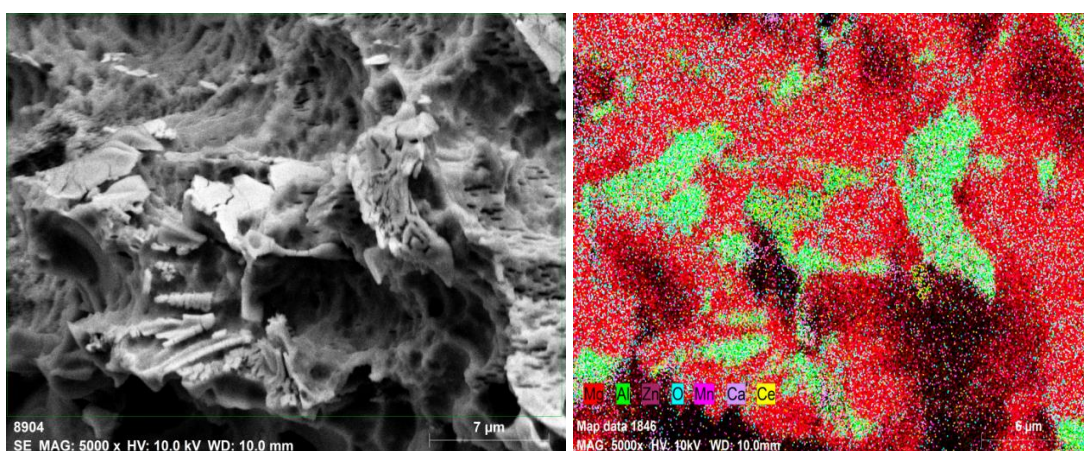
Figure 4.11. B2 sample after corrosion in red Hank's solution.

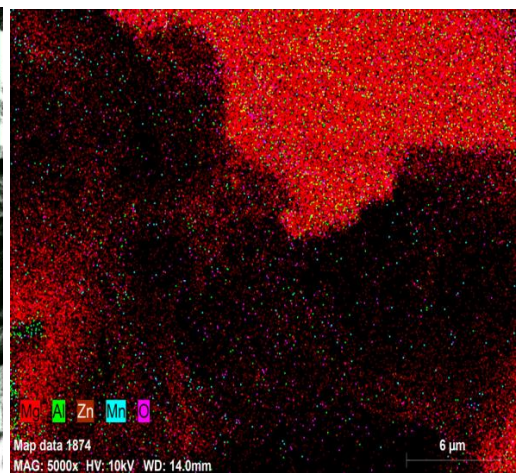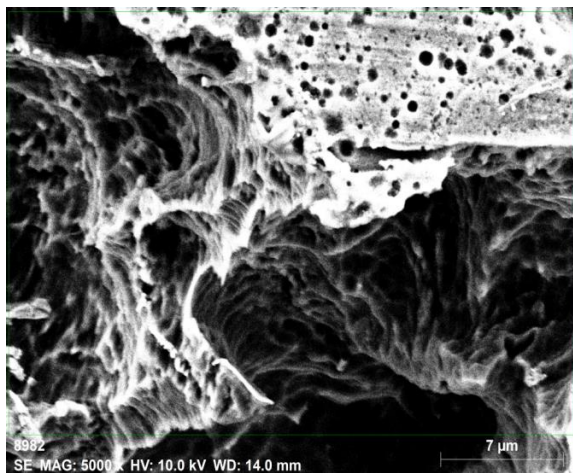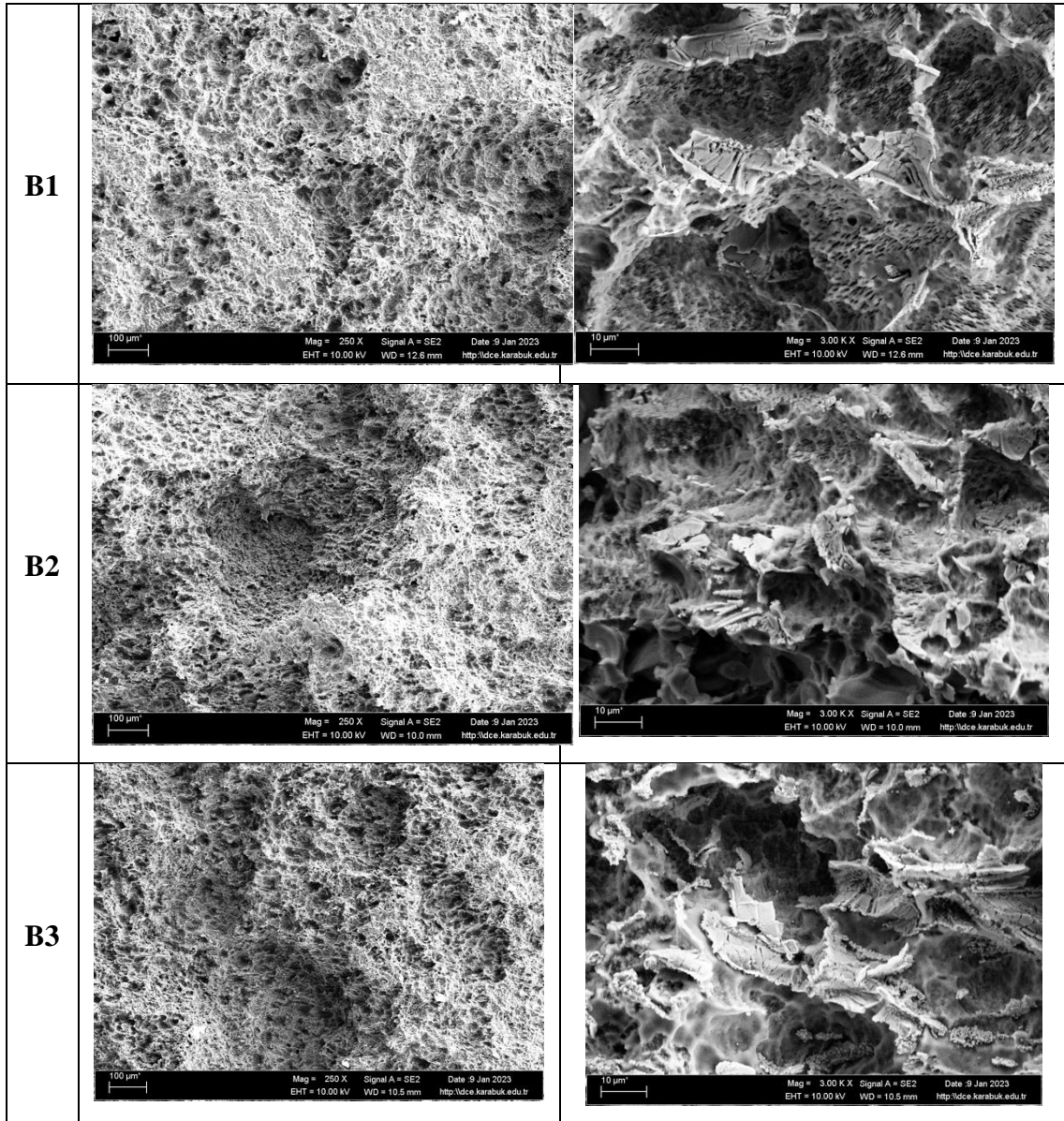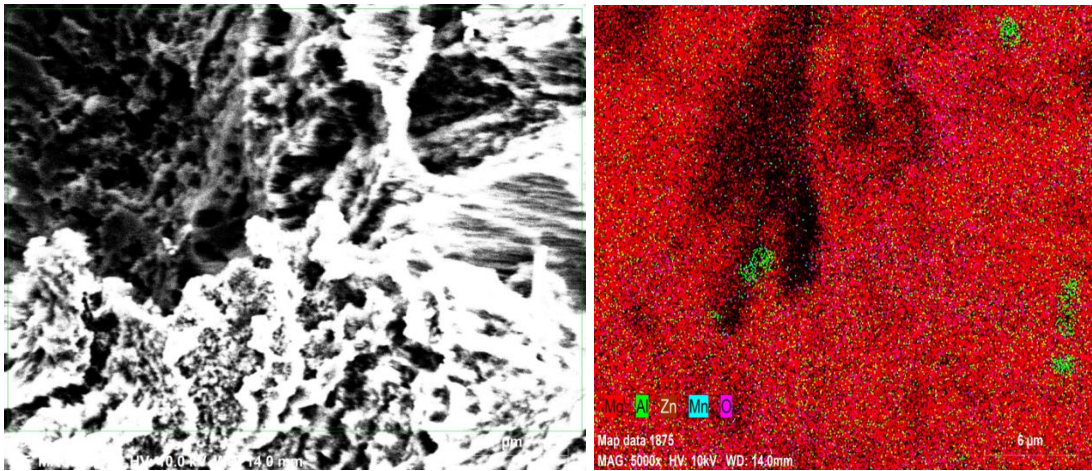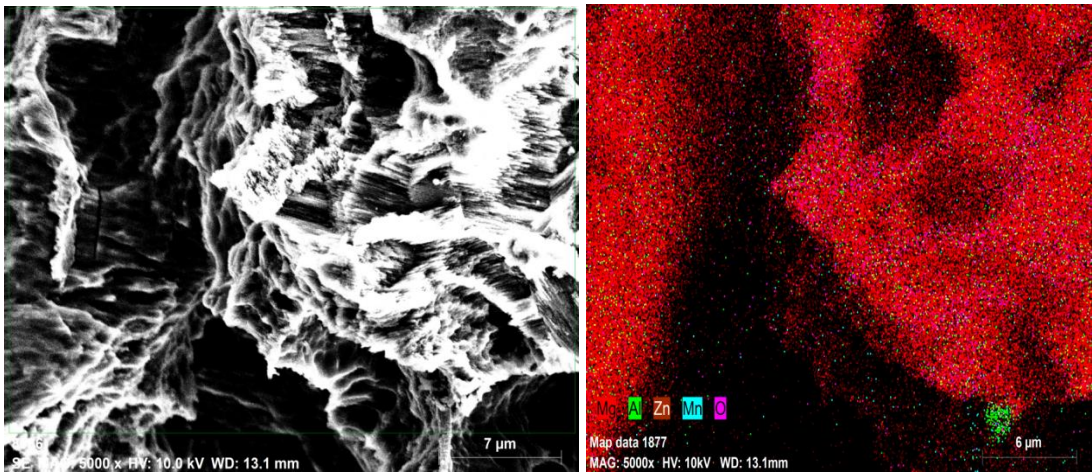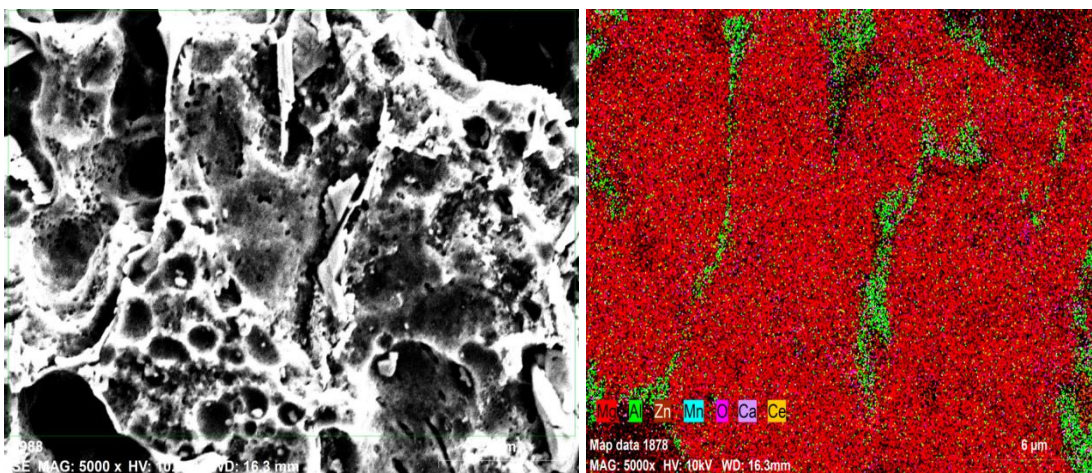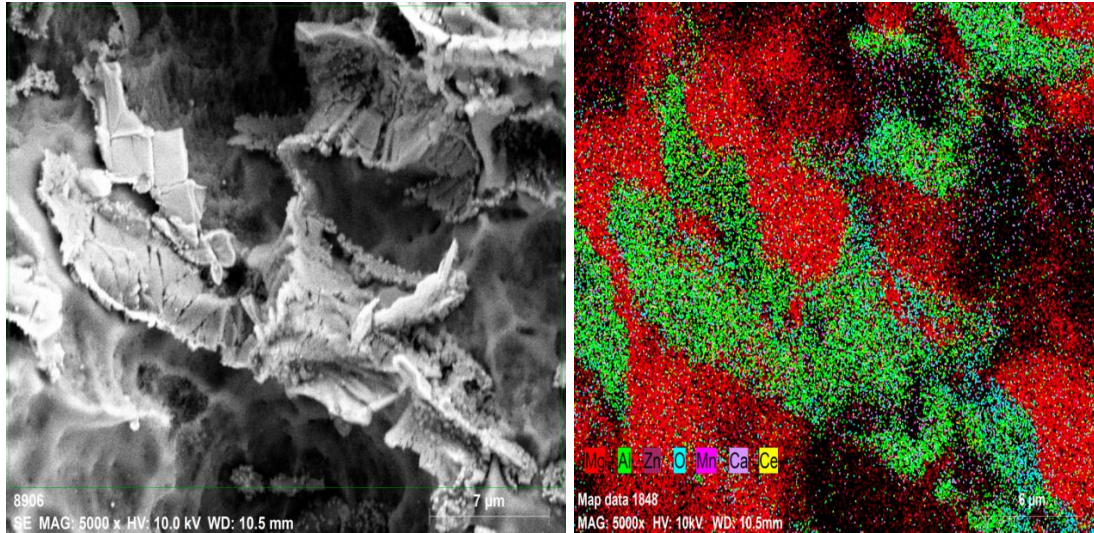Figure 4.12. B3 sample after corrosion in red Hank's solution.

Compare the surface morphology of the AZ31 magnesium alloy with polished and ground surfaces in Table 4.1. The ground sample has greater corrosion product layer cracking. The samples' surfaces had MgO, $Mg(OH)_2$, and phosphate corrosion products[134, 135]. detect the corrosive environment. Despite identical MgO and Mg(OH) product quantities, the ground sample has a larger phosphate-based corrosion product layer (a fractured layer visible on the surface behind the clusters of MgO and $Mg(OH)_2$ products). Compared to the alloy in enriched HBSS+ lacking Mg^{2+} and Ca^{2+} ions, the AZ31 magnesium alloy had a more stable corrosion reaction [32] .

4.3. XRD AND EDX OF THE PREPARED ALLOY

Figure 4.13 shows how XRD investigation revealed secondary phase variations between non-modified and modified Ca and Ce AZ31 Mg alloys. α-Mg and β-$Mg_{17}Al_{12}$ phases were often seen in the investigated alloys. The formation of secondary phases is influenced by the differences in electronegativity of the alloying elements; a larger difference facilitates the formation of distinct types. Al (1.61), Mn (1.55), Mg (1.31), Ce (1.12), and Ca (1.00) are the elements in order of electronegativity [136]. With the Ce addition at 21.68°, $Al_{11}Ce_3$ was also formed. Furthermore, there is a strong correlation between the Mn/Al weight ratio (1.20) and

the Al_8Mn_5 ratio (1.27) [117], which was detected on the AZ31 (Figures 4.14 and 4.15).
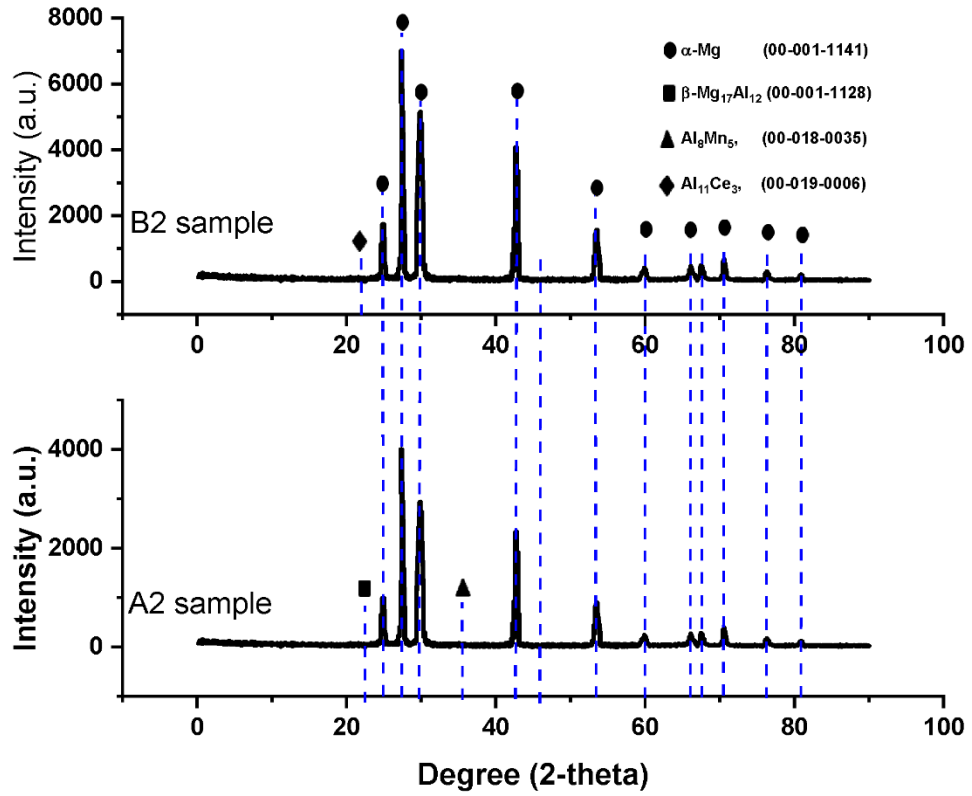
Figure 4.13. XRD for the prepared samples.
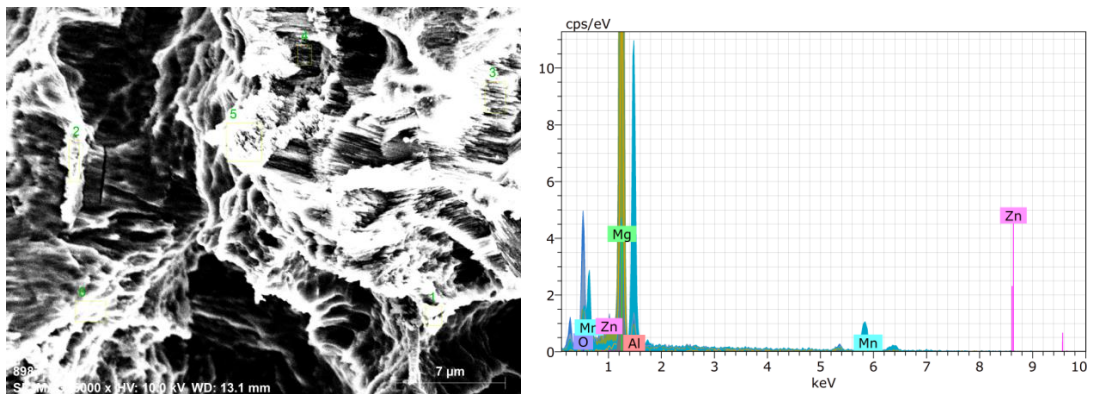
Figure 4.14. EDX for the A2 sample.
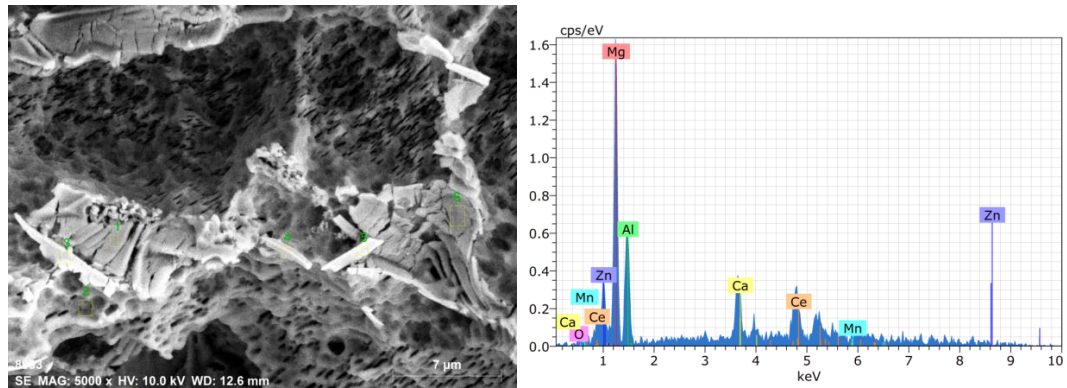
Figure 4.15. EDX for the B2 sample.

4.4. WEAR TEST

Samples with a diameter of 10 mm were evaluated for wet wear at constant sliding speeds of 1 m · sec-1, with weights of 2 and 4 N and sliding distances of 0.5, 1, 1.5, 2, 2.5 mm. The samples' wear resistance is shown in Table 4. 4 and Figure 4.16, which make it evident that weight loss increased as applied loads increased. This is because as the material's load increases, surface friction increases. The added Ca and Ce allowed the hot rolled samples from 90°, 45°, and 0° angles to RD to have higher wear resistance values, as the results demonstrate. The values of A1–3 and B1–3, two similar alloys, follow the same trend when it comes to surface profile and specific wear rate evaluation: 45° > 0° > 90°. Additionally, compared to the A3 specimen, B3's wear resistance increased by more than two times. It has been reported that temperature influences the strain value of AZ31 up to the fracture point because rising temperatures increase the activity of non-basal slip systems.

In Table 4.4, the two-dimensional (2D) profiles of the worn surfaces demonstrate the wear reduction on the prepared alloy following the addition of Ca and Ce to the base alloy; the wear tracks were shallower and narrower than those obtained for the prepared alloy. Notably, there was very little material that was plastically deformed at the wear path edges.

Table 4.4. Two-dimensional (2D) profiles of wear tracks for the prepared alloy under load 2 and 4 N.

2 N	4 N
A1	A1
A2	A2
A3	A3
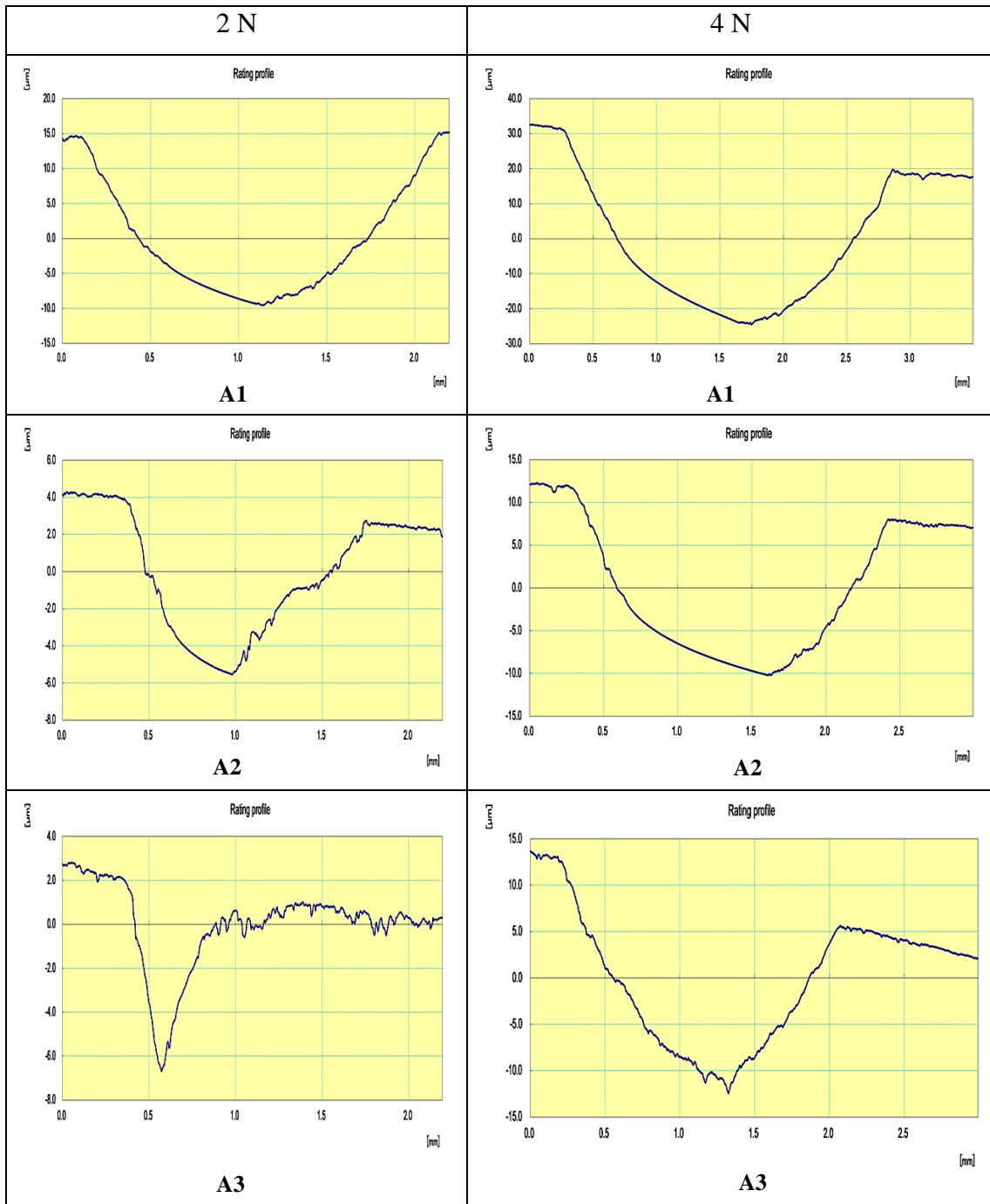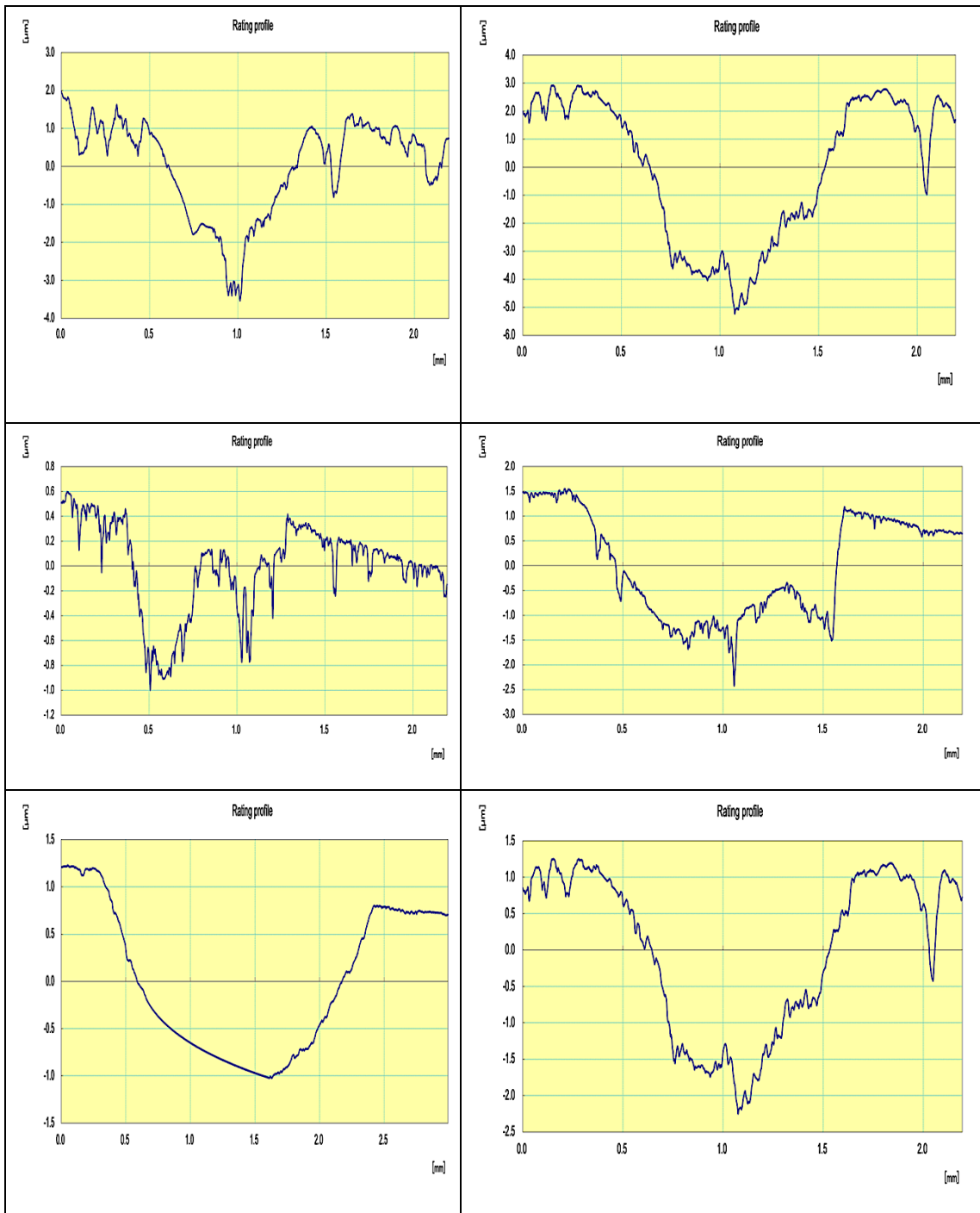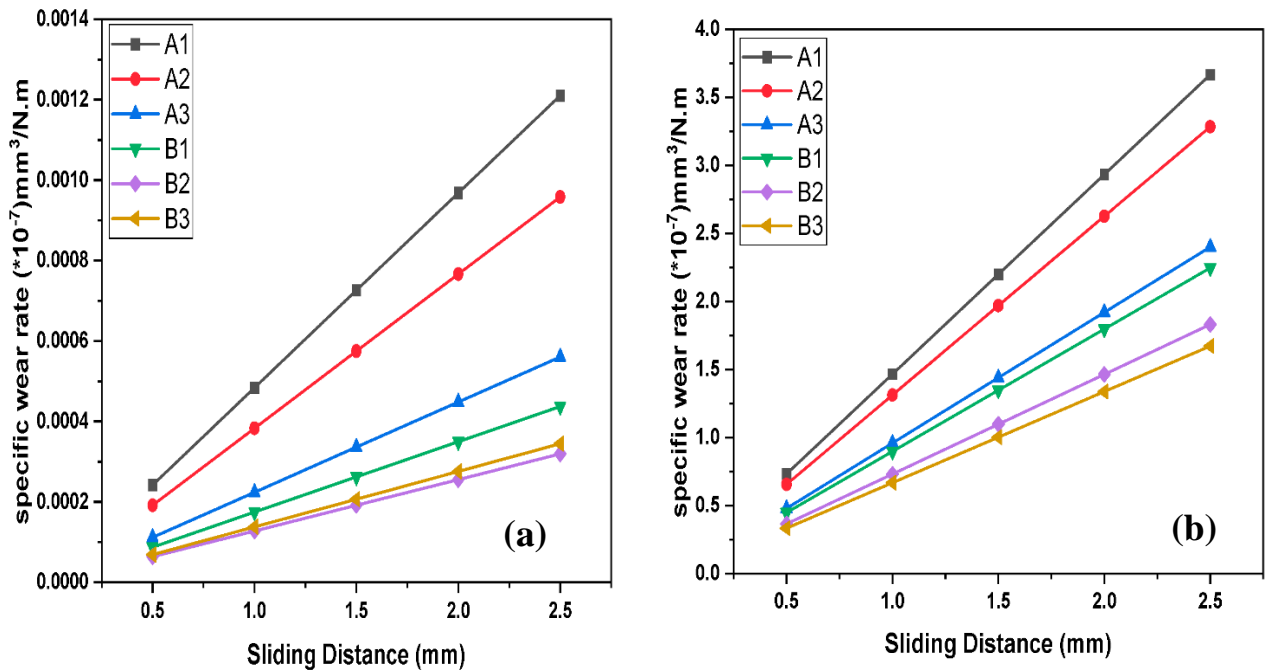
Figure 4.16. Specific wear rate fort he prepared alloy in White Hank's solution under a)2 N, and b) 4N.

The wear behavior of magnesium alloys has been found to be influenced in part by synthetic bodily fluids. The fact that it lowers the coefficient of friction by creating a positive lubricating effect is among the most significant. By doing so, wear loss may be avoided[137]. Body fluids also corrode magnesium in another scenario. Since there is an instantaneous electrochemical reaction the moment the magnesium alloy comes into contact with bodily fluid. Anodic and cathodic reactions are brought on by this. Galvanic corrosion of the α Mg matrix is believed to occur as a result of various phases in the Mg alloy following this interaction. Moreover, flaking wear debris and mechanical wear both cause abrasive wear and accelerate the corrosion process that damages the protective film created by iron. This loosening and porosity of the magnesium alloy's surface increases its wear resistance due to Hank's fluid wear effect. The magnesium alloy also corrodes readily because it is prone to scratching under heavy loads. In addition to aggravating wear on the magnesium alloy, the two influencing factors work in tandem [137, 138]. In contrast to the intermetallics in the casting microstructure, any potential intermetallics that emerge

in the microstructure following extrusion appear thinner and more evenly distributed. These intermetallics, however, appear more coarse-grained and extend along the grain boundaries in the cast structure.

4.5. ELECRTOCHEMICAL ANALYSIS

4.5.1. Results of the Immersion Corrosion Test

The specimens were subjected to a corrosion analysis and reaction in the Mg alloy (AZ31 and AZ31-1Ca-0.5Ce) by immersing in HBSS and HBSS+ solutions for three days (72 hrs.) in the laboratory of the Karabuk University Faculty of Engineering. After that, each specimen was removed at a designated time, weighed, and returned to the solutions, as illustrated in Figure 4.17. As the intensity of the sandblasting process increased, corrosion appeared. The literature studies show that as the surface area increases, the roughness also increases due to the sandblasting effect, which reduces corrosion resistance. When Ca and Ce were added, it was found that the corrosion resistance of grade AZ31 materials based on magnesium increased. All of the samples' weight loss increases with immersion time, as seen in Figure 4.17 a, and b. In both solutions, the weight loss appears to be highest in the first 24 hrs. of immersion, after which weight loss tapers off. Sample A3 has the highest total weight loss while sample B2 has the lowest in the white solution, while sample A1 has the highest weight loss in the red solution and B2 has the lowest weight loss. The AZ31 samples (A1, A2, A3) showed increasing weight loss over time, indicating continuous corrosion in the solution. The Ca-containing samples (B1, B2, B3) had significantly lower weight loss than the AZ31 samples at most time points. This indicates improved corrosion resistance of Ca. The improvement by adding Ca varies depending on the sample. For example, after 8 hours, B1 had >10 times less weight loss than A1, while B3 had about 2 times less weight loss than A3. This indicates that the influence of Ca depends on the specific sample. Weight loss trends over time differ between the AZ31- and Ca-containing samples. The AZ31 samples tend to show increasing weight loss with prolonged immersion. The Ca-containing samples show greater fluctuations in weight loss over time, suggesting a different corrosion mechanism. When comparing the results between the use of two different solutions,

HBSS+ (white solution) and HBSS (red solution), it is shown that adding Ca in HBSS+ significantly improved the corrosion resistance, with samples containing Ca up to 10 times less Weight loss than AZ31 samples, while in HBSS the effect of Ca addition is less pronounced. Weight losses are more similar for AZ31- and Ca-containing samples. For HBSS, the AZ31 samples show a very high weight loss with longer immersion times (48, 72 hours) compared to HBSS+. This suggests that the composition of HBSS leads to greater corrosion of AZ31.HBSS, the Ca-containing samples still have a lower weight loss than AZ31 after 48 and 72 hours of immersion, but the difference is smaller (5x) compared to HBSS+ (> 10x difference). Both solutions still have the anti-corrosion effect of the Ca addition, but the effect is diminished when HBSS is added. Thus, the corrosion mechanism and the potency of Ca are affected by the composition of the solution. The above-mentioned galvanic effect between the matrix and the grain boundaries causes the dissolved Ce molecules to have a major impact on the material's corrosion behavior. Ce primarily diffuses into the matrix [139, 140]. Significantly faster corrosion is seen in secondary phases rich in Al- Ca. Hence, the stable $Mg_{17}Al_{12}$ secondary phases are eliminated from the structure by Ce compounds with Al and are replaced by AlRE3 types. [141].
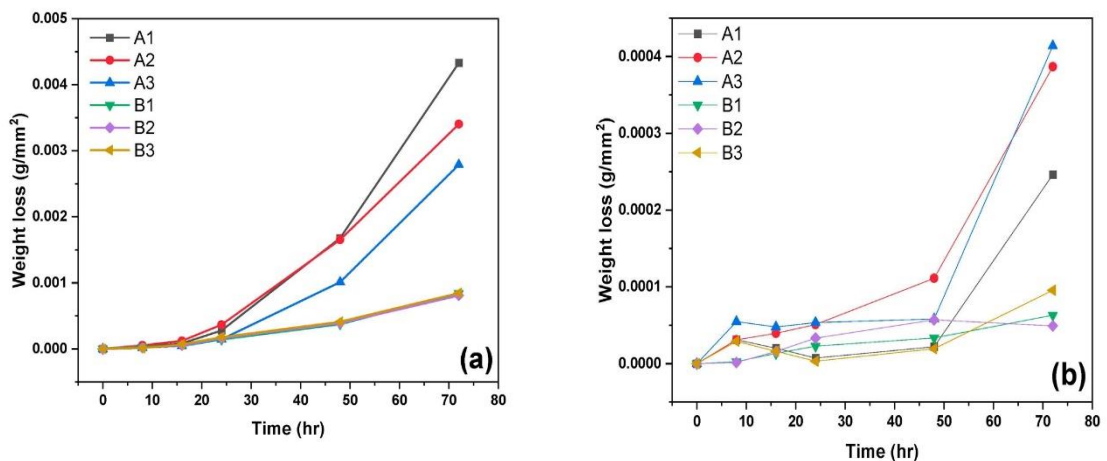
Figure 4.17. Weight loss of the prepared alloy against the time of immersion in a) Red solution, and b) White solution.

74

Figures 4.18 and 4.19 show the appearance of the exposed areas of the three samples after immersion test after 72 hr. in HBSS and HBSS$^+$ solution. The protective effect of the layer can be verified by the appearance of the piece. In the as-received and sanded samples, the entire exposed area is damaged, while in the treated sample only a small area within the exposed area has been corroded.

Figure 4.18. Image of the prepared samples after polarization analysis in HBSS solution.

Figure 4.19. Image of the prepared samples after polarization analysis in HBSS$^+$ solution.

4.5.2. Results of the Potentiodynamic Polarization Corrosion Test

The potentiodynamic polarization curves of the AZ31 alloy, both with and without the addition of Ca and Ce, are shown in Figures 4.20–421. The corrosion rate (mpy) diagrams are shown in Figures 4.20 (a and b), which were obtained after rolling. The Ca and Ce were obtained with the addition of Ca. Tables 4.5 and 4.6 provide the values for the two distinct solutions (HBSS and HBSS+ solution) based on the polarization curves for the corrosion potential (Ecorr), corrosion current density (Icorr), and Beta C and Beta A (V/decade).
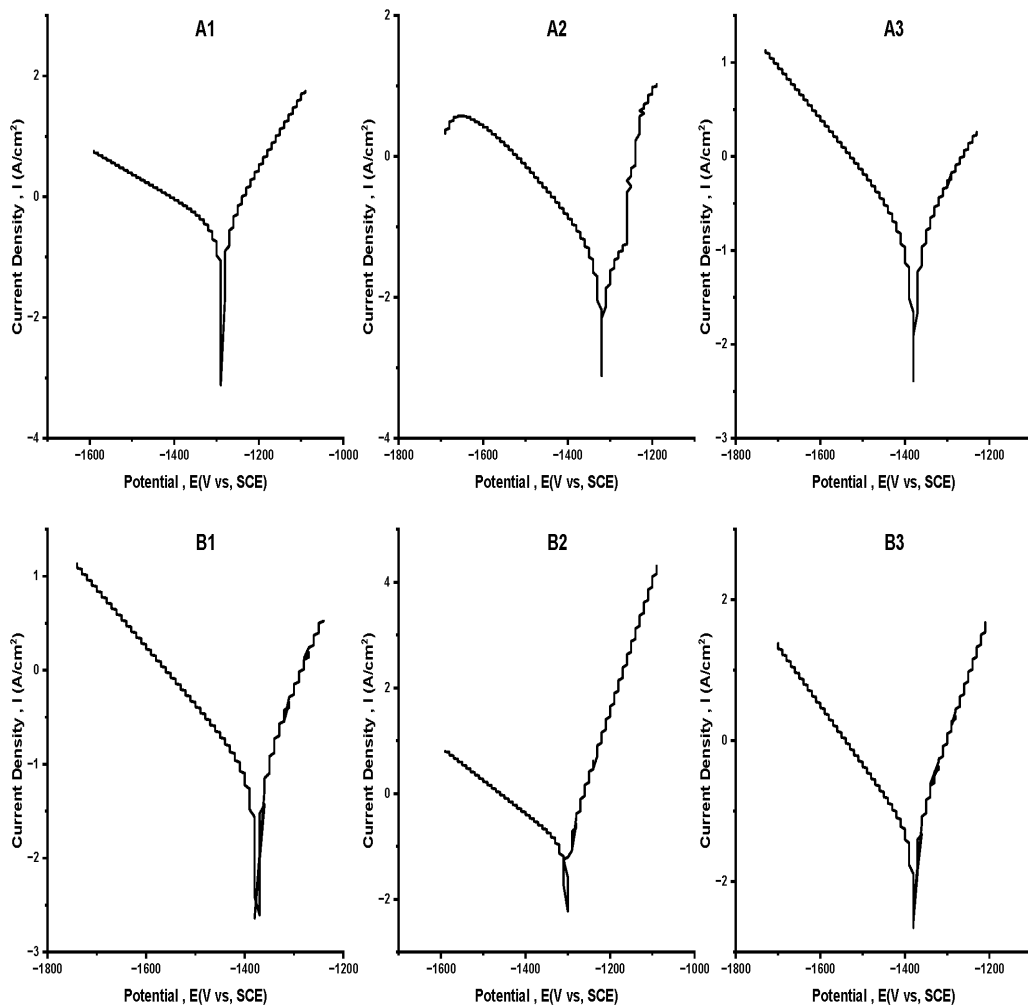
Figure 4.20. Potentiodynamic diagram for prepared samples in HBSS solution.
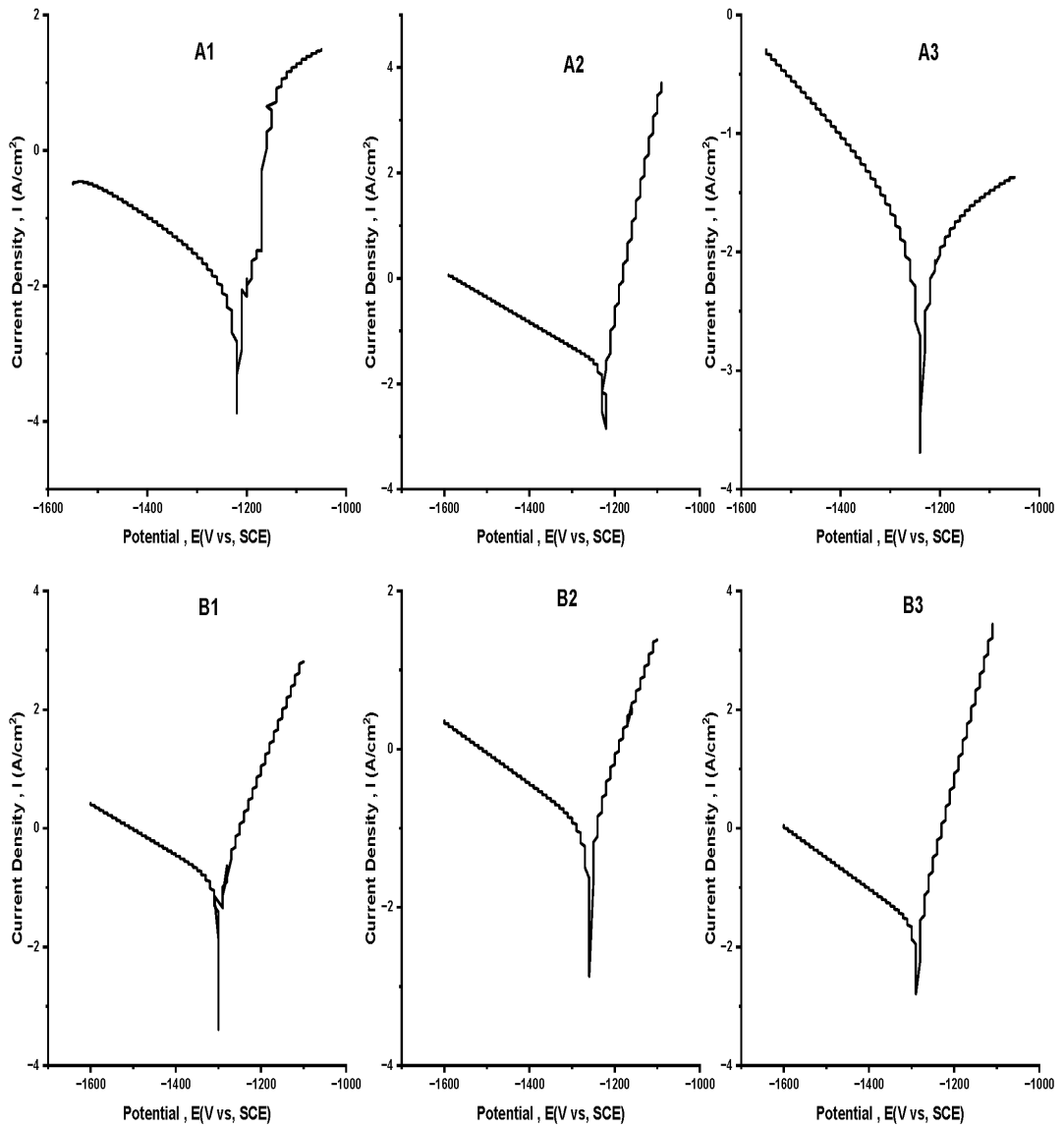
Figure 4.21. Potentiodynamic diagram for prepared samples in HBSS+ solution.

Table 4.5. Icorr and Ecorr rates for the prepared alloy's corrosion test in HBSS solution.

Sample	E_{corr} (v)	I_{corr} ($\mu A/cm^2$)	BetaC (V/decade)	BetaA (V/decade)
A1	-1,290	321	245,1e-3	86.40e-3
A2	-1.320	51.30	159,0e-3	242,8e-3
A3	-1,380	150	179,8e-3	136,7e-3
B1	-1,370	73.5	162.5e-3	78,70e-3
B2	-1.300	104	159,1e-3	40,70e-3
B3	-1,380	44.6	119,3e-3	57,00e-3

The samples containing Ca and Ce (B1-B3) have an open circuit potential (Ecorr) that is marginally higher than the samples containing neither Ca nor Ce (A1-A3), as shown by Figure 4.20 and Table 4.4. This suggests that the HBSS solution's ability to inhibit corrosion in AZ31 alloy can be enhanced by the addition of Ca and Ce.

Samples containing Ca and Ce (B1 and B3) have a corrosion current density (Icorr) that is generally lower than samples containing neither Ca nor Ce (A1-A3). This suggests that the addition of Ca and Ce lowers the rate at which AZ31 can alloy corrodes in HBSS solution.

The samples containing Ca and Ce (B1-B3) have cathodic Tafel slope (Beta C) and anodic Tafel slope (Beta A) that are generally lower than those of the samples containing Ca and Ce (A1-A3). This suggests that adding Ca and Ce can increase the cathodic and anodic polarization resistance of the AZ31 alloy in HBSS solution.

With its lowest Icorr value of 44.6 $\mu A/cm^2$, B3 is the best sample for corrosion resistance according to result. With a corrosion current density of -1.38 V, B3 has the lowest rate of metal dissolution. Its high tendency to be protected from corrosion by forming a passive film on its surface is further indicated by its Ecorr value of -1.38 V. The anodic and cathodic Tafel slopes are represented by the Beta A and Beta C values, respectively. They have to do with how quickly the electrochemical processes that take place during corrosion occur. The lower the Tafel slopes, the more difficult

the reactions are. The sample B3 has the lowest Beta C value of $119.3e^{-3}$ V/decade, which means that it has the lowest cathodic reaction rate. The sample B3 also has a relatively low Beta A value of $57.00e^{-3}$ V/decade, which means that it has a low anodic reaction rate.

Table 4.6. Icorr and Ecorr rates for the prepared alloy's corrosion test in HBSS[+] solution.

Sample	E_{corr} (v)	I_{corr} ($\mu A/cm^2$)	BetaC (V/decade)	BetaA (V/decade)
A1	-1,220	5.88	163,9e-3	43,80e-3
A2	-1.230	21.80	211,4e-3	25,00e-3
A3	-1.240	19.80	223,4e-3	503,6e-3
B1	-1,300	130	233,1e-3	52,40e-3
B2	-1.260	103	256,4e-3	65,00e-3
B3	-1.290	24.40	191,0e-3	35,80e-3

From the table, we can see that the open circuit potential (Ecorr) of the samples with Ca and Ce (B1-B3) is slightly lower than that of the samples without Ca and Ce (A1-A3). This indicates that adding Ca and Ce negatively impact the corrosion resistance of AZ31 alloy in the HBSS+ solution.

The corrosion current density (Icorr) of the samples with Ca and Ce (B1-B3) is generally higher than that of the samples without Ca and Ce (A1-A3), indicating that the addition of Ca and Ce increases the corrosion rate of AZ31 can alloy in HBSS[+] solution. The cathodic Tafel slope (Beta C) of the samples with Ca and Ce (B1-B3) is generally higher than that of the samples without Ca and Ce (A1-A3), indicating that the addition of Ca and Ce can reduce cathodic polarization resistance from AZ31 alloy in HBSS+ solution.

The anodic Tafel slope (Beta A) of the samples with Ca and Ce (B3) is generally lower than the samples without Ca and Ce (A3), indicating that the addition of Ca and Ce can increase the anodic polarization resistance of AZ31 alloy in HBSS[+] solution.

In summary, based on the Icorr, Ecorr and beta values, samples A1, A3 and B3 demonstrated the highest corrosion resistance in the HBSS+ solution, while sample B1 performed the poorest with the highest corrosion rate.

The alloys containing only magnesium, cerium, and calcium—each containing extra alloying elements—are the outcomes of the potentiodynamic polarization tests. Initial corrosion rate measurements are typically used to evaluate the corrosion behavior of magnesium alloys. These measurements are obtained through short-term methods, such as polarization curves or impedance measurements taken right after the sample is submerged in the electrolyte. For practical purposes, it is crucial to have quick and precise techniques for determining the rates of alloy corrosion [142].

According to TKacz et al.[143] found pitting corrosion attack on samples but no Epit on curves. These Mg^{2+}, Cav^{2+}, and sulfate ions may have made the magnesium alloys more reactive in enhanced HBSS+. The corrosion potential Ecorr of AZ31 alloys in HBSS without Mg^{2+} and Ca^{2+} ions is more negative than in enriched HBSS+.

Figure 4.22 a shows that the corrosion current density (Icorr) and subsequent corrosion rate (Vcorr) were higher in the HBSS corrosion environment without Mg^{2+} and Ca^{2+} ions, as reported in [143], This is due to the ions' presence or absence in the solution, especially the Mg^{2+} ions. While Mg^{2+} and Ca^{2+} ions are absent from HBSS, the concentration gradient might be significant [144, 145]. Magnesium in the alloys reacts with the corrosion environment to produce Mg^{2+} ions. Initially, the samples are submerged in a solution without any Mg^{2+} ions. Due to the concentration gradient, the Mg^{2+} ions move from the sample's surface, where there is a high concentration of ions, to the HBSS, which has a low concentration of ions (without Mg^{2+} and Ca^{2+} ions). Surface reactions of the AZ31 alloys with the corrosion environment are facilitated by the migration of Mg^{2+} ions. However, since Mg^{2+} ions predominate in the corrosion environment, the concentration gradient of enriched HBSS+ containing Mg^{2+} and Ca^{2+} ions should be smaller than the solution without the ions. Magnesium alloy surfaces interact with the corrosion environment less frequently because the migration of Mg^{2+} ions from the alloy surface to the corrosion environment occurs more slowly than in HBSS without Mg^{2+} and Ca^{2+} ions.
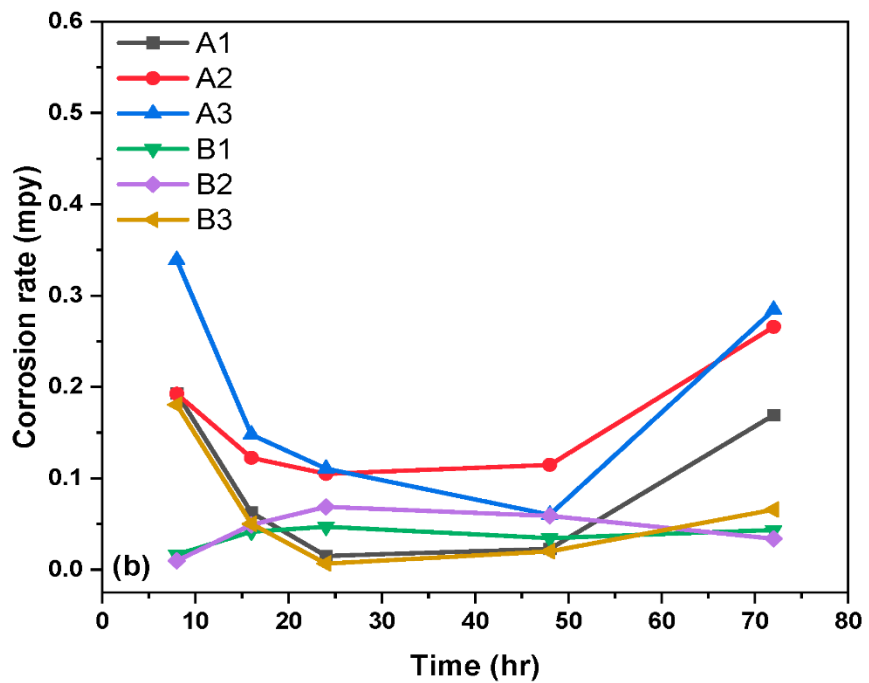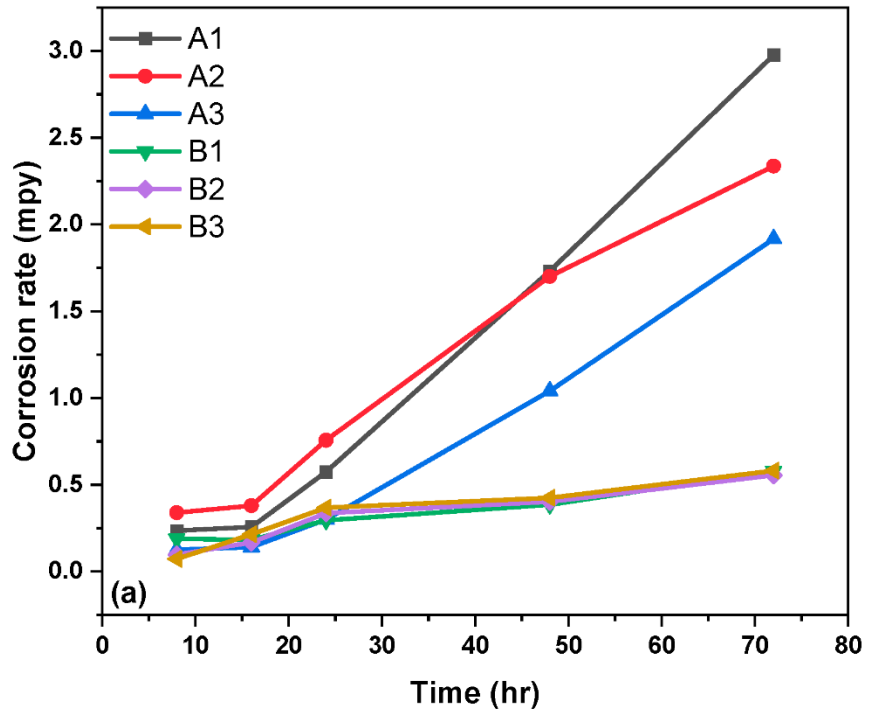
Figure 4.22. Weight loss of the prepared alloy against the time of immersion in a) Red solution (HBSS) , and b) White solution (HBSS$^+$).

The corrosion rate of AZ31 alloy was compared in two different solutions, namely HBSS and HBSS+. The results, depicted in Figure 4.20 (a, b), indicate that the presence of Ca and Ce in solution B1-B3 markedly decreases the corrosion rate when compared to samples A1-A3 in HBSS solution.

In the HBSS solution, corrosion rate of AZ31 alloy increasing with immersion time. For example, the corrosion rate of samples A1-A3 after 72 hours is between 2.97 and 1.92 $\mu A/cm^2$, while the corrosion rate of samples B1-B3 is between 0.58 and 0.03 $\mu A/cm^2$. This indicates that adding Ca and Ce to solution B1-B3 improved the AZ31 alloy corrosion resistances.

In the HBSS+ solution, the corrosion rate of the AZ31 alloy is significantly lower than in the HBSS solution. For example, the corrosion rate of samples A1-A3 after 72 hours is between 0.17 and 0.28 $\mu A/cm^2$, while the corrosion rate of samples B1-B3 is between 0.03 and 0.17 $\mu A/cm^2$. This indicates that the HBSS+ solution is less corrosive to the AZ31 alloy than the HBSS solution.

Overall, adding Ca and Ce to the solution, B1-B3, significantly reduced the corrosion rate of AZ31 alloy compared to samples A1-A3 in HBSS solution. In addition, the $HBSS^+$ solution is less corrosive to the AZ31 alloy than the HBSS solution. The corrosion rate of the samples rolled perpendicular to the rolling direction (A1, B1) was lower than that of the samples rolled parallel to the rolling direction (A2, B2) and the samples rolled transversely to the rolling direction (A3, B3). Both solutions indicate that the rolling direction significantly influenced the corrosion behavior. This could be related to the grain size, shape, orientation, and texture of the alloy sheets. The samples rolled perpendicular to the rolling direction had the finest and most equiaxed grains, the most random orientation distribution, and the weakest base texture, resulting in the highest ductility and formability as well as the lowest anisotropy and galvanic corrosion [146, 147]. The samples rolled parallel to the rolling direction had an intermediate grain size and shape, orientation distribution, and base texture, resulting in medium corrosion resistance. The samples rolled transversely to the rolling direction had the coarsest and most elongated grains, the most aligned orientation distribution, and the strongest base texture, resulting in the

lowest ductility and formability and the highest anisotropy and galvanic corrosion[147].

4.5.3. Electrochemical Impedance Measurement (EIS) Results

After electrochemical impedance measurements (EIS) of hot rolled AZ31 alloys in various directions with and without the addition of Ca and Ce, Figure 4.23 (a and b) displays the Nyquist curves that were produced. Upon closer inspection, it was discovered that the alloys' resistance to corrosion varied depending on the alloying element added. According to Figure 4.23a) of the Electrochemical Impedance Measurement (EIS) results, the AZ31 alloy (samples B1–B3) that had Ca and Ce added to it had lower impedance values than the samples that did not have those additions (samples A1–A3). This suggests that incorporating Ca and Ce enhanced the AZ31 alloy's ability to withstand corrosion.

The Nyquist curves indicate that, in comparison to immersion in HBSS, the immersion in HBSS$^+$ appears to have a considerable impact on the impedance spectrum of the system. Indicating that the system's capacitance has increased following immersion in HBSS$^+$, the curves in BBSS + have smaller diameters than the curves in HBSS solution. Possible explanations for this include the formation of a more uniform and compact layer on the system's surface, which raises the double-layer capacitance and lowers the charge transfer resistance.

The curves in HBSS$^+$ are shifted to the right compared to the curves in HBSS solution, indicating that the resistance of the system has increased after immersion in HBSS+. This could be due to the incorporation of sodium pyruvate and other components from HBSS+ into the system, which increases the bulk resistance and affects the electrical conductivity. In summary, based on the size of the Nyquist plot semicircle loops, sample A1 had the highest corrosion resistance, followed by B1. Samples A2, A3, B2 and B3 showed medium corrosion resistance, with corrosion resistance decreasing with increasing frequency for all samples in HBSS+ solution, while sample A1 showed the highest corrosion resistance while B1-B3 had the lowest based on the diameters of the distorted semicircular loops had corrosion

resistance. Heterogeneous corrosion reactions occur in all samples. The corrosion resistance decreases as the number of samples in the HBSS solution increases from A1 to B3. The rolling direction of the samples affects the EIS results because it affects the alloy's microstructure. The alloy microstructure can effect on the corrosion resistance. The samples that were rolled perpendicular to the RD (A1 and B1) have a different microstructure than the samples that were rolled parallel to the RD (A2 and B2), and the samples that were rolled at 45 degrees to the RD (A3 and B3). The different microstructures can result in different corrosion resistance properties, which can be observed in the EIS results.

Moreover, the orientation of the samples affected the impedance values. Samples A1 and B1, which were rolled perpendicular direction, had the highest impedance values, while samples A2 and B2, which were rolled parallel direction, had the lowest impedance values. Samples A3 and B3, which were rolled at 45° to the rolling direction, had intermediate impedance values.

Figure 4.21 b its Shows that the rolling direction of the samples affects the EIS results. Sample A1 and B1 were rolled perpendicular to the rolling direction, samples A2 and B2 were rolled parallel to the RD, and samples A3 and B3 were rolled at a 45° angle to the RD. The EIS results show that the samples rolled perpendicular to the RD have highest impedance, followed by the prepared alloys which rolled at a 45° angle to the RD, and then the samples rolled parallel to the RD. This suggests that an alloy's ability to withstand corrosion is influenced by the grain orientation within the sample. A further factor influencing the EIS results is the addition of Ca and Ce; samples containing these elements exhibit higher impedance values than samples without it.

The results of EIS show that the impedance of the samples rolled at 45° is generally higher than that of the samples rolled at 90°. This is particularly evident in the samples with added Ca and Ce (B1-B3), where the impedance of the samples rolled at 45° is consistently higher than that of the samples rolled at 90°. This suggests that orientation of the sample with respect to the rolling direction can have a significant effect on its electrochemical properties.

In both solutions, samples with Ca and Ce addition (B1-B3) showed higher impedance (Z') and lower negative impedance (-Z'') compared to those without addition (A1-A3), indicating improved corrosion resistance upon addition. The formation of a more compact and stable protective layer on the alloy's surface can be attributed to the presence of Ca and Ce elements. Within each set, the 45° rolled samples (A3, B3) exhibited the highest Z' and lowest -Z'', suggesting this orientation provided the best corrosion protection compared to 0° and 90°. This can be explained by the microstructural refinements and texture changes induced by 45° rolling, which enhanced the barrier properties and reduced the anodic dissolution of the alloy. Trends of Z' decreasing and -Z'' increasing over time were seen for all samples but were slower for B1-B3 and A3/B3 sets, demonstrating retardation of corrosion kinetics. This implies that the protective layers formed by Ca/Ce addition and 45° rolling were more durable and resistant to degradation than those formed by other conditions. The protective effects of Ca/Ce and 45° rolling were more significant at higher frequencies, implying their role in forming thicker and more uniform protective layers. The rolling direction and Ca/Ce addition had less of an impact on the impedance values at lower frequencies than did the solution resistance and charge transfer resistance. The combined effect of Ca/Ce and 45° rolling (B3) resulted in maximum improvement, indicating a synergistic influence on microstructure and corrosion inhibition. Regarding corrosion resistance and corrosion rate, the B3 sample was the best among all the samples with the highest Z' and the lowest Z'' in both solutions. It can be inferred that the ideal ratio of 45° rolling to Ca/Ce addition can improve the AZ31 magnesium alloy's corrosion resistance in physiological conditions.
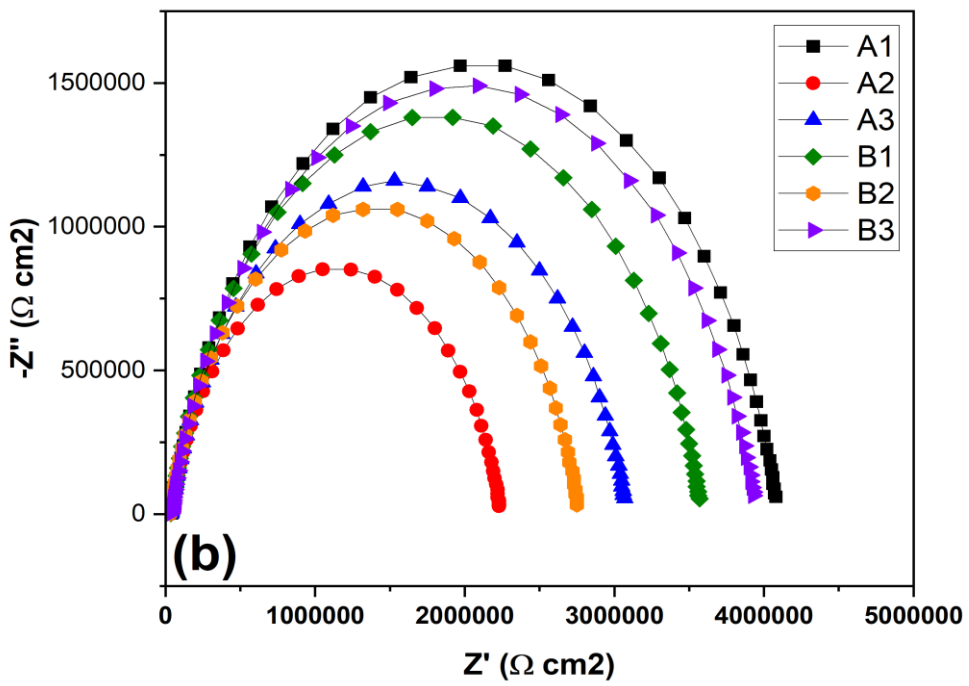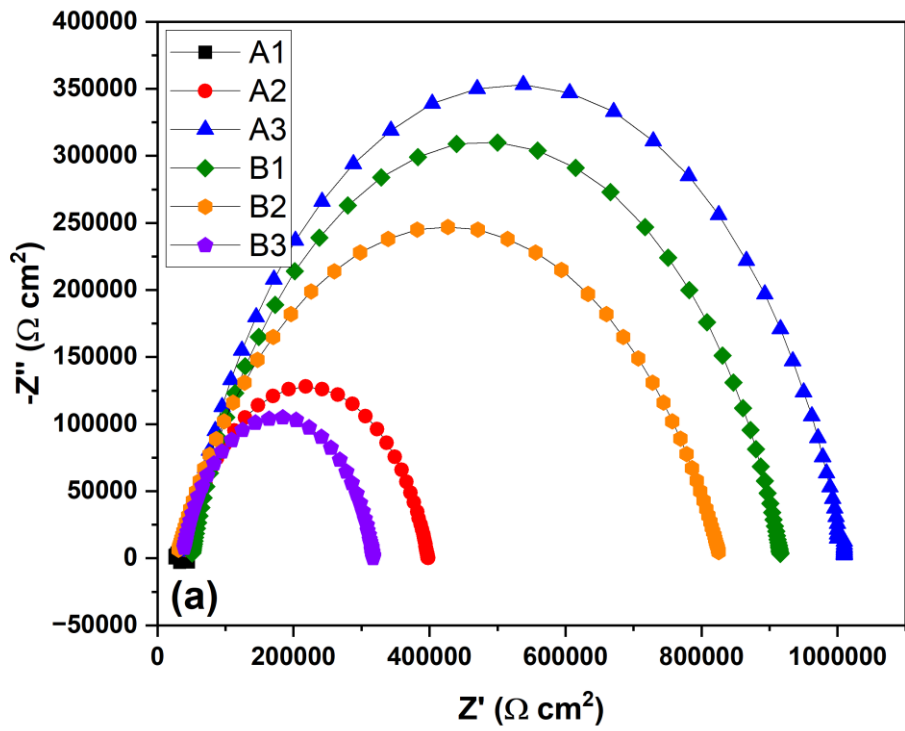
Figure 4.23. Nyquist curves of prepared alloys in a) white solution (HBSS$^+$) , and b) red solution (HBSS) **.**

PART 5

CONCLUSIONS

This study investigated the effects on the corrosion rate of AZ31 alloys of various Hank's solutions, Ca-Ce addition, and hot rolling in different directions. The potentiodynamic corrosion and immersion tests examined two different forms of corrosion. SEM and optical microstructure were used to examine the microstructure. The EDX apparatus was used to analyze the elements. The wet-wear test was conducted, and the following lists the outcomes of the tests and analyses that were done.

1. The XRD analysis revealed presence of α-Mg, β-Mg$_{17}$Al$_{12}$, Al$_{11}$Ce$_3$, and Al$_8$Mn$_5$ phases in the AZ31 Mg alloys, depending on the addition of Ce and Mn and their electronegativity difference with Mg.

2. The optical microstructure showed that the Ce and Ca refined grain size and weakened basal texture. The grain corners formed a ternary Mg-Zn-Ca phase after Ca addition. Ce and Ca may refine grain, strengthen second phase, and strengthen texture in AZ31 magnesium alloy. Hot-rolled sheets perpendicular to RD (90°) were more ductile and formable than 45° sheets.

3. The SEM analysis of the prepared samples in both white and red Hank's solutions revealed a high rate of pitting corrosion in samples A1 to A3, whereas the addition of Ca and Ce in samples B1 to B3 led to a noticeable decrease in the rate of corrosion.

4. The samples without and with addition of cerium and calcium in the red solution were more tendency to corrosion than the white solution.

5. Wear resistance, particularly evident in the 45° angle samples, with B3 exhibiting over double the wear resistance of A3; furthermore, the two-dimensional profiles illustrated narrower and shallower wear tracks for Ca- and Ce-added alloy, underscoring the effective reduction in wear through plastic deformation mitigation at the wear path edges.

6. The immersion corrosion test demonstrated that increased sandblasting intensity led to enhanced corrosion, attributed to heightened surface roughness; however, the addition of Ca and Ce notably improved the corrosion resistance of Mg-based grade AZ31 materials, as evidenced by lower weight loss in Ca-containing samples, the samples in the red solution were more tendency to corrosion than the white solution

7. The potentiodynamic polarization results revealed that the addition of Ca and Ce to AZ31 alloy generally improved its corrosion resistance in HBSS solution, evidenced by higher open circuit potential (Ecorr), lower corrosion current density (Icorr), and reduced cathodic and anodic Tafel slopes (Beta C and Beta A); however, in HBSS+ solution, the addition of Ca and Ce showed a potential negative impact on corrosion resistance, as indicated by slightly lower Ecorr, higher Icorr, increased cathodic Tafel slope (BetaC), and decreased anodic Tafel slope (BetaA), highlighting the complex and solution-dependent effects of alloy composition on the corrosion behavior of AZ31-Mg alloy.

8. The samples with the highest corrosion rate were those that were rolled crosswise to the rolling direction, while the samples with the lowest corrosion rate were rolled perpendicular direction.

9. Ca and Ce additions enhanced the AZ31 alloy's resistance to corrosion (samples B1−B3). The microstructure and orientation of the samples also had an impact on this resistance, as demonstrated by the EIS results with various impedance values.

REFERENCES

1. Zeng, R., Dietzel, W., Witte, F., Hort, N., & Blawert, C., "Progress and challenge for magnesium alloys as biomaterials", *Advanced Engineering Materials*,10(8): B3-B14 (2008).

2. Witte, F., Hort, N., Vogt, C., Cohen, S., Kainer, K. U., Willumeit, R., & Feyerabend, F. , "Degradable biomaterials based on magnesium corrosion", *Current opinion in solid state and materials science*,12(5-6): 63-72 (2008).

3. Cao, F., G.-L. Song, and A. Atrens, "Corrosion and passivation of magnesium alloys", *Corrosion Science*,111: 835-845 (2016).

4. Walsh, F.C., *RW Revie, Uhlig's Corrosion Handbook 2nd edition*. 2000, Springer.

5. Hamu, G.B., D. Eliezer, and L. Wagner, "The relation between severe plastic deformation microstructure and corrosion behavior of AZ31 magnesium alloy", *Journal of Alloys and Compounds*,468(1-2): 222-229 (2009).

6. Song, D., Ma, A., Jiang, J., Lin, P., Yang, D., & Fan, J. , "Corrosion behavior of equal-channel-angular-pressed pure magnesium in NaCl aqueous solution", *Corrosion Science*,52(2): 481-490 (2010).

7. AL-GBURI, A.S.N., *THE INVESTIGATION OF BIODEGRADABLE CORROSION PROPERTIES OF HOT ROLLED AT31 MG ALLOYS*. 2022.

8. Song, G.-L. and Z. Xu, "Crystal orientation and electrochemical corrosion of polycrystalline Mg", *Corrosion Science*,63: 100-112 (2012).

9. Liao, J., M. Hotta, and N. Yamamoto, "Corrosion behavior of fine-grained AZ31B magnesium alloy", *Corrosion Science*,61: 208-214 (2012).

10. Lu, Y., Deshmukh, S., Jones, I., & Chiu, Y. L., "Biodegradable magnesium alloys for orthopaedic applications: A review on corrosion, biocompatibility and surface modifications", *Materials Science and Engineering: C*,68: 948-963 (2016).

11. Ghoneim, A., A. Fekry, and M. Ameer, "Electrochemical behavior of magnesium alloys as biodegradable materials in Hank's solution", *Electrochimica acta*,55(20): 6028-6035 (2010).

12. Zhang, C., J. Lin, and H. Liu, "Magnesium-based biodegradable materials for biomedical applications", *MRS Advances*,3(40): 2359-2364 (2018).

13.   Wang, L., He, J., Yu, J., Arthanari, S., Lee, H., Zhang, H., Lu, L., Huang, G., Xing, B., Wang, H. and Shin, K.S., "Degradable Magnesium Corrosion Control for Implant Applications", *Materials*,15(18): 6197 (2022).

14.   Peng, H., Wang, W., Jiang, H., Zan, R., Sun, Y., Yu, S., Ni, J., Wang, W., Wang, T., Wang, J. and Zhang, X, "Effect of Galvanic Corrosion on the Degradability of Biomedical Magnesium", *Frontiers in Materials*,8: 767179 (2021).

15.   Tsao, L., "Stress-corrosion cracking susceptibility of AZ31 alloy after varied heat-treatment in 3.5 wt.% NaCl solution", *International journal of materials research*,101(9): 1166-1171 (2010).

16.   Wang, Z., Li, N., Li, R., Li, Y. and Ruan, L., "Biodegradable intestinal stents: a review", *Progress in Natural Science: Materials International*,24(5): 423-432 (2014).

17.   Chen, Y., Wang, Q., Peng, J., Zhai, C. and Ding, W., "Effects of extrusion ratio on the microstructure and mechanical properties of AZ31 Mg alloy", *Journal of Materials Processing Technology*,182(1-3): 281-285 (2007).

18.   Ishihara, S., Shibata, H., Komano, K., Goshima, T. and Nan, Z.Y., "Effect of extrusion ratio on fatigue properties of hot-extruded magnesium alloys", *Key engineering materials*,353: 291-294 (2007).

19.   Uematsu, Y., Tokaji, K., Kamakura, M., Uchida, K., Shibata, H. and Bekku, N, "Effect of extrusion conditions on grain refinement and fatigue behaviour in magnesium alloys", *Materials science and Engineering: A*,434(1-2): 131-140 (2006).

20.   Barnett, M., "Twinning and the ductility of magnesium alloys: Part I:"Tension" twins", *Materials science and Engineering: A*,464(1-2): 1-7 (2007).

21.   Liu, G., J. Zhou, and J. Duszczyk, "Prediction and verification of temperature evolution as a function of ram speed during the extrusion of AZ31 alloy into a rectangular section", *Journal of Materials Processing Technology*,186(1-3): 191-199 (2007).

22.   Humphreys, F.J. and M. Hatherly, *"Recrystallization and related annealing phenomena". Elsevier*(2012).

23.   de Almeida Pinto, R.A., "Electrochemical behaviour of magnesium alloys: study on the influence of rare earths as alloying elements", *Instituto Superior Técnico–Technical University of Lisbon*, (2008).

24.   Kramer, D.A., "Magnesium, its alloys and compounds", *US Geological Survey Open-File Report*,1: 341 (2001).

25. Mordike, B. and T. Ebert, "Magnesium: properties—applications—potential", *Materials science and Engineering: A*,302(1): 37-45 (2001).

26. Avedesian, M.M. and H. Baker, *"ASM specialty handbook: magnesium and magnesium alloys". ASM international Materials Park, OH*.274. (1999).

27. Wirth, C.J., Windhagen, H., Witte, F., Bach, F.W. and Kaese, V., *Medical implants, prostheses, prosthesis parts, medical instruments, devices and auxiliary contrivances made of a halogenide-modified magnesium substance*. 2005, Google Patents.

28. Prasad, S.S., Prasad, S.B., Verma, K., Mishra, R.K., Kumar, V. and Singh, S., "The role and significance of Magnesium in modern day research-A review", *Journal of Magnesium and Alloys*,10(1): 1-61 (2022).

29. Buldum, B.B., S. Aydın, and I. Ozkul, "Investigation of magnesium alloys machinability", *International Journal of Electronics Mechanical and Mechatronics Engineering*,2(3): 261-268 (2013).

30. Kainer, K.U., *"Magnesium alloys and technology". John Wiley & Sons*(2003).

31. Poinern, G.E.J., S. Brundavanam, and D. Fawcett, "Biomedical magnesium alloys: a review of material properties, surface modifications and potential as a biodegradable orthopaedic implant", *American Journal of Biomedical Engineering*,2(6): 218-240 (2012).

32. Russell, A. and W. Hugo, "7 antimicrobial activity and action of silver", *Progress in medicinal chemistry*,31: 351-370 (1994).

33. Wells, T.N., Scully, P., Paravicini, G., Proudfoot, A.E. and Payton, M.A., "Mechanism of irreversible inactivation of phosphomannose isomerases by silver ions and flamazine", *Biochemistry*,34(24): 7896-7903 (1995).

34. Thurman, R.B., C.P. Gerba, and G. Bitton, "The molecular mechanisms of copper and silver ion disinfection of bacteria and viruses", *Critical reviews in environmental science and technology*,18(4): 295-315 (1989).

35. Loukil, N., "Alloying elements of magnesium alloys: a literature review", *Magnesium alloys structure and properties*: 58-78 (2021).

36. Kannan, M.B., Dietzel, W., Blawert, C., Atrens, A. and Lyon, P.J.M.S., "Stress corrosion cracking of rare-earth containing magnesium alloys ZE41, QE22 and Elektron 21 (EV31A) compared with AZ80", *Materials science and Engineering: A*,480(1-2): 529-539 (2008).

37. Gu, X., Y. Zheng, Y. Cheng, S. Zhong, and T. Xi, "In vitro corrosion and biocompatibility of binary magnesium alloys", *Biomaterials*,30(4): 484-498 (2009).

38.   Gupta, M. and S.N.M. Ling, *"Magnesium, magnesium alloys, and magnesium composites". **John Wiley & Sons**(2011).

39.   Echeverry-Rendon, M., J.P. Allain, S.M. Robledo, F. Echeverria, and M.C. Harmsen, "Coatings for biodegradable magnesium-based supports for therapy of vascular disease: A general view"*, **Materials Science and Engineering: C**,102: 150-163 (2019).

40.   Luo, A., "Applications: aerospace, automotive and other structural applications of magnesium"*, **Fundamentals of magnesium alloy metallurgy**: 266-316 (2013).

41.   Li, L., M. Zhang, Y. Li, J. Zhao, L. Qin, and Y. Lai, "Corrosion and biocompatibility improvement of magnesium-based alloys as bone implant materials: a review"*, **Regenerative biomaterials**,4(2): 129-137 (2017).

42.   Radha, R. and D. Sreekanth, "Insight of magnesium alloys and composites for orthopedic implant applications–a review"*, **Journal of Magnesium and Alloys**,5(3): 286-312 (2017).

43.   Bamberger, M. and G. Dehm, "Trends in the development of new Mg alloys"*, **Annu. Rev. Mater. Res.**,38: 505-533 (2008).

44.   Elen, L., *AZ91 magnezyum alaşımına farklı oranlarda Bi ve Sb ilavesi ile katılaşma hızının mikroyapı ve mekanik özelliklere etkisi*. 2012, Fen Bilimleri Enstitüsü.

45.   Blawert, C., D. Fechner, D. Höche, V. Heitmann, W. Dietzel, K. Kainer, P. Živanović, C. Scharf, A. Ditze, and J. Gröbner, "Magnesium secondary alloys: Alloy design for magnesium alloys with improved tolerance limits against impurities"*, **Corrosion Science**,52(7): 2452-2468 (2010).

46.   Okamoto, H., "Supplemental Literature Review of Binary Phase Diagrams: Al-Mg, Bi-Sr, Ce-Cu, Co-Nd, Cu-Nd, Dy-Pb, Fe-Nb, Nd-Pb, Pb-Pr, Pb-Tb, Pd-Sb, and Si-W"*, **Journal of Phase Equilibria and Diffusion**,36: 183-195 (2015).

47.   Friedrich, H.E. and B.L. Mordike, *"Magnesium technology". **Springer**.212. (2006).

48.   Kim, B.H., S.W. Lee, Y.H. Park, and I.M. Park, "The microstructure, tensile properties, and creep behavior of AZ91, AS52 and TAS652 alloy"*, **Journal of Alloys and Compounds**,493(1-2): 502-506 (2010).

49.   Kim, Y.M., S.S. Park, S.K. Park, H.T. Son, and J.S. Lee. *"Hot-Extruded Microstructure and Mechanical Properties of Mg-Al-Sn Alloys"*. in **Defect and Diffusion Forum**. Trans Tech Publ (2010).

50.   Dev, A., N. Naskar, N. Kumar, A. Jena, and M. Paliwal, "A systematic investigation of secondary phase dissolution in Mg–Sn alloys", *Journal of Magnesium and Alloys*,7(4): 725-737 (2019).

51.   Wang, J., Z. Bao, C. Wu, S. Zhang, N. Wang, Q. Wang, and Z. Yi, "Progress in partially degradable titanium-magnesium composites used as biomedical implants", *Frontiers in Bioengineering and Biotechnology*,10: 996195 (2022).

52.   Lynch, R., "Zinc: alloying, thermomechanical processing, properties, and applications", *Encyclopedia of Materials: Science and Technology*: 9869-9883 (2001).

53.   Rollez, D., A. Pola, and F. Prenger, "Zinc alloy family for foundry purposes", *WORLD OF METALLURGY, ERZMETALL*,68(6): 354-358 (2015).

54.   Mezbahul-Islam, M., A. Mostafa, and M. Medraj, "Essential magnesium alloys binary phase diagrams and their thermochemical data", *Journal of Materials*,2014 (2014).

55.   Baker, H., "Alloy phase diagrams", *ASM handbook*,3: 2-80 (1992).

56.   Dan'Kov, S.Y., A. Tishin, V. Pecharsky, and K. Gschneidner, "Magnetic phase transitions and the magnetothermal properties of gadolinium", *Physical Review B*,57(6): 3478 (1998).

57.   Blawert, C., N. Hort, and K. Kainer, "Automotive applications of magnesium and its alloys", *Trans. Indian Inst. Met*,57(4): 397-408 (2004).

58.   Tekumalla, S., S. Seetharaman, A. Almajid, and M. Gupta, "Mechanical properties of magnesium-rare earth alloy systems: A review", *Metals*,5(1): 1-39 (2014).

59.   Hort, N., Y.-d. Huang, D. Fechner, M. Störmer, C. Blawert, F. Witte, C. Vogt, H. Drücker, R. Willumeit, and K. Kainer, "Magnesium alloys as implant materials–Principles of property design for Mg–RE alloys", *Acta Biomaterialia*,6(5): 1714-1725 (2010).

60.   Wang, B., C.-y. Chen, J.-q. Li, L.-z. Wang, Y.-p. Lan, and S.-y. Wang, "Production of Fe–Ti alloys from mixed slag containing titanium and Fe2O3 via direct electrochemical reduction in molten calcium chloride", *Metals*,10(12): 1611 (2020).

61.   Ramakrishnegowda, N., *Development of Layered Mg-Ti Composites for Biomedical Applications*. 2016, Christian-Albrechts-Universität zu Kiel.

62.   Yang, H., B. Jia, Z. Zhang, X. Qu, G. Li, W. Lin, D. Zhu, K. Dai, and Y. Zheng, "Alloying design of biodegradable zinc as promising bone implants for load-bearing applications", *Nature communications*,11(1): 401 (2020).

63. Gusieva, K., C. Davies, J. Scully, and N. Birbilis, "Corrosion of magnesium alloys: the role of alloying", *International materials reviews*, 60(3): 169-194 (2015).

64. Kirkland, N.T., M.P. Staiger, D. Nisbet, C.H. Davies, and N. Birbilis, "Performance-driven design of Biocompatible Mg alloys", *Jom*, 63: 28-34 (2011).

65. Yim, C., B. You, R. Jang, and S. Lim, "Effects of melt temperature and mold preheating temperature on the fluidity of Ca containing AZ31 alloys", *Journal of Materials Science*, 41: 2347-2350 (2006).

66. Wang, Y., M. Xia, Z. Fan, X. Zhou, and G. Thompson, "The effect of Al8Mn5 intermetallic particles on grain size of as-cast Mg–Al–Zn AZ91D alloy", *Intermetallics*, 18(8): 1683-1689 (2010).

67. Suzuki, A., N. Saddock, L. Riester, E. Lara-Curzio, J. Jones, and T. Pollock, "Effect of Sr additions on the microstructure and strength of a Mg-Al-Ca ternary alloy", *Metallurgical and Materials Transactions A*, 38: 420-427 (2007).

68. Zhang, J., Z. Guo, F. Pan, Z. Li, and X. Luo, "Effect of composition on the microstructure and mechanical properties of Mg–Zn–Al alloys", *Materials science and Engineering: A*, 456(1-2): 43-51 (2007).

69. Zhang, Z., *Development of Magnesium-Based Allovs for Elevated Temperature Applications*. 2000, Univ. Laval, Québec: Canada.

70. Roberge, P.R., *"Handbook of corrosion engineering"*. *McGraw-Hill Education*(2019).

71. Schwam, D., J.F. Wallace, Y. Zhu, S. Viswanathan, and S. Iskander, *Enhancements in magnesium die casting impact properties*. 2000, Case Western Reserve University (US).

72. Das, S. and L. Davis, "High performance aerospace alloys via rapid solidification processing", *Materials science and engineering*, 98: 1-12 (1988).

73. Peron, M., F. Berto, and J. Torgersen, *"Magnesium and Its Alloys as Implant Materials: Corrosion, Mechanical and Biological Performances"*. *CRC Press*(2020).

74. Gong, H., A. Kontsos, Y. Kim, P.I. Lelkes, Q. Zhang, D. Yao, K. Hazeli, and J.G. Zhou. *"Micro characterization of Mg and Mg alloy for biodegradable orthopedic implants application"*. in *International Manufacturing Science and Engineering Conference*. American Society of Mechanical Engineers (2012).

75. Putra, A.G., A. Manaf, and A. Anawati. *"Enhancing the Hardness of Mg-9Al-1Zn Cast Alloy by Solution Treatment"*. in *IOP Conference Series: Materials Science and Engineering*. IOP Publishing (2019).

76.   Xin, Y., C. Liu, X. Zhang, G. Tang, X. Tian, and P.K. Chu, "Corrosion behavior of biomedical AZ91 magnesium alloy in simulated body fluids", *Journal of materials research*,22(7): 2004-2011 (2007).

77.   Kokubo, T. and H. Takadama, "How useful is SBF in predicting in vivo bone bioactivity?", *Biomaterials*,27(15): 2907-2915 (2006).

78.   Gu, X.-N. and Y.-F. Zheng, "A review on magnesium alloys as biodegradable materials", *Frontiers of Materials Science in China*,4: 111-115 (2010).

79.   Xin, Y., K. Huo, H. Tao, G. Tang, and P.K. Chu, "Influence of aggressive ions on the degradation behavior of biomedical magnesium alloy in physiological environment", *Acta Biomaterialia*,4(6) (2008).

80.   Lai, H., J. Li, J. Li, Y. Zhang, and Y. Xu, "Effects of Sr on the microstructure, mechanical properties and corrosion behavior of Mg-2Zn-x Sr alloys", *Journal of Materials Science: Materials in Medicine*,29: 1-14 (2018).

81.   Wan, P., X. Lin, L. Tan, L. Li, W. Li, and K. Yang, "Influence of albumin and inorganic ions on electrochemical corrosion behavior of plasma electrolytic oxidation coated magnesium for surgical implants", *Applied surface science*,282: 186-194 (2013).

82.   Yamamoto, A. and S. Hiromoto, "Effect of inorganic salts, amino acids and proteins on the degradation of pure magnesium in vitro", *Materials Science and Engineering: C*,29(5): 1559-1568 (2009).

83.   Roos- Jansåker, A.M., S. Renvert, and J. Egelberg, "Treatment of peri-implant infections: a literature review", *Journal of clinical periodontology*,30(6): 467-485 (2003).

84.   Nociti Jr, F.H., M.Â.N. Machado, C.M. Stefani, E.A. Sallum, and A.W. Sallum, "Absorbable versus nonabsorbable membranes and bone grafts in the treatment of ligature- induced peri- implantitis defects in dogs: Part I. A clinical investigation", *Clinical Oral Implants Research*,12(2): 115-120 (2001).

85.   Wetzel, A.C., J. Vlassis, R.G. Caffesse, C.H. Hämmerle, and N.P. Lang, "Attempts to obtain re- osseointegration following experimental peri- implantitis in dogs", *Clinical Oral Implants Research*,10(2): 111-119 (1999).

86.   Tie, D., *Antibacterial Mg-Ag Biodegradable Alloys*. 2013, Technische Universität Hamburg.

87.   Han, P., M. Tan, S. Zhang, W. Ji, J. Li, X. Zhang, C. Zhao, Y. Zheng, and Y. Chai, "Shape and site dependent in vivo degradation of Mg-Zn pins in rabbit femoral condyle", *International journal of molecular sciences*,15(2): 2959-2970 (2014).

88.   Windhagen, H., K. Radtke, A. Weizbauer, J. Diekmann, Y. Noll, U. Kreimeyer, R. Schavan, C. Stukenborg-Colsman, and H. Waizy, "Biodegradable magnesium-based screw clinically equivalent to titanium screw in hallux valgus surgery: short term results of the first prospective, randomized, controlled clinical pilot study", *Biomedical engineering online*,12: 1-10 (2013).

89.   Zhao, D., S. Huang, F. Lu, B. Wang, L. Yang, L. Qin, K. Yang, Y. Li, W. Li, and W. Wang, "Vascularized bone grafting fixed by biodegradable magnesium screw for treating osteonecrosis of the femoral head", *Biomaterials*,81: 84-92 (2016).

90.   CFDA. *Announcement of the Review Results of Special Approval Applications for Innovative Medical Devices*. 2021 [cited 2023; Available from: https://www.cmde.org.cn/CL0004/3139.html.

91.   Revie, R.W., *"Uhlig's corrosion handbook"*. *John Wiley & Sons*.51. (2011).

92.   Yun, Y., Z. Dong, N. Lee, Y. Liu, D. Xue, X. Guo, J. Kuhlmann, A. Doepke, H.B. Halsall, and W. Heineman, "Revolutionizing biodegradable metals", *Materials Today*,12(10): 22-32 (2009).

93.   Thornburg, D. and H. Piehler, "An analysis of constrained deformation by slip and twinning in hexagonal close packed metals and alloys", *Metallurgical Transactions A*,6: 1511-1523 (1975).

94.   Wiersma, B., *A Structural Integrity Assessment of the Tank farm Waste Transfer System*. 2006.

95.   Makar, G. and J. Kruger, "Corrosion of magnesium", *International materials reviews*,38(3): 138-153 (1993).

96.   Valente, T., "Grain boundary effects on the behavior of WE43 magnesium castings in simulated marine environment", *Journal of materials science letters*,20(1): 67-69 (2001).

97.   Rongchang, Z., H. Enhou, and K. Wei, "Corrosion of artificial aged magnesium alloy AZ80 in 3.5 wt pct NaCl solutions", *Journal of Materials Sciences and Technology*,23(03): 353 (2007).

98.   Potzies, C. and K.U. Kainer, "Fatigue of magnesium alloys", *Advanced Engineering Materials*,6(5): 281-289 (2004).

99.   Stephens, R., C. Schrader, and K. Lease, "Corrosion fatigue of AZ91E-T6 cast magnesium alloy in a 3.5 percent NaCl aqueous environment", (1995).

100.   Yue, T.M., H. Ha, and N. Musson, "Grain size effects on the mechanical properties of some squeeze cast light alloys", *Journal of Materials Science*,30: 2277-2283 (1995).

101. Eliezer, A., J. Haddad, Y. Unigovski, and E. Gutman, "Static and dynamic corrosion fatigue of Mg alloys used in automotive industry", *Materials and manufacturing processes*,20(1): 75-88 (2005).

102. Rodrigues, P.S., I.R. Zenóbio, T.I. da Silva, C.Q. Fernandes, T.G. de Sousa, J.A. de Castro, G.S. da Fonseca, J.A. Huguenin, and E.A. Ferreira, "Effect of Aging on Corrosion Resistance of AZ31 Magnesium Alloy", *Journal of Materials Engineering and Performance*: 1-13 (2023).

103. Op't Hoog, C., N. Birbilis, and Y. Estrin, "Corrosion of pure Mg as a function of grain size and processing route", *Advanced Engineering Materials*,10(6): 579-582 (2008).

104. Liu, M., D. Qiu, M.-C. Zhao, G. Song, and A. Atrens, "The effect of crystallographic orientation on the active corrosion of pure magnesium", *Scripta materialia*,58(5): 421-424 (2008).

105. Song, G.-L., R. Mishra, and Z. Xu, "Crystallographic orientation and electrochemical activity of AZ31 Mg alloy", *Electrochemistry Communications*,12(8): 1009-1012 (2010).

106. Klarner, A.D., *"Development of Mg-Al-Sn and Mg-Al-Sn-Si Alloys and Optimization of Super Vacuum Die Casting Process for Lightweight Applications"*. *The Ohio State University*(2018).

107. Mokhtarishirazabad, M., M. Azadi, G.H. Farrahi, G. Winter, and W. Eichlseder, "Improvement of high temperature fatigue lifetime in AZ91 magnesium alloy by heat treatment", *Materials science and Engineering: A*,588: 357-365 (2013).

108. Vespa, G., L. Mackenzie, R. Verma, F. Zarandi, E. Essadiqi, and S. Yue, "The influence of the as-hot rolled microstructure on the elevated temperature mechanical properties of magnesium AZ31 sheet", *Materials science and Engineering: A*,487(1-2): 243-250 (2008).

109. Han, T., G. Huang, Q. Deng, G. Wang, B. Jiang, A. Tang, Y. Zhu, and F. Pan, "Grain refining and mechanical properties of AZ31 alloy processed by accumulated extrusion bonding", *Journal of Alloys and Compounds*,745: 599-608 (2018).

110. Dalland, O. and E. Nes, "Origin of cube texture during hot rolling of commercial Al・Mn・Mg alloys", *Acta Materialia*,44(4): 1389-1411 (1996).

111. Wasiur-Rahman, S. and M. Medraj, "Critical assessment and thermodynamic modeling of the binary Mg–Zn, Ca–Zn and ternary Mg–Ca–Zn systems", *Intermetallics*,17(10): 847-864 (2009).

112. Bahrami, A., M. Kiani Khouzani, S.A. Mokhtari, S. Zareh, and M. Yazdan Mehr, "Root cause analysis of surface cracks in heavy steel plates during the hot rolling process", *Metals*,9(7): 801 (2019).

113. Guo, F., D. Zhang, X. Yang, L. Jiang, S. Chai, and F. Pan, "Effect of rolling speed on microstructure and mechanical properties of AZ31 Mg alloys rolled with a wide thickness reduction range", *Materials science and Engineering: A*,619: 66-72 (2014).

114. Shang, L., "Effect of microalloying on microstructure and hot working behavior for AZ31 based magnesium alloy", (2008).

115. Ding, Y., Q. Le, Z. Zhang, and J. Cui, "Effect of rolling speed on microstructure and mechanical properties of as-cast AZ31B alloy under different reduction schedules", *Journal of Materials Processing Technology*,233: 161-173 (2016).

116. Mallick, P.K., *"Materials, design and manufacturing for lightweight vehicles"*. *Woodhead publishing*(2020).

117. Kara, I.H. and H. Demirtas, "The effect of hot rolling process on macro-texture and high-temperature mechanical properties of AZ31B alloy modified by Ca and Ce", *Proceedings of the Institution of Mechanical Engineers, Part E: Journal of Process Mechanical Engineering*,237(4): 1566-1573 (2023).

118. Chen, H., J. Tang, W. Gong, Y. Gao, F. Tian, and L. Chen, "Effects of annealing treatment on the microstructure and corrosion behavior of hot rolled AZ31 Mg alloy", *Journal of Materials Research and Technology*,15: 4800-4812 (2021).

119. Tkacz, J., K. Slouková, J. Minda, J. Drábiková, S. Fintová, P. Doležal, and J. Wasserbauer, "Influence of the composition of the Hank's balanced salt solution on the corrosion behavior of AZ31 and AZ61 magnesium alloys", *Metals*,7(11): 465 (2017).

120. Jawad, S.M., *Effect of Cr and Cr Additives On Corrosion and Dry Sliding Wear of NiTi Shape Memory Alloy*. 2015, M. Sc. thesis Department of Metallurgical Engineering, University of Babylon.

121. Şimşek, I. and D. Özyürek, "Investigation of Wear and Corrosion Behaviors of Ti15Mo Alloy Produced by Mechanical Alloying Method in SBF Environment", *Powder Metallurgy and Metal Ceramics*,58: 446-454 (2019).

122. Wang, T., T. Zhu, J. Sun, R. Wu, and M. Zhang, "Influence of rolling directions on microstructure, mechanical properties and anisotropy of Mg-5Li-1Al-0.5 Y alloy", *Journal of Magnesium and Alloys*,3(4): 345-351 (2015).

123. Chaudry, U., Y. Kim, and K. Hamad, "Effect of Ca addition on the room-temperature formability of AZ31 magnesium alloy", *Materials Letters*,238: 305-308 (2019).

124. Song, L., Y. Lu, Y. Zhang, X. Li, M. Cong, and W. Xu, "The effect of Ca addition on microstructure and mechanical properties of extruded AZ31 alloys", *Vacuum*,168: 108822 (2019).

125. Masoudpanah, S. and R. Mahmudi, "Effects of rare-earth elements and Ca additions on the microstructure and mechanical properties of AZ31 magnesium alloy processed by ECAP", *Materials science and Engineering: A*,526(1-2): 22-30 (2009).

126. AKBAŞ, A. and M. ZEREN, "Investigation of the effect of various Ca content on microstructure and mechanical properties of as-cast ZK60 Magnesium alloys", *Politeknik Dergisi*: 1-1 (2023).

127. Li, Q., W. Xiong, M. Yu, J. Li, L. Liu, G. Zhu, L. Wang, J. Wang, S. Yu, and E. Liu, "Effect of Ce content on performance of AZ31 magnesium alloy anode in air battery", *Journal of Alloys and Compounds*,891: 161914 (2022).

128. Kim, K.H., N.D. Nam, J.G. Kim, K.S. Shin, and H.C. Jung, "Effect of calcium addition on the corrosion behavior of Mg–5Al alloy", *Intermetallics*,19(12): 1831-1838 (2011).

129. Chaudry, U.M., A. Farooq, K. bin Tayyab, A. Malik, M. Kamran, J.-G. Kim, C. Li, K. Hamad, and T.-S. Jun, "Corrosion behavior of AZ31 magnesium alloy with calcium addition", *Corrosion Science*,199: 110205 (2022).

130. Nam, N., J. Kim, K. Shin, and H. Jung, "The effect of rare earth additions on the electrochemical properties of Mg–5Al-based alloys", *Scripta materialia*,63(6): 625-628 (2010).

131. Hanna, A., A. Dakhouche, K. Tirsatine, A. Sari, Y. Khereddine, D. Bradai, and H. Azzeddine, "Effect of hot rolling on the corrosion behavior of AZ31 magnesium alloy", *Metallurgical Research & Technology*,116(1): 109 (2019).

132. Ren, Y., J. Huang, K. Yang, B. Zhang, Z. Yao, and H. Wang, "Study of bio-corrosion of pure magnesium", *Jinshu Xuebao*,41(11): 1228-1232 (2005).

133. Gu, X.-N., S.-S. Li, X.-M. Li, and Y.-B. Fan, "Magnesium based degradable biomaterials: A review", *Frontiers of Materials Science*,8: 200-218 (2014).

134. Zhu, Y., G. Wu, Y.-H. Zhang, and Q. Zhao, "Growth and characterization of Mg (OH) 2 film on magnesium alloy AZ31", *Applied surface science*,257(14): 6129-6137 (2011).

135. Song, Y., D. Shan, R. Chen, F. Zhang, and E.-H. Han, "Biodegradable behaviors of AZ31 magnesium alloy in simulated body fluid", *Materials Science and Engineering: C*,29(3): 1039-1045 (2009).

136. McNaught, A.D. and A. Wilkinson, *"Compendium of chemical terminology". Blackwell Science Oxford*.1669. (1997).

137. Li, H., D. Liu, Y. Zhao, F. Jin, and M. Chen, "The influence of Zn content on the corrosion and wear performance of Mg-Zn-Ca alloy in simulated body fluid", *Journal of Materials Engineering and Performance*,25: 3890-3895 (2016).

138. Liu, D.-B., B. Wu, X. Wang, and M.-F. Chen, "Corrosion and wear behavior of an Mg–2Zn–0.2 Mn alloy in simulated body fluid", *Rare Metals*,34: 553-559 (2015).

139. Yang, J., J. Peng, E.A. Nyberg, and F.-s. Pan, "Effect of Ca addition on the corrosion behavior of Mg–Al–Mn alloy", *Applied surface science*,369: 92-100 (2016).

140. Wang, L., B.-P. Zhang, and T. Shinohara, "Corrosion behavior of AZ91 magnesium alloy in dilute NaCl solutions", *Materials & Design*,31(2): 857-863 (2010).

141. Liu, J., E.H. Han, Y. Song, and D. Shan, "Effect of twins on the corrosion behavior of Mg–5Y–7Gd–1Nd–0.5 Zr Mg alloy", *Journal of Alloys and Compounds*,757: 356-363 (2018).

142. Feliu Jr, S., "Electrochemical impedance spectroscopy for the measurement of the corrosion rate of magnesium alloys: Brief review and challenges", *Metals*,10(6): 775 (2020).

143. Tkacz, J., K. Slouková, J. Minda, J. Drábiková, S. Fintová, P. Doležal, and J. Wasserbauer, "Corrosion behavior of wrought magnesium alloys AZ31 and AZ61 in Hank's solution", *KOM–Corrosion and Material Protection Journal*,60(4): 101-106 (2016).

144. Esmaily, M., J. Svensson, S. Fajardo, N. Birbilis, G. Frankel, S. Virtanen, R. Arrabal, S. Thomas, and L. Johansson, "Fundamentals and advances in magnesium alloy corrosion", *Progress in materials science*,89: 92-193 (2017).

145. Zhou, M., L. Yan, H. Ling, Y. Diao, X. Pang, Y. Wang, and K. Gao, "Design and fabrication of enhanced corrosion resistance Zn-Al layered double hydroxides films based anion-exchange mechanism on magnesium alloys", *Applied surface science*,404: 246-253 (2017).

146. Huang, Z., J. Zhou, G. Yang, H. Lai, and C. Qi, "Effect of cross rolling on the corrosion resistance of AZ31 magnesium alloy", *Revista de Chimie*,71(8): 176-182 (2020).

147. Khan, A.S., A. Pandey, T. Gnäupel-Herold, and R.K. Mishra, "Mechanical response and texture evolution of AZ31 alloy at large strains for different strain rates and temperatures", *International Journal of Plasticity*,27(5): 688-706 (2011).

RESUME

Ali Abdulhaleem Raoof AL SHAIBANI is a material engineer who graduated from the Metallurgy Engineering Engineering, University of Technology - Iraq. He received his Bachelor's degree in 2007-2008. He is currently studying for his Master's degree at Karabük University in the field of Materials Engineering.